

Fall 2014

Modeling of High Pressure Radial Piston Pumps

Pulkit Agarwal
Purdue University

Follow this and additional works at: https://docs.lib.purdue.edu/open_access_theses



Part of the [Mechanical Engineering Commons](#)

Recommended Citation

Agarwal, Pulkit, "Modeling of High Pressure Radial Piston Pumps" (2014). *Open Access Theses*. 297.
https://docs.lib.purdue.edu/open_access_theses/297

This document has been made available through Purdue e-Pubs, a service of the Purdue University Libraries. Please contact epubs@purdue.edu for additional information.

PURDUE UNIVERSITY
GRADUATE SCHOOL
Thesis/Dissertation Acceptance

This is to certify that the thesis/dissertation prepared

By Pulkit Agarwal

Entitled
Modeling of High Pressure Radial Piston Pumps

For the degree of Master of Science in Mechanical Engineering

Is approved by the final examining committee:

Andrea Vacca

Monika Ivantysynova

John Lumkes

To the best of my knowledge and as understood by the student in the Thesis/Dissertation Agreement, Publication Delay, and Certification/Disclaimer (Graduate School Form 32), this thesis/dissertation adheres to the provisions of Purdue University's "Policy on Integrity in Research" and the use of copyrighted material.

Andrea Vacca

Approved by Major Professor(s): _____

Approved by: Ganesh Subbrayan

12/08/2014

Head of the Department Graduate Program

Date

MODELING OF HIGH PRESSURE RADIAL PISTON PUMPS

A Thesis

Submitted to the Faculty

of

Purdue University

by

Pulkit Agarwal

In Partial Fulfillment of the

Requirements for the Degree

of

Master of Science in Mechanical Engineering

December 2014

Purdue University

West Lafayette, Indiana

To my parents, sister and my cute little niece Anvi

ACKNOWLEDGEMENTS

I would like to extend my heartfelt gratitude to Prof. Andrea Vacca for giving me this exciting opportunity to perform research on fluid power components. This work would not have been possible without the valuable support and guidance provided by him through these years. I would also like to thank Prof. Monika Ivantysynova for being a part of my graduate committee and for her insightful comments and suggestions throughout my research. Also, I am sincerely indebted to Kelong for all the assistance provided during his stay as a visiting researcher at Maha.

Thanks are due to all my labmates especially Divya, Ram, Sid, Matteo, Tim, Gabriele, Guido, Addison, Meike, Mrudula for making my stay at Maha a truly enjoyable and memorable experience. My acknowledgement for the lab would not be complete without thanking Susan, Connie and Antony for their help in making all our lives in graduate school so much easier and their enthusiasm in spreading the cheer in the lab.

I would like to thank my family members who have shown constant faith in me and have always been there for my support.

TABLE OF CONTENTS

	Page
LIST OF TABLES	vii
LIST OF FIGURES	viii
NOMENCLATURE	xv
ABSTRACT	xxi
CHAPTER 1. INTRODUCTION	1
1.1 Introduction to Radial Piston Machines	1
1.1.1 The Reference Pump Design	2
1.2 Research Objectives	4
1.3 Literature Overview	6
1.3.1 Modeling of Radial Piston Machines	6
1.3.2 Lumped Parameter Modeling of Positive Displacement Machines	7
1.3.3 Lubricating Gap Model for Positive Displacement Machines	7
1.3.4 Friction Modeling in Line EHL	8
CHAPTER 2. STRUCTURE OF THE SIMULATION MODEL	9
2.1 Geometric Model	10
CHAPTER 3. GLOBAL FLUID DYNAMIC MODEL	13
3.1 Lumped Parameter Approach	13
3.2 Solution Process	18
3.3 Results	19
3.4 Generic Hydraulic System	23
3.4.1 Description	24
3.4.2 Results	26
CHAPTER 4. PISTON-CYLINDER INTERFACE	30

	Page
4.1 Fluid Solver	31
4.1.1 Fluid Film Geometry	32
4.1.2 Mesh Setup & Boundary Conditions	34
4.1.3 Solution Process	35
4.1.4 Evaluation of Performance Parameters	38
4.1.4.1 Leakage flow	38
4.1.4.2 Power losses due to viscous friction	38
4.2 Solid Deformation Solver	39
4.2.1 Influence Method for Evaluating Material Deformation	40
4.2.2 Ideal Support Constraint	41
4.3 Dynamic Linking of Fluid & Solid Meshes	43
4.4 Force Analysis of Piston	44
4.5 FSI Solution Algorithm	49
4.6 Results	50
4.6.1 Result Comparison between FSI and Rigid Body Model	53
4.6.2 Evaluation of Performance Parameters using the FSI Model	59
4.6.3 Effect of Changing Clearance on Simulation Results	62
CHAPTER 5. CAM-PISTON INTERFACE	67
5.1 EHL Model	69
5.1.1 Governing Equations	70
5.1.2 Discretization of Lubricating Domain	73
5.1.3 Incorporating Non-Newtonian Fluid Behavior	74
5.1.4 Solution Algorithm	78
5.1.5 Prediction of Traction/friction Forces in EHL Contact	81
5.1.6 Potentials of the EHL Model	81
5.2 Application of EHL Model to Reference Pump Geometry	85
5.2.1 Cam-piston Interface with Direct Cam-piston Contact	86
5.2.2 Cam-piston Interface with Rolling Element Bearing and Outer Race	89
5.3 Results from the Fully Coupled Pump Model	94

	Page
5.3.1 Results for Direct Cam-piston Contact.....	94
5.3.2 Results for Rolling Element Bearing type Interface.....	96
5.3.3 Result Comparison for Different Cam-piston Configurations.....	98
5.3.4 Design Directions for Reference Pump using the Developed EHL Model .	101
CHAPTER 6. CONCLUSION & FUTURE WORK.....	104
LIST OF REFERENCES	107
APPENDICES	
Appendix A. Derivation of the Pressure Buildup Equation.....	114
Appendix B. Derivation of the Reynolds Equation.....	116

LIST OF TABLES

Table	Page
Table 1: Operating conditions used for generating results from global fluid dynamic model.....	20
Table 2: Nomenclature for forces as shown in Figure 37.....	44
Table 3: Details of the reference pump, working fluid and solid component parameters used in simulations.....	52
Table 4: Velocity distributions in different lubricating conditions.....	76
Table 5: Non-Newtonian formulation of Reynolds equation.	77
Table 6: Output parameters for the operating condition shown in Figure 74.	94

LIST OF FIGURES

Figure	Page
Figure 1: Common designs of radial piston pumps	1
Figure 2: Top view of radial piston pump block.....	2
Figure 3: Inside view of pump housing	3
Figure 4: Detailed view of a displacement chamber.....	4
Figure 5: Schematic of the multi-domain simulation tool for modeling radial piston machines	9
Figure 6: Illustration of geometrical parameters to determine piston position (x_p) as a function of cam rotation (θ_p).	11
Figure 7: Instantaneous piston displacements in 1 cycle of shaft revolution	12
Figure 8: Piston velocity at varying shaft angles for complete pump cycle. <i>Shaft speed=1200 rpm</i>	12
Figure 9: Piston-cylinder gap length vs shaft angle for complete pump cycle. <i>Shaft speed=1200 rpm</i>	12
Figure 10: Schematic of the lumped parameter model for the reference pump design	14
Figure 11: The displacement chamber control volume.....	15
Figure 12: Geometrical parameters and force analysis of a ball check valve with conical seat.....	16
Figure 13: HP channel control volume	17
Figure 14: Flow connections through a single displacement chamber	18
Figure 15: AMESim implementation of the complete hydraulic system	19
Figure 16: Pressure (A) and flow rate (B) at pump outlet as a function of shaft angle. Operating condition: 1	20

Figure	Page
Figure 17: Pressure (A) and flow rate (B) at pump outlet as a function of shaft angle. Operating condition: 2	20
Figure 18: Pressure (A) and flow rate (B) at pump outlet as a function of shaft angle. Operating condition: 3	21
Figure 19: Pressure (A) and flow rate (B) at pump outlet as a function of shaft angle. Operating condition: 4	21
Figure 20: Flow rate comparison of four displacement chambers in 1 cycle of shaft rotation.....	22
Figure 21: Instantaneous pressures in displacement chamber (A) and flow rate through check valves (B) at operating condition 1. <i>Valve timings: (1) Inlet valve opens, (2) inlet valve closes, (3) Outlet valve opens, (4) Outlet valve closes</i>	22
Figure 22: ISO schematic of the complete hydraulic system for operating high pressure hydraulic tools.	24
Figure 23: Structural details of the spool block.....	26
Figure 24: Flow rate at system outlet vs pressure at system outlet.....	27
Figure 25: Experimental setup for pressure measurements in LP flow control system parts.....	28
Figure 26: Validation of pressure generation between the HP and LP pump.....	28
Figure 27: Lubricating gaps in a rotating cam type radial piston pump	30
Figure 28: Magnified view of the piston-cylinder lubricating gap showing leakage flow	32
Figure 29: (A) Evaluation of film thickness in the lubricating gap domain. (B) Fluid film in unwrapped configuration	33
Figure 30: Computational grid for fluid domain with boundary conditions.....	35
Figure 31: (A) Terms in Equation (4.2) : top surface (h_t); bottom surface (h_b); fixed cylinder (V_t); piston velocity (V_b). (B) Reference plane and sign convention.....	36

Figure	Page
Figure 32: Solid mesh for piston and cylinder geometries	40
Figure 33: Deformation fields in cylinder (A) and piston (B) on application on reference pressure on a single cell. Ideal support constraint used for both geometries.....	41
Figure 34: Ideal support constraint for piston & cylinder geometries	42
Figure 35: Dynamic link between fluid & solid mesh. Fluid mesh elements are shown in blue while red lines represent solid mesh faces.	43
Figure 36: Detailed view of fluid forces acting on the piston for resolution of F_{s1} F_{s2} ...	47
Figure 37: (A) 3D view of the piston and interacting components. (B) Free body diagram of the reciprocating piston. (C) Resolution of fluid forces.	48
Figure 38: Numerical algorithm for FSI coupled force balance model	50
Figure 39: Typical convergence plot from the FSI model.....	51
Figure 40: Displacement chamber pressures obtained through global fluid dynamic model for outlet pressures of 700 bar and 2500 bar. Shaft speed=1800 rpm	52
Figure 41: Instantaneous pressure field in lubricating gap domain over one shaft revolution using rigid body model. Operating condition: Outlet pressure=2500 bar, Shaft speed=1800 rpm	54
Figure 42: Instantaneous film thicknesses in lubricating gap domain over one shaft revolution using rigid body model. Operating condition: Outlet pressure=2500 bar, Shaft speed=1800 rpm	55
Figure 43: Instantaneous pressure field in lubricating gap domain over one shaft revolution using FSI model. Operating condition: Outlet pressure=2500 bar, Shaft speed=1800 rpm	56
Figure 44: Instantaneous film thicknesses in lubricating gap domain over one shaft revolution using FSI model. Operating condition: Outlet pressure=2500 bar, Shaft speed=1800 rpm	57

Figure	Page
Figure 45: Instantaneous elastic deformation in lubricating gap domain over one shaft revolution. <i>Operating condition: Outlet pressure=2500 bar, Shaft speed=1800 rpm</i>	58
Figure 46: Comparison of minimum film thickness generated using rigid body model and FSI model. <i>Operating condition: Outlet pressure=2500 bar, Shaft speed=1800 rpm</i>	59
Figure 47: Instantaneous leakage flow rate through a single piston-cylinder interface. <i>Operating condition: Outlet pressure=700 bar, Shaft speed=1800 rpm</i>	60
Figure 48: Instantaneous viscous friction force acting on a single piston. <i>Operating condition: Outlet pressure=700 bar, Shaft speed=1800 rpm</i>	60
Figure 49: Leakage flow and viscous power losses at different outlet pressures. <i>Shaft speed=1800 rpm</i>	61
Figure 50: Volumetric efficiencies and outlet flow rates at different outlet pressures. <i>Shaft speed=1800 rpm</i>	62
Figure 51: Leakage flow and viscous power losses at different piston-cylinder clearances. <i>Outlet pressure= 2500 bar, Shaft speed=1800 rpm</i>	63
Figure 52: Volumetric efficiency at different piston-cylinder clearances. <i>Outlet pressure = 2500 bar, Shaft speed=1800 rpm</i>	63
Figure 53: Instantaneous elastic deformation in lubricating gap domain over one shaft revolution for piston-cylinder radial clearance=2 μ m. <i>Operating condition: Outlet pressure=2500 bar, Shaft speed=1800 rpm</i>	64
Figure 54: Instantaneous film thickness over one shaft revolution for piston-cylinder radial clearance=2 μ m. <i>Outlet pressure = 2500 bar, Shaft speed=1800 rpm</i>	65
Figure 55: Minimum film thickness over one shaft revolution for piston-cylinder radial clearance =2 μ m. <i>Outlet pressure = 2500 bar, Shaft speed=1800 rpm</i>	66
Figure 56: Cam-piston lubricating interface. (a) Reference pump geometry (b) CAD illustration for the same	67

Figure	Page
Figure 57: Geometry of the cam piston contact interface. (a) in reference pump geometry (b) equivalent line contact geometry between a cylinder and a plane.....	68
Figure 58: Different configurations of cam-piston contact. (A) Hydrostatic slipper as analyzed in [1] (B) Roller support (C) Rolling element bearing.....	69
Figure 59: Lubricating gap domain between the piston and cylinder in line EHL.....	73
Figure 60: Lubricant model used in Jacobson, Hamrock [12].....	75
Figure 61: Range of contact loads between cam and piston at Outlet pressures: 700-2500 bar, Shaft speeds: 1200-1800 rpm	79
Figure 62: Solution algorithm flowchart for EHL line contact problem	80
Figure 63: Pressure field and film thickness (dimensionless) in a typical line EHL contact. Input parameters: $W' = 1.3 \times 10^{-4}$, $Ue = 1.0 \times 10^{-11}$, $SRR = 0$, $G = 5007$	82
Figure 64: Fluid viscosity variation in a typical line EHL contact. Input parameters: $W' = 1.3 \times 10^{-4}$, $Ue = 1.0 \times 10^{-11}$, $SRR = 0$, $G = 5007$	83
Figure 65: Dependence of pressure field on varying velocity parameter (Ue). $W' = 1.3 \times 10^{-4}$, $SRR = 0$, $G = 5007$	83
Figure 66: Friction coefficient using the Newtonian model. $Ue = 1.0 \times 10^{-11}$, $SRR = 0$, $G = 5007$	84
Figure 67: Comparison of friction coefficient as obtained using the Newtonian and non-Newtonian fluid model. $W' = 2.0478 \times 10^{-5}$, $Ue = 1.0 \times 10^{-11}$, $G = 5007$	85
Figure 68: Cam-piston interface with direct cam-piston contact. Resolution of velocity at contact point is shown on top right.	86
Figure 69: Input parameters for EHL friction model for <i>Pump outlet pressure: 700 bar, Shaft speed = 1800 rpm</i> . (A) Contact load in terms of Hertzian pressures. (B) Entrainment speed of lubricant. (C) Slide-roll ratio	88

Figure	Page
Figure 70: Results from friction model for <i>Pump outlet pressure: 700 bar, Shaft speed = 1800 rpm</i> . (A) Friction coefficient variation with shaft angle. (B) Minimum film thickness with varying shaft angle.	89
Figure 71: Cam-piston interface with rolling element bearings and outer race.	90
Figure 72: Instantaneous contact loads on each piston with maximum loaded piston shown for each shaft angle. <i>Pump outlet pressure: 700 bar, Shaft speed = 1800 rpm</i>	91
Figure 73: Input parameters for EHL friction model for <i>Pump outlet pressure: 700 bar, Shaft speed = 1800 rpm</i> . (A) Angular velocity of outer race (B) Entrainment speed of lubricant. (C) Contact load in terms of Hertzian pressures.	93
Figure 74: Results from friction model for $\theta = 0^\circ$. Input parameters: $W' = 1.97 \times 10^{-5}$, $Ue = 4.66 \times 10^{-13}$, $SRR = 0$ <i>Pump outlet pressure: 700 bar, Shaft speed = 1800 rpm</i>	93
Figure 75: Instantaneous pressure field in lubricating gap domain over one shaft revolution for direct contact type cam-piston interface. <i>Operating condition: Outlet pressure=700 bar, Shaft speed=1800 rpm</i>	95
Figure 76: Instantaneous film thicknesses in lubricating gap domain over one shaft revolution for direct contact type cam-piston interface. <i>Operating condition: Outlet pressure=700 bar, Shaft speed=1800 rpm</i>	96
Figure 77: Instantaneous pressure field in lubricating gap domain over one shaft revolution when pure rolling is assumed in the rolling element bearing type cam-piston interface. <i>Operating condition: Outlet pressure=700 bar, Shaft speed=1800 rpm</i>	97
Figure 78: Instantaneous film thicknesses in lubricating gap domain over one shaft revolution when pure rolling is assumed in the rolling element bearing type cam-piston interface. <i>Operating condition: Outlet pressure=700 bar, Shaft speed=1800 rpm</i>	98

Figure	Page
Figure 79: Piston eccentricities over one shaft revolution. (A) Direct cam-piston contact (B) Pure-rolling contact.....	99
Figure 80: Side loads/moments acting on piston. F_{Cf} : friction force, F_{CN} : normal contact force.....	99
Figure 81: ϵ_{el} field in piston-cylinder lubricating gap domain over one shaft revolution for direct cam-piston contact type interface. <i>Operating condition: Outlet pressure=700 bar, Shaft speed=1800 rpm</i>	100
Figure 82: ϵ_{el} field in piston-cylinder lubricating gap domain over one shaft revolution for pure rolling cam-piston contact. <i>Operating condition: Outlet pressure=700 bar, Shaft speed=1800 rpm</i>	101
Figure 83: Piston eccentricities over one shaft revolution when friction direction changes. <i>Operating condition: Outlet pressure=700 bar, Shaft speed=1800 rpm</i>	103
Figure 84: ϵ_{el} field in piston-cylinder lubricating gap domain for $\theta = 250^\circ$	103
Figure 85: Arbitrary control volume in space.....	114
Figure 86: Definition of lubricating gap used in the derivation. The top and the bottom surfaces are represented using the dotted lines and the reference plane ($z=0$) is represented in blue.	116

NOMENCLATURE

Symbol	Description	Units
$P_{DC,i}$	pressure in i^{th} displacement chamber	bar
$V_{DC,i}$	volume of i^{th} displacement chamber	m^3
K	bulk modulus of hydraulic oil	Pa
Q	flow rate	m^3/s
$Q_{rHP,i}$	flow rate from i^{th} displacement chamber to HP channel	m^3/s
$Q_{rHP,i}$	flow rate from LP channel to i^{th} displacement chamber	m^3/s
$Q_{\text{pist},i}$	piston-cylinder leakage flow rate in i^{th} displacement chamber	m^3/s
ΔP	pressure difference between displacement chamber and drain	bar
$A_{DC,i}$	cross-sectional area of i^{th} displacement chamber	m^2
s_p	piston displacement from bottom dead center	m
A_v	orifice area of check valve	m^2
k_{spr}	spring stiffness in ball check valves	N/m
x_v	valve opening	M
F_{jet}	flow forces acting in the ball check valve	N

F_{vf}	viscous friction acting on the ball in check valve	N
V_{val}	volume of fluid present in the valve opening area	m^3
P_{HP}	pressure in HP channel	bar
P_{LP}	pressure in LP channel	bar
V_{HP}	volume of HP channel	m^3
V_{LP}	volume of LP channel	m^3
ρ	density of hydraulic oil	kg/m^3
η	viscosity of hydraulic oil	Pa.s
α	discharge coefficient for orifice	-
L	length of the lubricating gap	m
h	lubricating gap height/ film thickness between solid surfaces	m
w_{gap}	width of lubricating gap region	m
u	velocity of solid surfaces in lubricating gap	m/s
Q_{prv}	flow rate through pressure relief valve at pump outlet	m^3/s
P_{dsg}	discharge pressure at outlet of pressure relief valve	bar
P_{out}	pressure at pump outlet	bar
$e1, e2$	piston eccentricities with respect to cylinder axis	m
l_{gap}	gap length of lubricating film region	m
x_A	Distance of cylinder face from origin	m
y_m	y co-ordinate of center of piston cross-section	m
h_g	Film thickness in gap domain	m

ϕ	angle along cylinder circumference	°
r_p	Piston radius	m
r_c	cylinder radius	m
p	Pressure generated in lubricating film domain	bar
\mathbf{V}	velocity vector	m/s
β_p	pressure coefficient for density	Pa-m ³ /Kg
α_p	pressure coefficient for viscosity	Pa ⁻¹
z	distance along gap film thickness	m
u, v	fluid velocity components in x,y direction in the gap region	m/s
\mathbf{n}	surface normal vector	-
Q_{leak}	leakage flow rate	m ³ /s
P_{visc}	power losses due to viscous friction	W
τ	shear stress	Pa
\mathbf{u}	deformation vector	M
\mathbf{F}	force vector	N
F	force	N
\mathbf{f}	body force vector	N
E	Young's modulus	Pa
ϵ	strain tensor	-
σ	stress tensor	Pa
ξ, λ	Lame's coefficients	Pa

ν	Poisson's ratio	-
Id	identity matrix	-
μ	friction coefficient	
θ	shaft angle	°
u_e	Entrainment velocity	m/s
u_s	sliding velocity	m/s
SRR	slide-roll ratio	-
δ	elastic deformation of solids	m
E'	effective modulus of elasticity of two contacting surfaces	Pa
$S(x)$	geometric separation between surfaces	m
w'	load per unit width in a line contact	N/m
R_x	radius of cylindrical surface in x direction	m
b	half Hertzian width	m
p_H	hertzian pressure	Pa
τ_L	limiting shear stress	Pa
τ_0	shear strength constant	-
γ	limiting shear strength proportionality constant	-
ω_{gs}, ω_{H0}	Under-relaxation parameters	-
P	dimensionless pressure	Pa
X	dimensionless x co-ordinate	-
H	dimensionless gap height	-

G	dimensionless material parameter	-
ω_i, ω_o	angular velocities of inner cam, outer race	rpm
r_o	radius of outer race	m
e	eccentricity in the rotating shaft	m

Subscripts	Description
-------------------	--------------------

t	top surface
b	bottom surface
g	gap region
p	piston
0	at ambient temperature and pressure conditions
visc	viscous friction
ref	reference
cp	contact point
a	surface a
b	surface b

Acronyms	Description
-----------------	--------------------

LP	Low Pressure
HP	High Pressure
FSI	Fluid Structure Interaction
EHL	Elastohydrodynamic Lubrication
HYGESim	Hydraulic Gear machine Simulator
CAD	Computer Aided Design

ODE	Ordinary Differential Equation
BDC	Bottom Dead Center
CFD	Computational Fluid Dynamics
FVM	Finite Volume Method
FEM	Finite Element Method
IM	Influence Matrix

ABSTRACT

Agarwal, Pulkit. M.S.M.E., Purdue University, December 2014. Modeling of High Pressure Radial Piston Pumps. Major Professor: Andrea Vacca, School of Mechanical Engineering

A comprehensive multi-domain simulation tool for investigating the operation of radial piston machines has been developed in the present study. The simulation tool is capable of analyzing the displacing action of the machine parts as well as the power losses occurring in the lubricating interfaces which makes it useful for supporting the design process of radial piston units. The reference machine analyzed in this study is a radial piston pump of rotating cam type design used for high pressure applications. Though the modeling process and calculations in this analysis pertain mostly to this specific design, the concepts involved and numerical procedure can be applied to generic designs of radial piston machines. A lumped parameter based model for complete hydraulic system of the pump has been formulated which can predict the main flow parameters in the pump namely flow rate and pressure at pump outlet. This model can be easily coupled with other hydraulic components present in a circuit to model the systems level performance of the machine. However, an improvement in pump design calls for a detailed investigation of internal components present in the pump specifically the lubricating interfaces present in the pump. The lumped parameter model is capable of generating boundary conditions to simulate the flow behavior in these lubricating interfaces. A separate model for piston-cylinder interface and cam-piston interface has been developed in this study to incorporate the detailed features involved in each of them.

The piston/cylinder lubricating interface represents one of the most critical design elements of radial piston machines. The interface performs the functions of a

hydrodynamic bearing by supporting the radial loads acting on the piston, seals the high pressure fluid in the displacement chamber and reduces friction between the moving parts. However, operating in the Elastohydrodynamic Lubrication (EHL) regime, it also represents one of the main sources of power loss due to viscous friction and leakage flow. An accurate prediction of instantaneous film thickness, pressure field, and load carrying ability is necessary to create more efficient interface designs. For this purpose, a fully coupled numerical solver has been developed to capture fluid-structure interaction phenomena in the lubricating interface at isothermal fluid conditions. This model considers the piston micro-motion during one complete cycle of pump operation.

The radial loads acting on the piston have a significant influence on piston micro-motion and hence the power losses in piston-cylinder interface. These loads are caused majorly by the friction forces existing between the cam and piston. A more accurate evaluation of performance parameters in the piston-cylinder interface can be achieved by calculating the instantaneous friction acting between the cam and piston under lubricating conditions. Different approaches for evaluating this friction coefficient were considered ranging from a simplified assumptions of pure sliding, pure rolling to a detailed analysis of lubricant flow between the cam-piston surfaces. For this purpose, a line contact EHL model was developed that can predict viscous friction forces generated between the cam and piston at changing surface velocities and contact loads. Also, instantaneous pressure field and film thickness can be predicted to a reasonable accuracy. This model is capable of analyzing multiple configurations of cam-piston interface design.

The numerical results presented in this thesis provide detailed information of the pump performance parameters at different operating conditions thereby confirming the utility of the simulation tool to support the design process of these units and assist in creation of more energy efficient pumps. Validation of the numerical model developed in this study with experimental results can be a part of future work.

CHAPTER 1. INTRODUCTION

1.1 Introduction to Radial Piston Machines

Radial piston machines are widely used positive displacement machines for high pressure applications and offer benefits of high efficiency together with a capability of withstanding very high loads at low speeds. They are characterized by a compact arrangement with high energy conversion efficiency. The disc shaped design of these units offers distinct advantages over other hydrostatic pumps while integrating with the gearboxes in automotive vehicles. Hence, these units are widely used in mobile applications to realize hydrostatic transmission systems along with stationary systems such as hydraulic presses. Radial piston pumps are commonly manufactured in two different types of designs, as shown in Figure 1,

- Rotating cam type design in which the cylinder housing remains stationary and the pistons rest on an inner cam in the center that describes eccentric motion
- Rotating cylinder type design in which the pistons rest on an outer stationary ring and the cylinder housing in the center rotates.

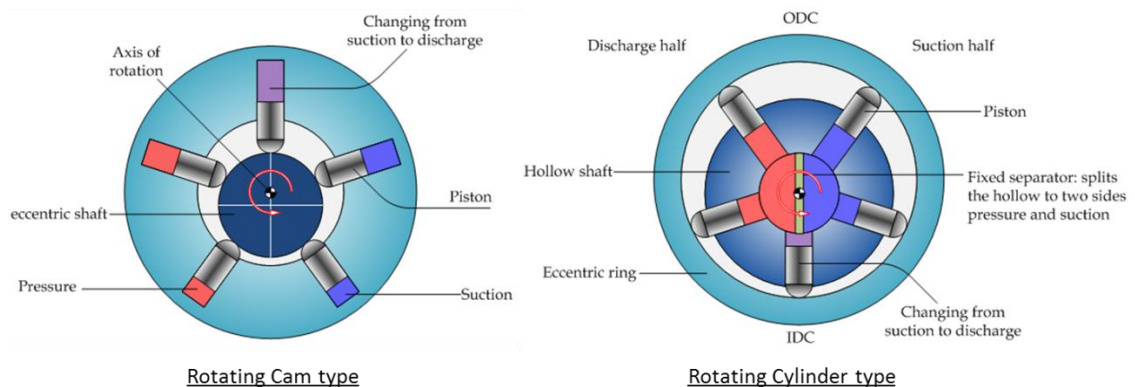


Figure 1: Common designs of radial piston pumps.

1.1.1 The Reference Pump Design

The specific pump chosen for the present study is a rotating cam type pump with rated operating pressure of 700 bar and displacement of 1.0 cc/rev. It finds application as a hydraulic power supply for portable tools such as clamping devices, cutting tools, mini presses and rock splitters. Figure 2 shows the top view of the radial piston pump assembly. The pump consists of 4 pistons radially arranged around an eccentric cam. Due to this eccentricity, a rotating motion in the cam imparts a reciprocating motion to the pistons that causes pumping of the fluid in and out of the displacement chambers. In order to minimize the relative motion between the cam and piston head surfaces to reduce friction and wear, rolling element bearings are placed between the rotating shaft and the outer race of the cam (not shown in the figure but present in actual design). However, that does not influence the kinematics of the piston motion significantly and the pump geometry considered in Figure 2 is sufficient for subsequent analysis.

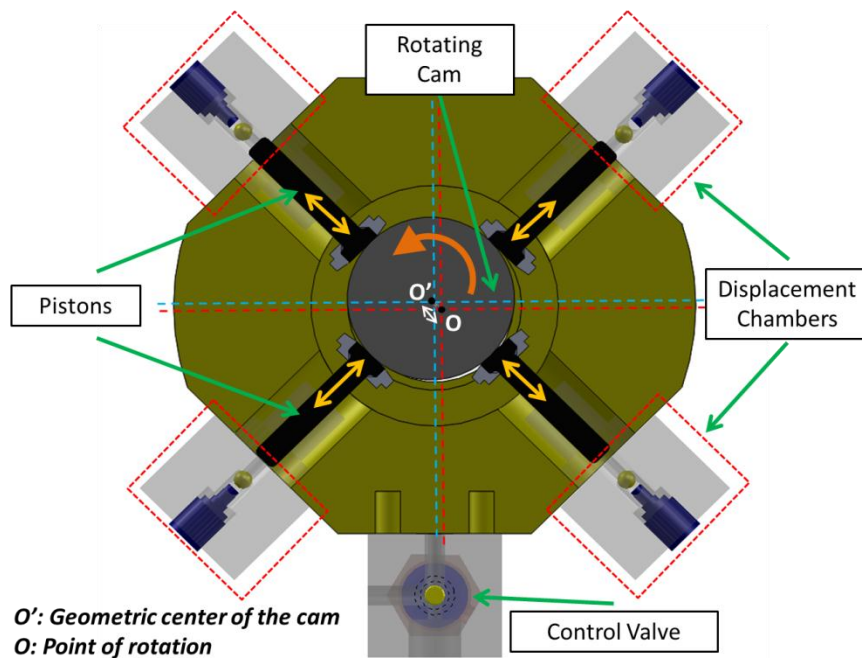


Figure 2: Top view of radial piston pump block.

The inlet and outlet ports of the radial piston pump are connected to two channels running through the casing of the pump as shown in Figure 3. There is a channel in lower part of the pump casing (LP Channel) which receives the fluid from the suction port at low pressure and feeds it to each of the 4 displacement chambers. Similarly, there is a channel in the upper part of the pump casing (HP Channel) which receives the fluid displaced by the pistons in each displacement chamber at high pressure set at delivery port of the pump. The HP Channel is connected to the hydraulic tools and a pressure relief valve which would maintain the fluid at a fixed pressure depending upon the requirement and the rating of the hoses.

Two ball check valves present in each of the displacement chambers control the entry and exit of the fluid in each displacement chamber. There is a ball check valve present at the inlet of the displacement chamber which opens only when the pressure in the displacement chamber is less than that of the LP channel. Similarly, there is an outlet ball check valve to control the exit of the high pressure fluid when the pressure in the displacement chamber exceeds the HP channel pressure. Figure 4 shows a detailed schematic of fluid flow through a single displacement chamber.

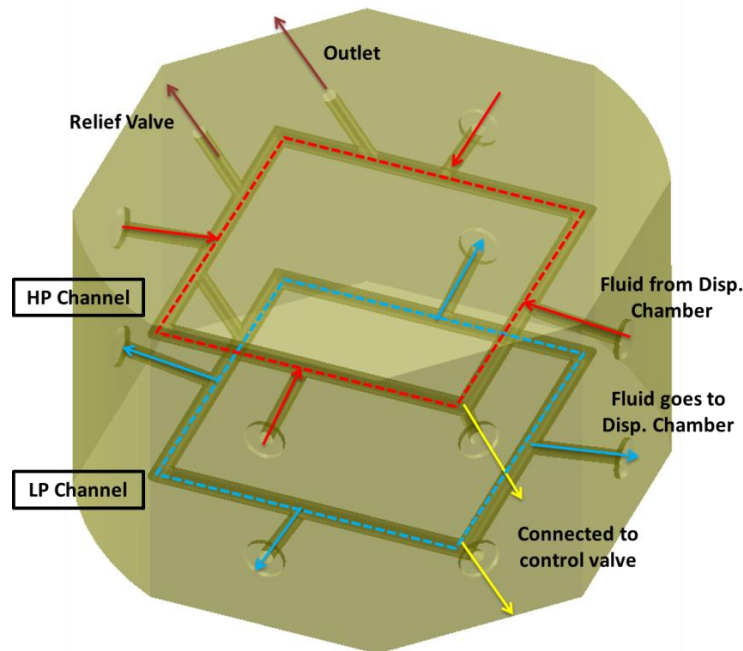


Figure 3: Inside view of pump housing.

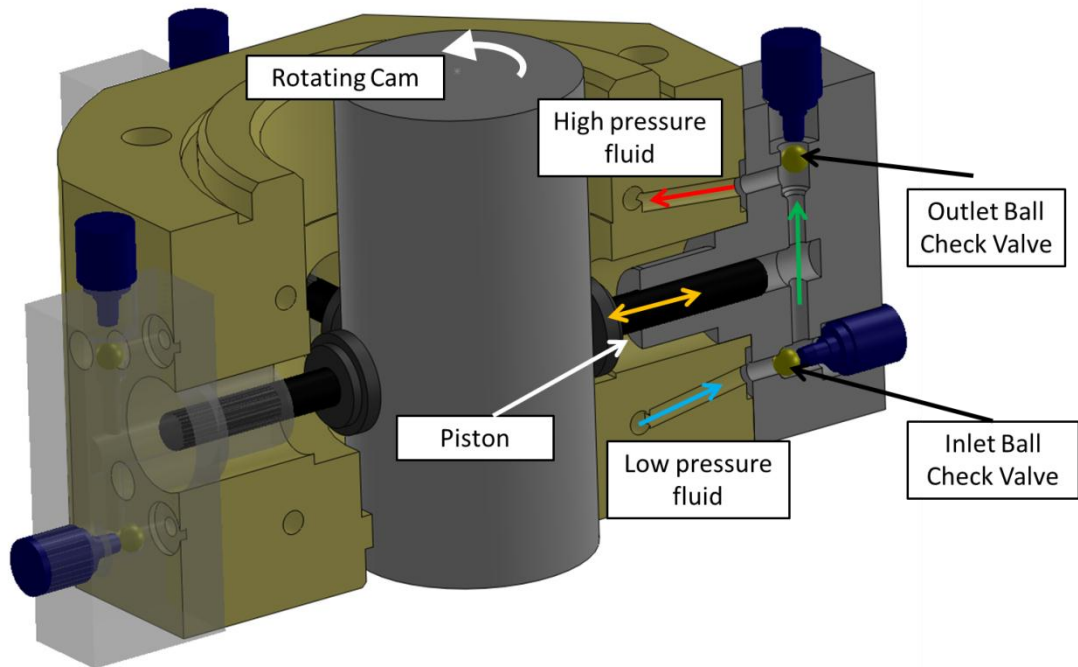


Figure 4: Detailed view of a displacement chamber.

1.2 Research Objectives

At present, the radial piston machines are largely designed by performing a number of experiments on a trial and error basis which is expensive and time consuming. This generates the need for simulation models that can model the complex physics associated with fluid flow through the pumps/motors and dynamic forces acting on machine parts so as to reduce the cost and time associated with these experiments. Analytical models for predicting the kinematic parameters for pump parts and simplified numerical models for generating basic flow are available in literature. However, there is a lack of detailed numerical models that can accurately predict the performance parameters associated with these machines namely the leakage flow and friction losses that play an important role in the design process.

The present study aims to fill this knowledge gap related to the modeling of radial piston units by presenting a comprehensive multi-domain simulation tool that can not only model the main flow through the unit but is also capable of evaluating the leakage flow

and the related power losses in the lubricating gaps in the pump. The simulation tool is formulated to be capable of generating the following parameters,

- a) The main flow parameters (flow rate, pressure ripple) through the displacement chambers and the inlet/outlet connections by considering the interaction of the pump with other elements in hydraulic circuit.
- b) The leakage and power losses associated with lubricating gap flow at the piston-cylinder interface by simulating the Fluid-Structure Interaction (FSI) phenomena.
- c) Instantaneous values of lubricant film pressure distribution and friction forces acting at the cam-piston interface.

Original contributions of this work include development of a fully coupled FSI model for piston-cylinder lubricating interface of radial piston machines and a generic numerical Elastohydrodynamic Lubrication (EHL) model for analyzing the friction forces generated in cam-piston interface. The effects of elastic deformation in modeling the piston-cylinder lubricating interface were considered in radial piston machines for the first time. The simulation tool developed in this research has immense potential to virtually design efficient radial piston machines through a careful consideration of flow physics involved and also presents a generic model to analyze novel/modified designs of radial piston machines.

The analysis of the reference radial piston pump configuration shows how the model can be used to predict the displacing action and main parameters of the flow through the pump, such as the flow fluctuation at pump delivery. This kind of analysis can lead to future research on the reduction of these fluctuations which is the key cause of fluid-borne noise generation. Similarly, a detailed analysis of the leakage flow and power losses occurring in the lubricating interfaces can be used to study the effect of the design changes to achieve specific objectives related to pump performance (such as to make the pump operational upto 2500 bar working pressures as considered in the present work).

1.3 Literature Overview

This section discusses the literature related to different aspects of the present research. The previous work done in analytical/numerical modeling of radial piston machines is presented along with the state of the art in modeling lubricating gaps in positive displacement machines and friction forces in non-conformal EHL contacts.

1.3.1 Modeling of Radial Piston Machines

Despite their large use in fluid power applications, there has been little reported work on modeling of radial piston machines. An analytical model of a radial piston motor was developed in [1] for evaluation of factors affecting motor performance including friction in ball joints. The work was focused on analysis of the different forces acting on pump parts and the motion parameters involved. The flow features in the motor were not studied. In [2, 3], an isothermal model for description of gap flow through radial piston machines was formulated. In [4], efficiency analysis of a radial piston pump was performed for a wind turbine transmission system. A detailed model for evaluating the main flow features was developed using a simplified model for lubricating gaps. In [5], a simulation model for radial piston motor was developed based on multibody dynamics. This model considers coupling between the different lubricating interfaces to generate the motion parameters for the motor.

In all the research works mentioned, the pump/motor parts are modeled as rigid bodies while the lubricating gaps if modeled assume hydrodynamic lubrication regime. The effects of elastic and thermal deformation of solid components are not considered while solving for pressure field in the lubricating gap. A detailed analysis of EHL friction existing between cam-piston has not been performed in previous studies. Also, these models do not consider higher operating pressures (>700 bar).

There has been significant work on digital displacement control of radial piston machines [6] for better response speed and energy efficiency. This work has been focused on the system performance of the machine and does not involve a component level modeling of machine parts.

1.3.2 Lumped Parameter Modeling of Positive Displacement Machines

Though radial piston machines are unique in design and operation, the displacing action in these machines is similar to axial piston unit and is achieved by reciprocating motion generated in each of the pistons. There is significant literature available on axial piston and gear units which have been studied in varied detail in different works. Evaluation of the main flow features in positive displacement machines can be easily performed by developing a simplified lumped parameter model for each chamber/volume space. This approach has been utilized frequently in studying the gear machines and axial piston machines in the past [7-12]. The pressure transients in external gear pumps were analyzed in [7]. Also, the development of the simulation tool HYGESim, which is capable of generating flow parameters in external gear machines, is described in [8]. Similar work on gerotor units has been performed in [10]. [11-12] describe simulation models for axial piston machines which have been followed by a series of research works on advanced modeling of lubricating gaps utilizing the main flow results as boundary conditions. The lumped parameter approach as applied to modeling of radial piston machines is described in detail in CHAPTER 3.

1.3.3 Lubricating Gap Model for Positive Displacement Machines

The modeling of lubricating gaps in positive displacement machines, specifically axial piston and gear pumps, has been a subject of active research in last few years. There have been individual studies on the different lubricating interfaces in axial piston machines that include the works performed on the piston-cylinder interface [13,14], the slipper-swash plate interface [15,16] and the cylinder block-valve plate interface [17,18] that have resulted in accurate prediction of pump performance parameters. Similar studies have been performed on the lubricating interface between the gears and lateral bushes in external gear machines [19,20]. The effects of elastic and thermal deformation have been found to be significant in determining the features of operation as well as the performance parameters of axial piston pumps and gear pumps [21-23]. Utilizing similar principles, a FSI model for piston-cylinder lubricating interface in radial piston machines was developed in this study which is discussed in CHAPTER 4.

1.3.4 Friction Modeling in Line EHL

The modeling of pressure generation, gap film thickness and friction/traction forces in lubricated line contacts operating in EHL has been a major topic of research in tribology since last 40 years. A large number of experimental/empirical as well as numerical methods have been formulated to evaluate the above mentioned parameters in line contacts. Early EHL models [24-27] that developed new solution techniques and laid down the fundamental theories for EHL regime were largely based on Newtonian fluid assumption, smooth surfaces and rolling velocities only. Also, the major experimental studies were focused on line contact film thickness measurements using twin disc/roller machines [28, 29] which confirmed the basic trends in EHL. On the other hand, increase in computing power in last 20 years has seen development of high fidelity simulation models for line and point contact EHL/mixed lubrication problems [30-34] that incorporate the non-Newtonian fluid rheology models, thermal effects and the influence of surface asperities [35-37]. A detailed review of the important studies that have been performed on EHL in non-conformal surfaces can be found in [38].

Despite the availability of these highly sophisticated numerical models that can predict the film thickness and pressure distribution in contact zone to a reasonable accuracy, accurate prediction of friction/traction in heavily loaded mixed EHL contacts has always been a challenge with few numerical models existing for the same. However, a number of numerical/empirical studies on friction calculations in full-film EHL contacts have been conducted [39-44] that enable precise calculation of viscous friction acting between the lubricated surfaces. The present research utilizes these principles in developing a generic friction model for cam-piston interface in radial piston machines operating in EHL regime.

CHAPTER 2. STRUCTURE OF THE SIMULATION MODEL

This chapter discusses the overall structure of the multi-domain simulation tool which was developed in this study to evaluate the different flow features and physics involved in operation of radial piston pumps. The simulation tool is comprehensive and operates by linking together a number of modules each of which performs a different computation process. Figure 5 shows the complete schematic of the multi-domain simulation tool with the different modules. The connections between the blocks depict exchange of data between the individual modules.

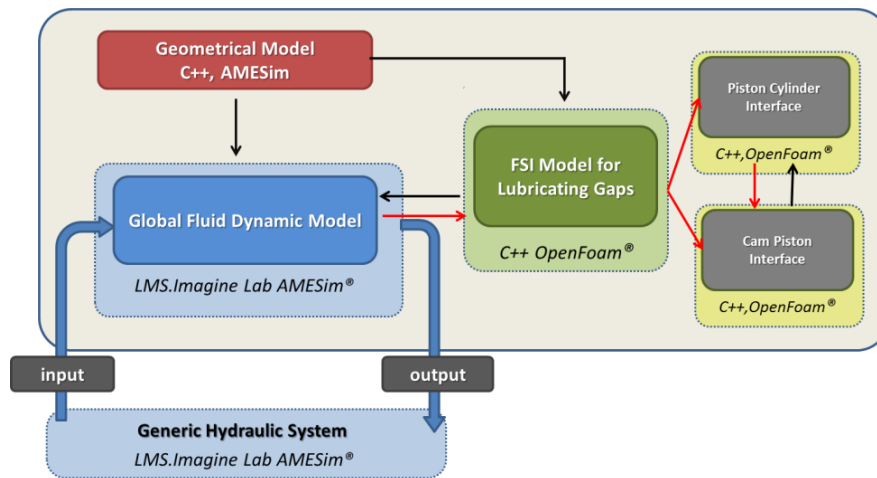


Figure 5: Schematic of the multi-domain simulation tool for modeling radial piston machines.

As seen in the figure, it consists of a geometrical model that calculates the kinematic parameters for motion of cam and piston. This is coupled to the global fluid dynamic model that calculates the basic flow parameters such as flow rate, pressure ripple at pump outlet and also the instantaneous pressures in each of the displacement chambers. For

accurate prediction of flow parameters through the fluid dynamic model, it is important to consider the other components present in the hydraulic system that might affect the flow conditions in the main pump under study. This is handled by a module for generic hydraulic systems that can consist of any number of valves/pumps or other components.

The second part of the simulation tool comprises a lubricating gap model which is essential for accurate prediction of leakage and hence the performance parameters. This module is divided into separate sub-modules for piston-cylinder interface and cam-piston interface. As shown in Figure 5, the different modules of the simulation tool interact closely with each other by exchanging information. The generic hydraulic system is fully coupled to the global fluid dynamic model to generate the main flow parameters whereas the kinematic parameters generated by the geometric model are used as inputs by both the fluid dynamic and lubricating gap modules. Displacement chamber pressures from the fluid dynamic model are used as boundary conditions for the piston-cylinder gap module which receives friction forces as inputs from the cam-piston model. A detailed insight into each of the main modules is provided in the subsequent chapters. The following section provides details of the geometrical model.

2.1 Geometric Model

The development of the geometric model is essential for calculating the kinematic parameters required as inputs by the other modules of the simulation tool for evaluation of flow parameters. The model is built using C++ and can handle cam and piston surfaces of any arbitrary shapes. It can be easily incorporated into AMESim which facilitates easy coupling with the global fluid dynamic model built in the same framework. Figure 6 shows the geometry of the moving components in the pump that are involved in calculating motion parameters for the reciprocating piston from the eccentric motion of shaft (cam). The CAD geometries of cam and piston are required as inputs along with dimensions for displacement chamber parts.

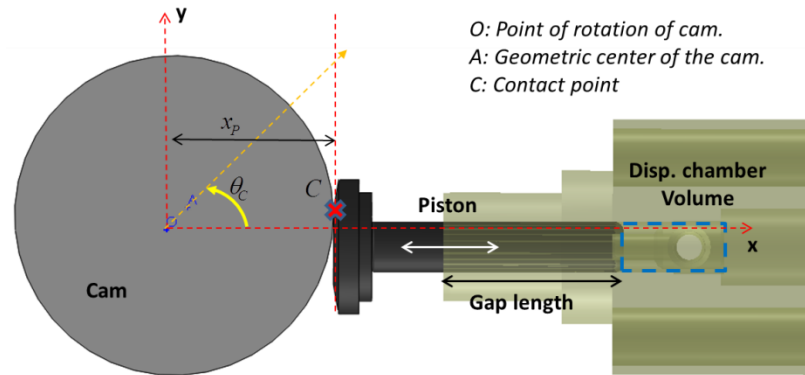


Figure 6: Illustration of geometrical parameters to determine piston position (x_p) as a function of cam rotation (θ_p).

The geometric model is capable of generating precise values of kinematic/motion parameters for different modules of simulation tool which are listed below,

1. **Global fluid dynamic model:** Generates instantaneous values of piston displacement, displacement chamber volume and piston translational velocity.
2. **Piston-Cylinder lubricating gap model:** Calculates the instantaneous length of lubricating oil film between piston and cylinder and co-ordinates of the contact point between the cam and piston since the contact forces act at this point.
3. **Cam-piston gap model:** Contact point coordinates are required to calculate the surface velocity parameters for EHL line contact model.

The kinematic parameters generated for the reference radial piston pump using the geometric model are shown now. The piston stroke is dependent on the amount of eccentricity present in the rotating cam (2.5 mm in the reference design). Figure 7 shows the instantaneous piston displacement for each displacement chamber present in reference pump design when the eccentric cam/shaft is rotated. A shaft angle of 0° corresponds to piston 1 starting from its bottom dead center (BDC). The variation in piston-cylinder gap length and piston velocity in one cycle of shaft revolution can be seen in Figure 8 and Figure 9 when the shaft speed of the pump is 1200 rpm.

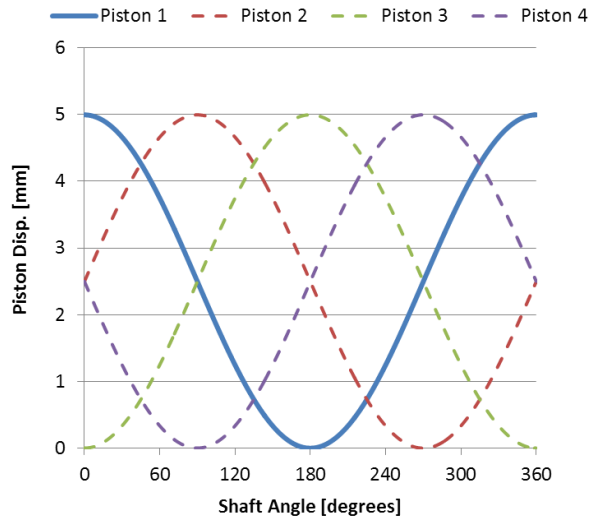


Figure 7: Instantaneous piston displacements in 1 cycle of shaft revolution.

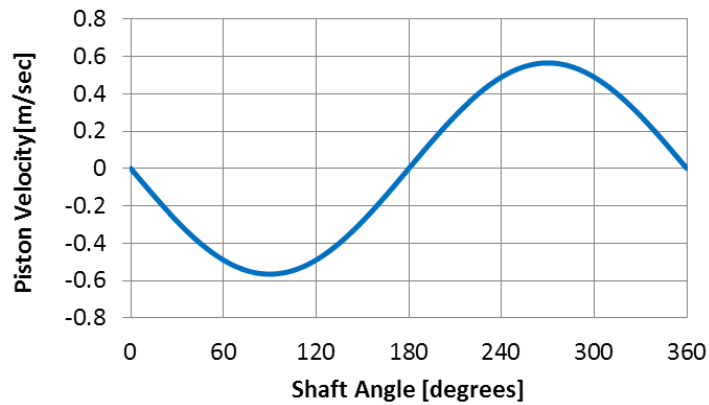


Figure 8: Piston velocity at varying shaft angles for complete pump cycle. *Shaft speed=1200 rpm.*

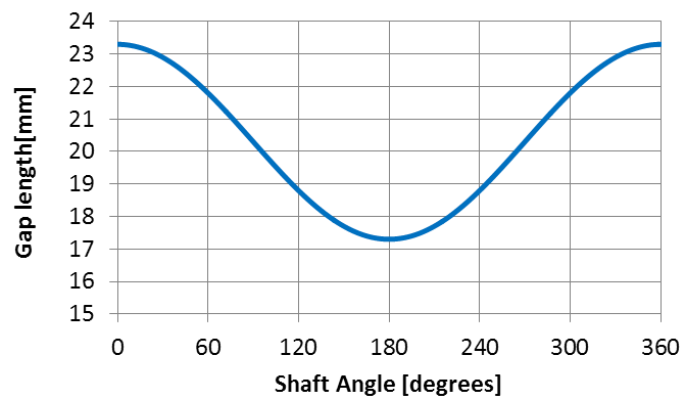


Figure 9: Piston-cylinder gap length vs shaft angle for complete pump cycle. *Shaft speed=1200 rpm.*

CHAPTER 3. GLOBAL FLUID DYNAMIC MODEL

The global fluid dynamic model is the central component of the multi-domain simulation tool and strongly influences the functioning of other modules. This model is used to analyze the fluid flow through the complete hydraulic system of the pump that includes the different displacement chambers, check valves, low and high pressure channels and the inlet/outlet connections. The primary output of the model includes the main flow parameters in the pump namely flow rate, pressure at the pump outlet as well in each of the displacement chambers. It is based on the lumped parameter approach which is described in detail in the following section.

3.1 Lumped Parameter Approach

In order to evaluate the flow features through different sections, the radial piston machine can be divided into separate control volumes corresponding to each displacement chamber and LP/HP channels. Figure 10 represents the schematic of the lumped parameter model used to analyze the reference design of the radial piston pump. The individual control volumes in the pump consist of the four displacement chambers and two channels while orifices are used to model the flow connections between these different control volumes. According to the lumped parameter approach, the fluid properties in each of these control volumes are assumed to be independent of spatial parameters and are considered functions of time only. This approach has been found to generate results to an acceptable accuracy in axial piston and external gear machines in the past [7, 11].

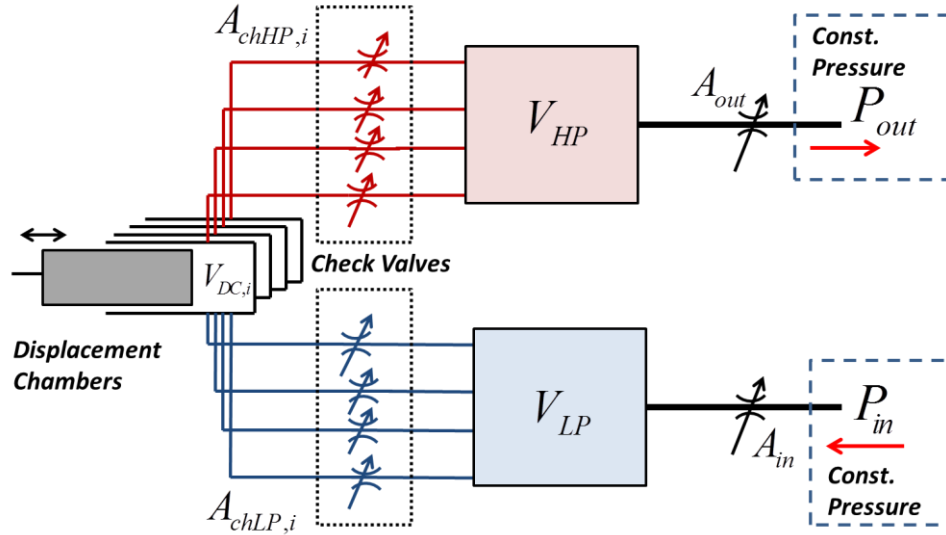


Figure 10: Schematic of the lumped parameter model for the reference pump design.

In order to solve for fluid flow parameters across the complete pump system, flow equations for each of the components have to be coupled together to formulate a solution procedure. The rate of change of pressure in each control volume can be obtained using the pressure built-up equation. The derivation of the pressure built-up equation follows from the conservation of mass and fluid state equation which is detailed in APPENDIX A. The pressure built-up equation for each displacement chamber can be described as follows,

$$\frac{dP_{DC,i}}{dt} = \frac{K}{V_{DC,i}} \left[-\frac{dV_{DC,i}}{dt} - (Q_{rHP,i} + Q_{rLP,i} + Q_{pist,i}) \right] \quad (3.1)$$

$\frac{dV_{DC,i}}{dt}$ represents the rate of change of displacement chamber volume and can be represented by the following equation where $\frac{ds_P}{dt}$ is the instantaneous piston velocity that is generated by the geometric model as already discussed in the previous chapter.

$$\frac{dV_{DC,i}}{dt} = A_{DC,i} \frac{ds_P}{dt} + \frac{dV_{HPv,i}}{dt} + \frac{dV_{LPv,i}}{dt} \quad (3.2)$$

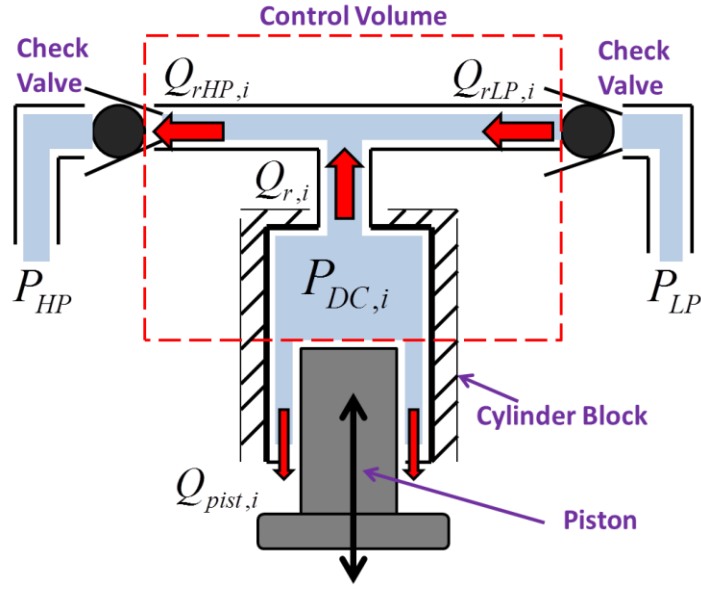


Figure 11: The displacement chamber control volume.

Solving for pressure distribution using Equation (3.1) requires the flow rate terms across each of the check valves present near the displacement chamber ($Q_{rHP,i}$, $Q_{rLP,i}$). These are solved by using orifice flow equations for turbulent flow as follows,

$$Q_{rHP,i} = \alpha A_{HPv,i} \sqrt{\frac{2|P_{DC,i} - P_{HP}|}{\rho}} \text{sgn}(P_{DC,i} - P_{HP}) \quad (3.3)$$

$$Q_{rLP,i} = \alpha A_{LPv,i} \sqrt{\frac{2|P_{DC,i} - P_{LP}|}{\rho}} \text{sgn}(P_{DC,i} - P_{LP}) \quad (3.4)$$

Where, $A_{HPv,i}$ represents the orifice area of connection between the HP channel and displacement chamber which is determined by the opening of the outlet ball check valve as can be seen in Figure 12. Similarly, $A_{LPv,i}$ represents opening area of inlet ball check valve. The valve opening areas in orifice flow equations were evaluated by a careful selection of AMESim libraries in which the effects of geometry are included in detail. The $\frac{dV_{val}}{dt}$ terms in Equation (3.2) take into account the volume change due to movement of the ball in the check valve and are incorporated in the valve models.

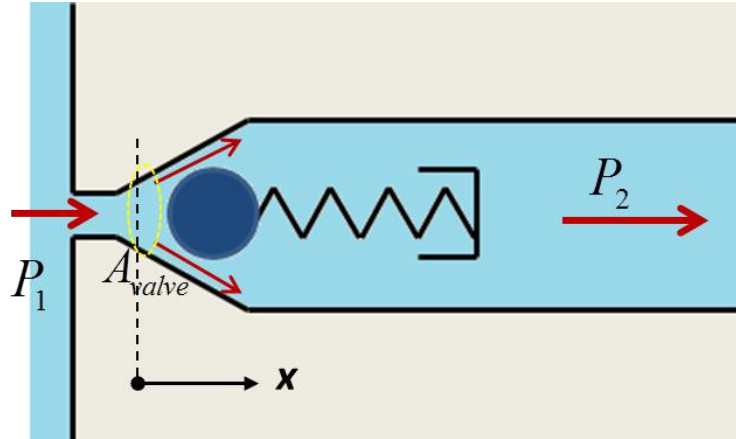


Figure 12: Geometrical parameters and force analysis of a ball check valve with conical seat.

Figure 12 shows the different forces acting on the ball during a typical pump operation. The orifice area in the check valves ($A_{HPv,i}$, $A_{LPv,i}$) is obtained after calculating the valve opening (x_v) by solving the equations of motion for the ball,

$$-k_{spr}(x_v + x_0) + P_2A_2 - P_1A_1 - F_{jet} - F_{vf} = 0 \quad (3.5)$$

where x_0 is the pre-compression in the spring, A_1, A_2 are the ball areas on which the pressures P_1, P_2 act respectively, F_{jet} represent the flow forces acting on the ball which try to close the valve and F_{vf} is the viscous friction.

The flow forces (F_{jet}) are calculated through the in-built libraries in AMESim that are based on analytical relations [45]. The dynamics of the check valve are highly dependent on the viscous forces F_{vf} which add damping to the motion of the ball to reduce the ball acceleration. An accurate estimation of these viscous forces would require experimental measurements to be conducted. To simplify the analysis, an empirical value of friction coefficient was chosen [46] based on 5-10% damping which is typical in hydro-mechanical systems and resulted in smooth opening and closing of the check valves.

Flow through the HP and LP channel volumes are analyzed using a similar set of equations. Figure 13 shows the detailed view of the HP channel control volume and its flow connections with the outlet, the four displacement chambers and a pressure relief

valve. Equations governing the HP system are described below while a similar procedure can be adopted to derive equations for LP channel,

$$\frac{dP_{HP}}{dt} = \frac{K}{V_{HP}} \left[- \sum_{i=1}^4 Q_{rHP,i} - Q_{out} - Q_{prv} \right] \quad (3.6)$$

$$Q_{prvHP} = \alpha A_{HPv} \sqrt{\frac{2|P_{HP} - P_{dsg}|}{\rho}} \text{sgn}(P_{HP} - P_{dsg}) \quad (3.7)$$

$$Q_{out} = \alpha A_{out} \sqrt{\frac{2|P_{HP} - P_{out}|}{\rho}} \text{sgn}(P_{HP} - P_{out}) \quad (3.8)$$

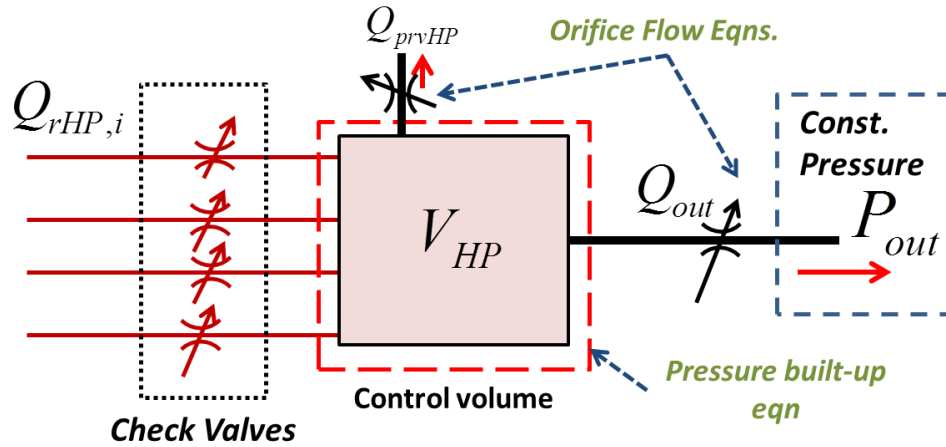


Figure 13: HP channel control volume.

The leakage flow rate through each displacement chamber ($Q_{pist,i}$) can be calculated using a laminar flow equation (considering fully developed laminar flow and relative motion between surfaces),

$$Q_{pist,i} = w_{gap} \left[- \frac{h^3}{12\eta} \left(\frac{\Delta P}{L} \right) + \frac{hu}{2} \right] \quad (3.9)$$

where, u is the velocity of the wall, L is the gap length, h is the gap height and w_{gap} is the gap width.

This represents a simplified approach to generate an initial guess for the leakage flow for obtaining displacement chamber pressures which are used as boundary conditions for the lubricating gap models. The solution process for determining the flow parameters in the pump is described in the next section. The FSI model for piston-cylinder interface then evaluates the accurate leakages taking into account the piston micro-motion and hydrodynamic effects which are used to refine the displacement chambers pressures again thereby forming a coupled system. However, usually the leakages observed in the pump design do not require a strong coupling and a few iterations are enough to obtain an accurate solution.

3.2 Solution Process

The Equations (3.1) to (3.9) represent a system of ODEs which requires coupling and solution using an iterative solver. In the present study, the commercial solver AMESim was used to model the individual components in the circuit and solve the system of equations to calculate system parameters. Figure 14 shows the different components involved in modeling a single displacement chamber while implementing in AMESim. The complete hydraulic system of the pump for the same can be seen in Figure 15. After computations are performed for multiple shaft revolutions, convergence is obtained when simulation results are periodic for each subsequent revolution.

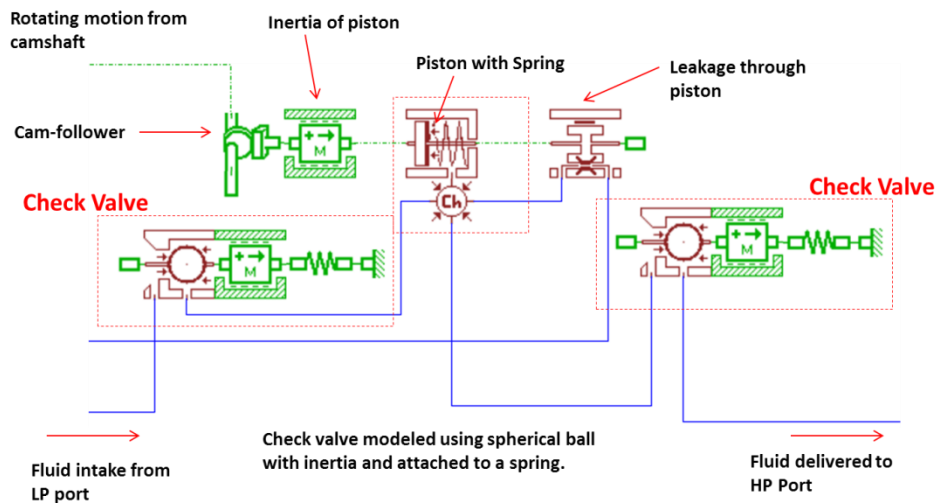


Figure 14: Flow connections through a single displacement chamber.

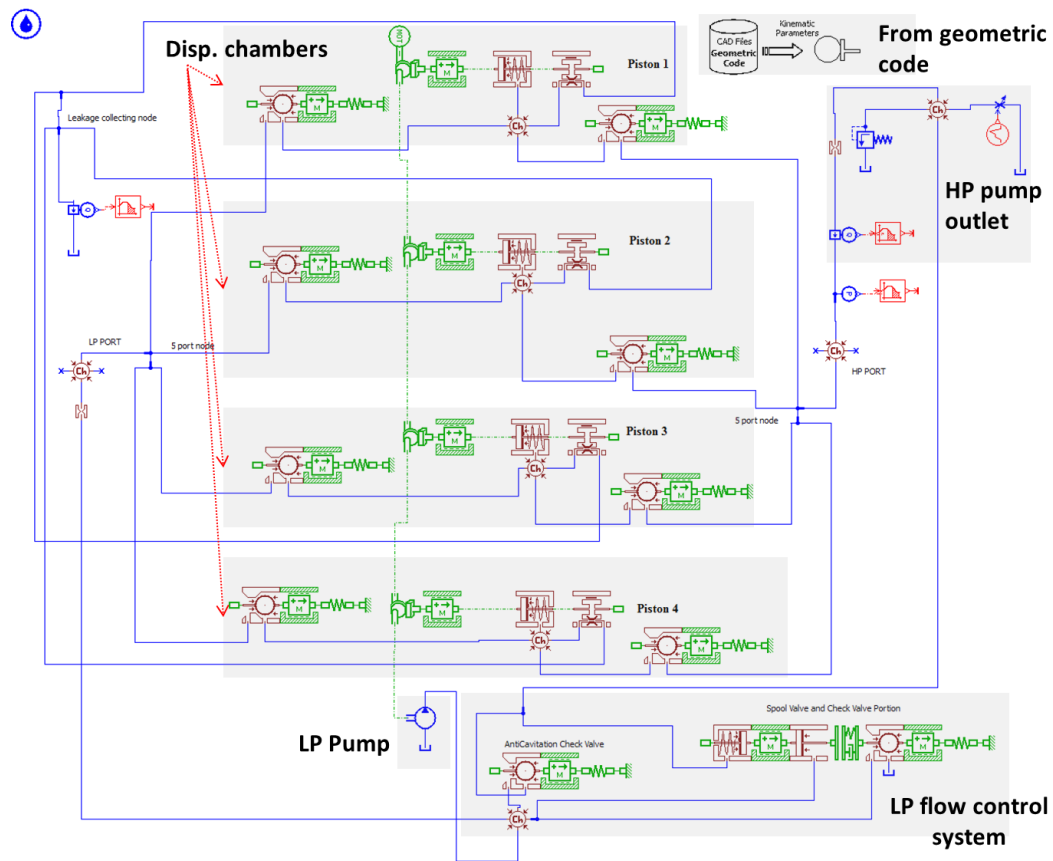


Figure 15: AMESim implementation of the complete hydraulic system.

Besides the individual components of the radial piston pump, the schematic shows components of a low pressure flow control system present at pump inlet which was implemented in conjunction with the main pump. The details of this system will be explained in section 3.4.

3.3 Results

Simulation results depicting the different flow features of the radial piston pump are now detailed. The global fluid dynamic model is capable of simulating the pump at a wide range of operating conditions corresponding to mean outlet pressure and shaft speed. Table 1 shows the four operating conditions for which the simulation results were generated. The pressure generated at the pump outlet along with the flow rate is depicted

in Figure 16 - Figure 19. It can be seen that each shaft revolution in the pump operation generates four pressure peaks at the outlet which are a result of simultaneous impact of the four displacement chambers operating together. ISO VG 32 hydraulic oil is used as the working fluid for all simulations.

Table 1: Operating conditions used for generating results from global fluid dynamic model.

Operating condition	Mean outlet pressure (bar)	Shaft speed (rpm)
1	700	1200
2	700	1800
3	2500	1200
4	2500	1800

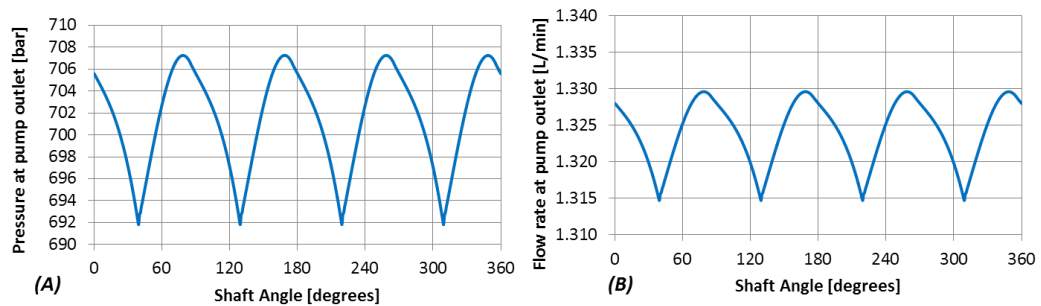


Figure 16: Pressure (A) and flow rate (B) at pump outlet as a function of shaft angle for operating condition 1.

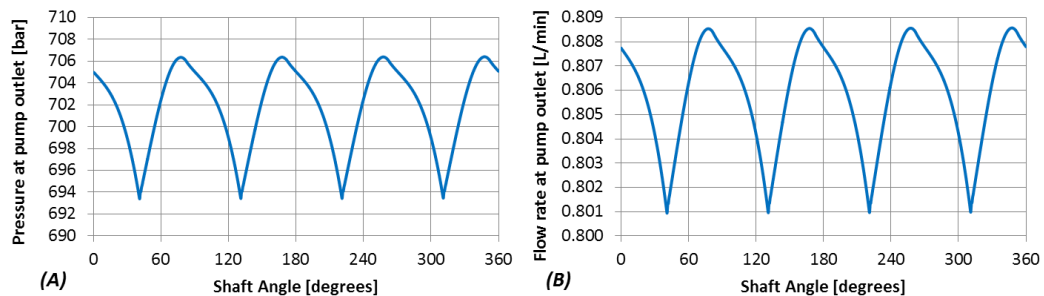


Figure 17: Pressure (A) and flow rate (B) at pump outlet as a function of shaft angle for operating condition 2.

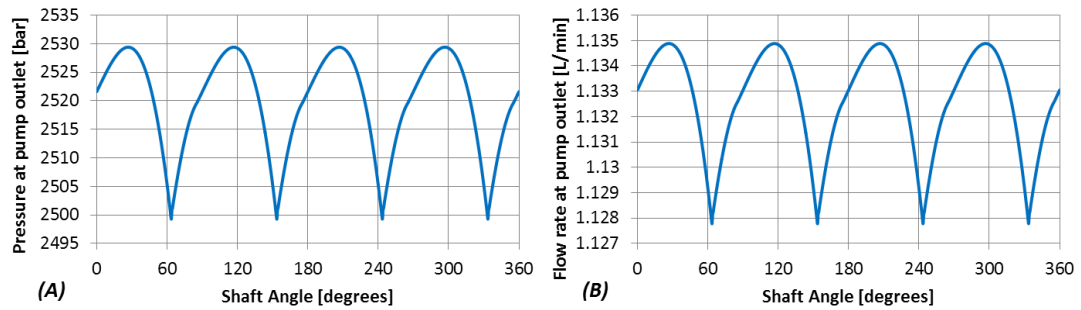


Figure 18: Pressure (A) and flow rate (B) at pump outlet as a function of shaft angle for operating condition 3.

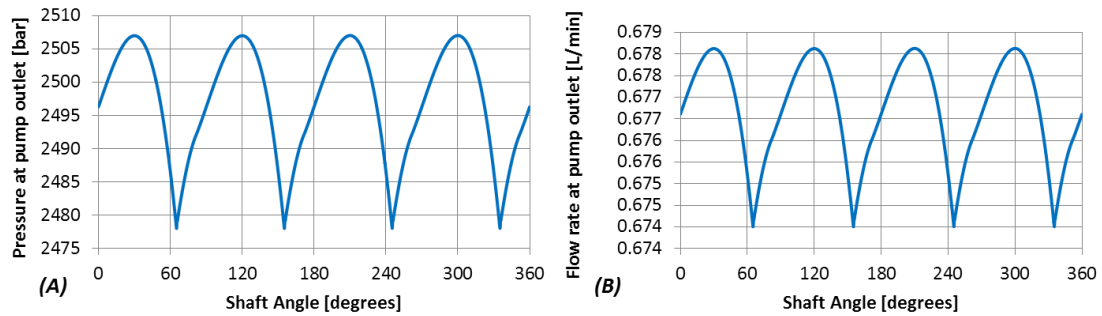


Figure 19: Pressure (A) and flow rate (B) at pump outlet as a function of shaft angle for operating condition 4.

The flow variation in one cycle of shaft rotation is in the form of a ripple with four peaks. This is due to the presence of four displacement chambers each of which generate discontinuous flow that is governed by the opening and closing of check valves. Figure 20 shows the flow ripple at pump outlet for operating condition 1 (refer Table 1) along with instantaneous flow rate in each of the displacement chambers. It can be seen that the net flow rate at the pump outlet is a resultant of the individual flows in displacement chambers.

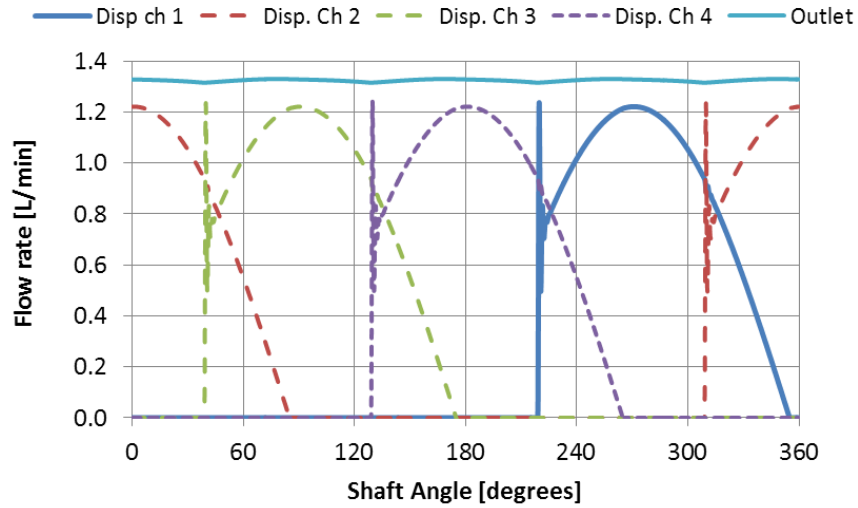


Figure 20: Flow rate comparison of four displacement chambers in 1 cycle of shaft rotation.

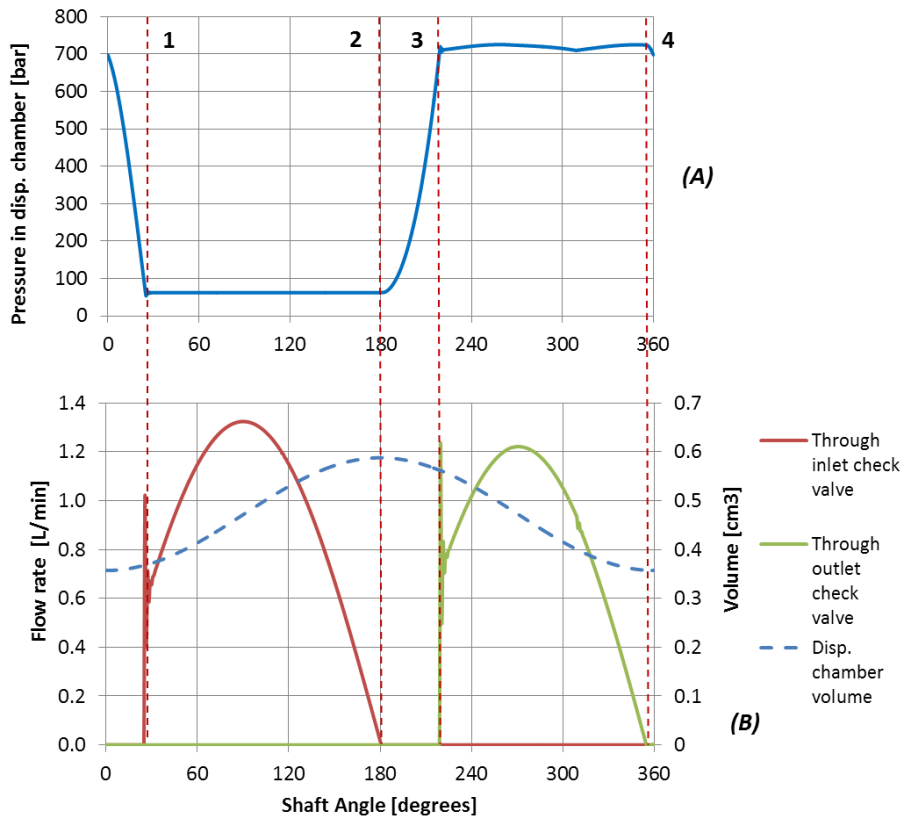


Figure 21: Instantaneous pressures in displacement chamber (A) and flow rate through check valves (B) at operating condition 1. Valve timings: (1) Inlet valve opens, (2) inlet valve closes, (3) Outlet valve opens, (4) Outlet valve closes.

The global fluid model is also capable of predicting the instantaneous pressure in each of the displacement chambers as shown in Figure 21. Also shown along with the pressure variation is the timing of the opening and closing of the inlet and outlet ball check valves during steady state operation. As the inlet check valve opens, the built-up pressure is released for fluid intake at constant pressure. Closing of the inlet valve is followed by a rapid increase in pressure as the piston is moving towards BDC at this time. When the pressure is sufficient to open the outlet check valve, discharge of fluid occurs at high pressure and the cycle repeats.

The corresponding flow rates through the check valves are also shown in Figure 21. It can be seen that the flow rate through inlet check valve is slightly greater than that of outlet check valve as some part of the fluid intake passes as leakage flow between the piston and cylinder.

The simulation results described above were obtained through a simplified prediction of the leakage flows based on laminar flow assumption in each piston-cylinder interface which overpredicts the leakage values as it doesn't consider the effects of hydrodynamic pressure generation due to piston micro-motion. Though a small change in leakage flow through the piston-cylinder lubricating gap doesn't affect the main flow through the unit, it certainly affects the power losses due to shear and volumetric loss that characterize the durability of the unit. This calls for a detailed analysis for the flow through the gap domain using a CFD model which is discussed in the next chapter.

3.4 Generic Hydraulic System

In order to consider the effects of the other hydraulic components present in the system on the performance of the pump, a low pressure flow control system was modeled in conjunction with the global fluid dynamic model. In this study, a hydraulic system used for operating high pressure hydraulic tools was chosen for analysis since the reference pump design is typically used for that purpose.

3.4.1 Description

High pressure hydraulic tools such as bolt tensioners, rock splitters, cutting tools often operate on repeated cycles with short duration operation. These tools typically require a low pressure and high flow rate in the beginning wherein the movable parts grip the required area and then a high pressure to produce sufficient force to break the material at low speed. To enhance the system controllability, a discrete variable flow supply group is used to meet separate demands for these two operating conditions.

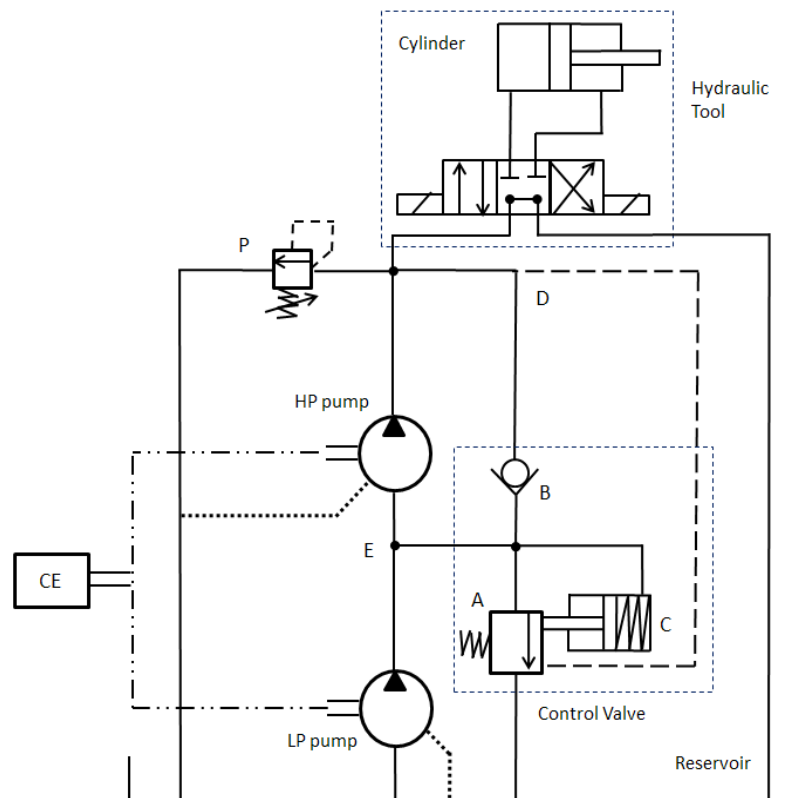


Figure 22: ISO schematic of the complete hydraulic system for operating high pressure hydraulic tools.

The system (Figure 22) utilizes a gear pump to provide fluid at a higher flow rate during the first stage of operation of the tools, which occur at relatively low pressures. Once the hydraulic cylinder/actuator starts the main function of the tool, the load suddenly increases and a lower flow rate is required to decrease the speed. This demand is met by a radial piston pump of rotating cam design. A specific hydraulic system is used to control

the fluid flow through the two pumps and the hydraulic actuator, the details which are shown in Figure 22. Both the radial piston pump (HP pump) and the gear pump (LP pump) are connected to a control system that consists of multiple valves incorporated in a single block (Figure 23), which carries out the function of performing directional control of the flow to optimize the energy consumption.

The fluid control system comprises three main components that regulate the direction of fluid flow through the circuit. The pressure relief valve (A) is actuated by a pilot pressure line from the outlet of the HP pump. Besides there is a spring loaded spool (C) that is actuated by pressure in the region between the LP and HP pump (Node E). A check valve (B) connects the both the regions together.

The functioning of these components can be understood in context of pump operation mode. During the low pressure operation of the tool, when there is a requirement of high flow rate, the check valve B opens to bypass the flow from the LP pump to the cylinder. The HP pump does not generate pressure during this time.

When the hydraulic cylinder receives high load, there is a pressure buildup in the cylinder which then propagates inside the valve (node D to node E). The pressure can rise up to a maximum limit, set by the pressure relief valve P, which causes a discharge of the excess flow preventing the pressure in the region A to rise above the limiting value. This lead to the closure of the check valve B so that in the region A, a constant pressure of low magnitude (10-15 bar) is established. The pressure at the outlet will rise up to the maximum rated value set by the pressure relief valve. At this stage, the high pressure required by the outlet is generated by the radial piston HP pump while the LP pump performs the function of supplying the fluid at an elevated pressure to avoid cavitation during the suction phases of the radial piston pump.

The described flow regulation achieved by the control valve of Figure 22 ensures minimum energy waste as the excess flow during the high pressure operation is discharged at low pressure.

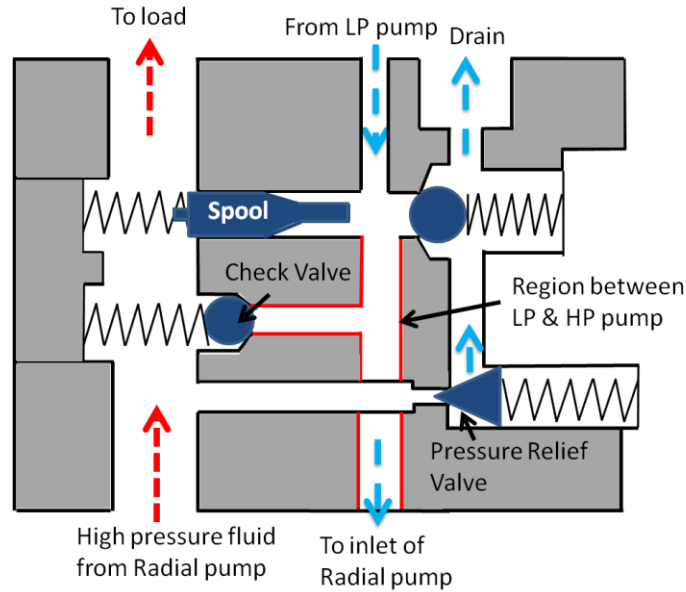


Figure 23: Structural details of the spool block.

The hydraulic system for the tool operation was modeled in AMESim as well and coupled with the global fluid dynamic model for the radial piston pump as was shown in Figure 15. The LP charge pump is modeled as a flow generator only since we are not concerned with operating details.

3.4.2 Results

The simulation model developed in AMESim is capable of predicting flow parameters for the complete system that includes the HP pump, LP pump and components of fluid control system. Figure 24 shows the variation of flow rate at the system outlet with the changing pressure at the same node. It can be seen through the figure that when the system pressure is below the value P^* (determined by pre-load setting of the spring in spool C of Figure 22), the flow rate at the system outlet is high as the tool is in low pressure/high speed operation. Once the system pressure exceeds P^* , the flow rate reduces considerably as the tool now requires high pressure generation for clamping operation. This reduction in flow is carried out by the pressure relief valve A (refer Figure 22) which is actuated by system outlet pressure.

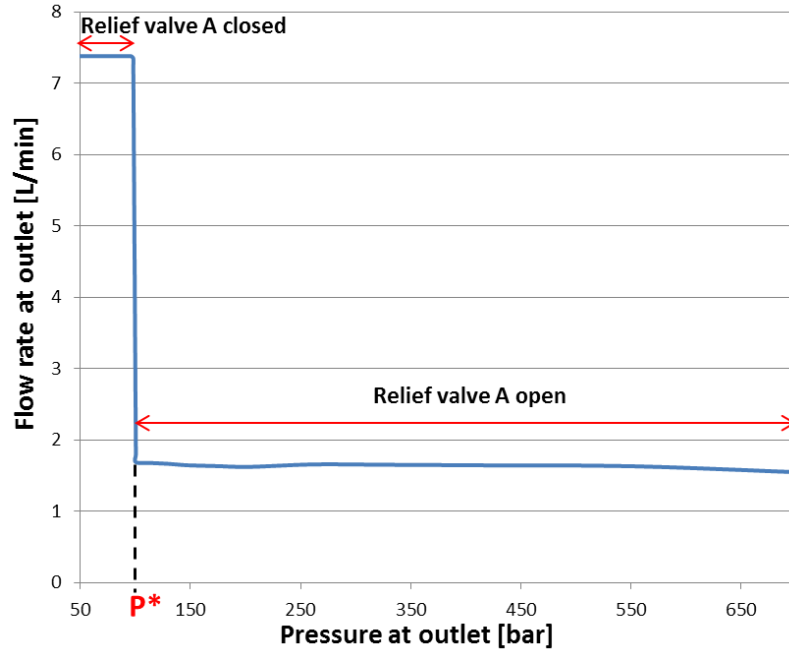


Figure 24: Flow rate at system outlet vs pressure at system outlet.

In order to validate the performance of the hydraulic system, an experimental setup was designed as shown in Figure 25 and flow parameters were measured for an operating cycle of the hydraulic tool. The cycle was run in two steps. Initially, the load (from the hydraulic tool) was kept very low as the hyd. cylinder was reaching the working condition. In the second stage of the cycle, the load at the pump outlet is increased rapidly which occurs when the force requirement by the hydraulic tool is high.

Figure 26 shows a comparison between the experimental and simulated values of fluid pressure in the region between the LP and HP pump (node E in Figure 22). It can be seen through Figure 26 that during the initial half of the cycle the pressure between HP and LP pump remains at a moderate value of 40-50 bar when there is little load acting on the HP pump (radial piston pump). As soon as the load at the outlet is increased, the check valve releases the fluid in the region and the pressure drops down to a minimal pressure of 10-15 bar. There is a small difference in the latter part of the graph between the measured and simulated values as the exact spring setting of check valve was difficult to simulate.

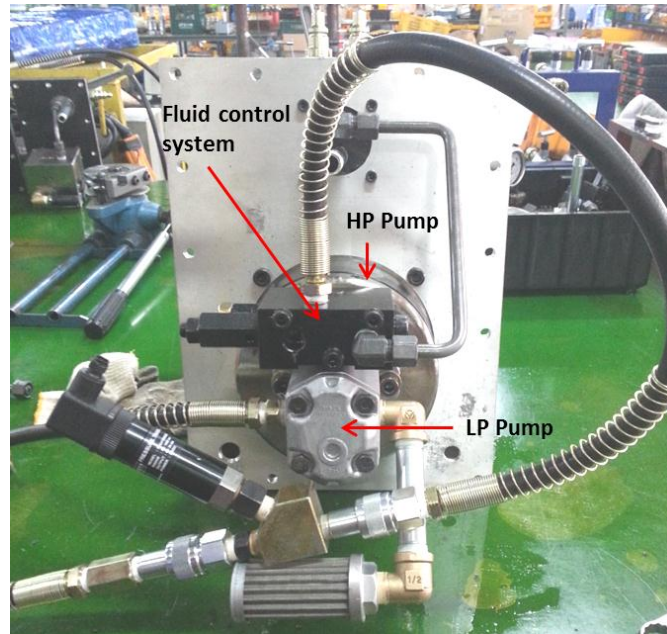


Figure 25: Experimental setup for pressure measurements in LP flow control system parts.

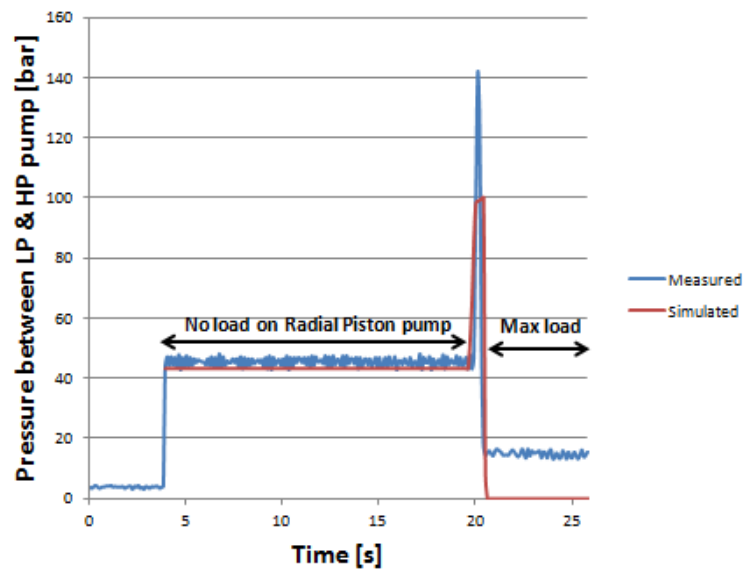


Figure 26: Validation of pressure generation between the HP and LP pump.

A detailed analysis of the hydraulic system was essential to understand its effects on the results of the main pump under study. The results shown in this section led to the conclusion that subsequent investigation of the radial piston pump particularly the lubricating interfaces can be performed without coupling the entire model for the hydraulic system since that only varies the input/output conditions of the flow during the

high flow rate, low pressure period. In the remaining analysis in this study, the steady state results at high pressure from the hydraulic tool system (15 bar constant pressure at radial piston pump inlet) were taken as boundary conditions to run the global fluid dynamic model. Nevertheless, this analysis illustrated a methodology to model generic hydraulic systems in conjunction with the fluid dynamic model for radial piston machines thereby proving the versatility of the multi-domain simulation tool.

CHAPTER 4. PISTON-CYLINDER INTERFACE

In CHAPTER 3, it was mentioned that the global fluid dynamic model predicts leakage flow by assuming a constant gap height between the piston and cylinder by using a simplified laminar flow equation. However, that results in over-estimation of leakage flows leading to inaccurate calculations of the volumetric efficiency of the pump. Also, to analyze the power losses occurring in the gap domain due to viscous friction, it is essential to analyze the gap domain in detail by developing a CFD based model that can generate the steady state values of pressure distribution and film thickness.

This section details the numerical approach used to simulate the lubricating gap flow between piston and cylinder. Although the results presented in this section will pertain to the reference pump chosen in the study, the model developed in this study can be applied to generic radial piston units with both rotating cam and rotating cylinder type designs.

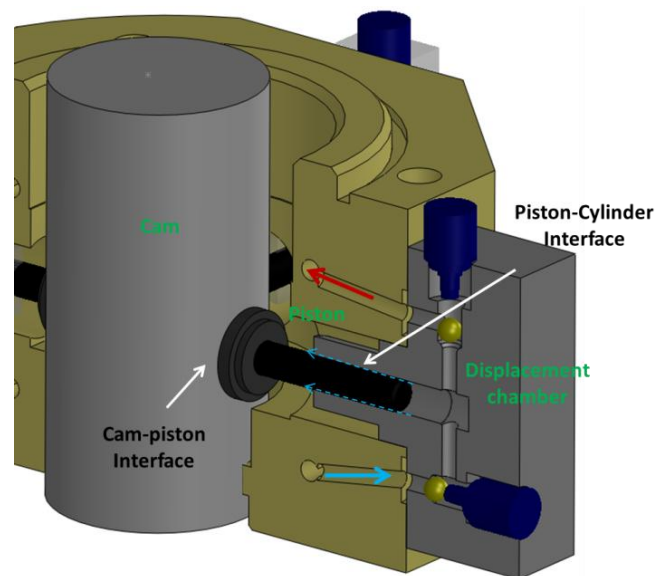


Figure 27: Lubricating gaps in a rotating cam type radial piston pump.

Figure 27 shows the gap domain between the piston and cylinder. The precise evaluation of fluid flow parameters in the gap requires an accurate estimation of the micro-motion of the piston during its reciprocating cycle and evaluation of the gap film thickness at every instant which is critical in calculating the pressure distribution in the gap domain.

To analyze the principle of piston micro-motion, it is important to consider the different forces acting on the piston. In radial piston machines of rotating cam type design, the torque is generated by the eccentric shaft which is transferred to the reciprocating piston as a sum of a linear force component that acts along the piston axis and a transverse component that generates side loads on the piston in the radial direction. Thus, the fluid film needs to generate an appropriate load carrying ability while sealing the displacement chamber simultaneously. It was seen in Figure 21 that the displacement chamber pressure varies greatly during each cycle of pump operation which leads to oscillating loads on the piston. In an efficient pump design, piston self-adjusts its eccentricity to generate adequate hydrodynamic pressure buildup to bear this main external load.

Due to the squeeze film and micro-motion, local high pressure peaks are developed in the fluid film causing elastic deformation of the piston and the cylinder due to pressure loading of surfaces. The surface elastic deformation of piston and cylinder generates an elasto-hydrodynamic lubrication regime and introduces a fluid-structure interaction problem. The different modules/components of the Fluid-Structure Interaction (FSI) solver for piston-cylinder interface are described as follows,

4.1 Fluid Solver

The power losses and leakage flow in the piston-cylinder interface are highly dependent on the pressure generated in the gap domain and the values of gap film thickness. To evaluate the pressure generation based on piston micro-motion, a comprehensive fluid solver was developed that takes into account the hydrodynamic pressure buildup due to the translational effects from piston sliding and squeeze effects due to piston micro-motion. Figure 28 shows the magnified view of the lubricating gap interface between the

piston and cylinder. The various aspects of the fluid solver are detailed in the following sections,

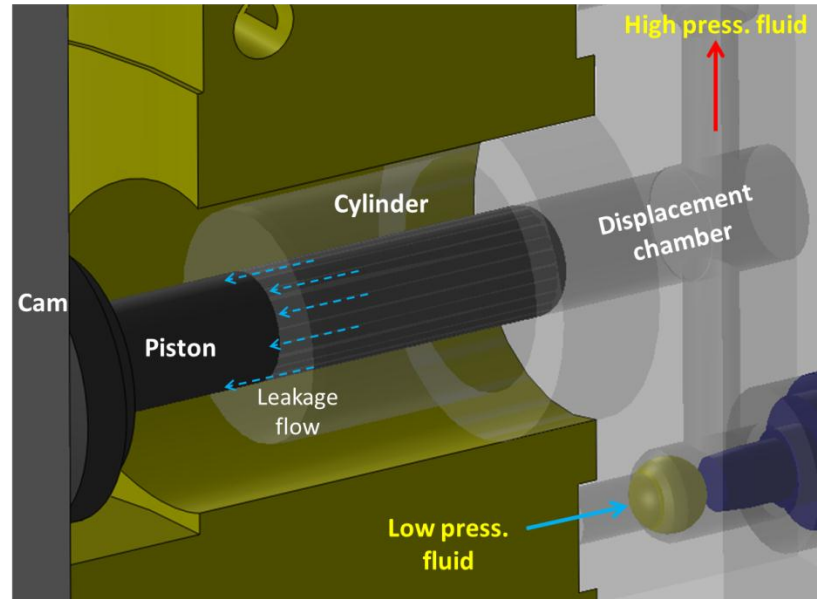


Figure 28: Magnified view of the piston-cylinder lubricating gap showing leakage flow.

4.1.1 Fluid Film Geometry

Figure 29 shows the fluid film geometry as it exists in the reference pump design. The lubricant film region consists of the annular region between two cylindrical surfaces of piston and cylinder with the length of the film region dependent on instantaneous piston position. The thickness of the lubricating film needs to be calculated throughout the gap domain as an input to the fluid solver for solving for pressure distribution. This is achieved by formulating geometrical relations for piston-cylinder geometry using the coordinate system as depicted in the figure.

Since all the forces acting on the piston (discussed in detail in 4.4) in the present pump geometry are in the x-y plane with no force component on the piston along z axis, 2 degrees of freedom (e_1, e_2) are sufficient to describe the piston in any arbitrary configuration in its radial micro-motion.

The co-ordinates of the center of piston cross section along the length of the gap can be defined as,

$$y_m(x) = \frac{e_2 - e_1}{l_{gap}}(x - x_A) + e_1 \quad (4.1)$$

where e_1 , e_2 are the piston eccentricities at either end of the lubricating gap as shown in the figure, x_A is the distance of cylinder face from origin which remains fixed and l_{gap} is the instantaneous length of the lubricating film region.

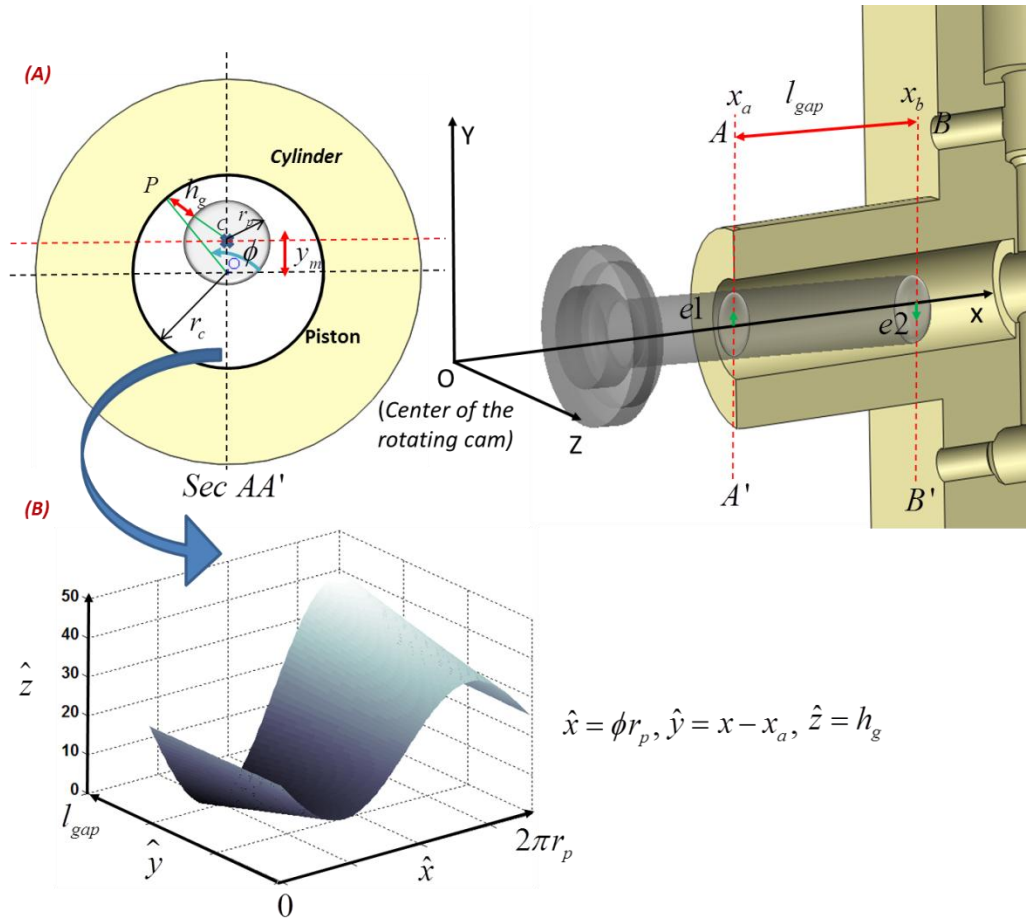


Figure 29: (A) Evaluation of film thickness in the lubricating gap domain. (B) Fluid film in unwrapped configuration.

Using geometry as shown in Figure 29, the film thickness value at h_g any arbitrary point in fluid domain can be expressed as a function of the circumferential angle ϕ and distance along the piston axis x as follows,

$$h_g(x, \phi) = \sqrt{(r_c \sin \phi - y_m(x))^2 + r_c^2 \cos^2 \phi} - r_p \quad (4.2)$$

The evaluation of gap height using Equation (4.2) considers piston and cylinder as rigid bodies. The change in gap heights due to elastic deformation of surfaces will be discussed in detail in the next section.

The fluid film is present in a circular configuration in the actual pump design. However, the curvature of the film geometry can be neglected while solving for pressure generation, since the piston-cylinder clearance is much smaller to the piston diameter. It implies that now the film shape can be unwrapped from the piston circumference and viewed as a periodic stationary profile with length $2\pi r_p$. This reduces the complicated film geometry into a simplified one that can be easily represented in the cartesian frame as shown in Figure 29 using the transformed co-ordinates \hat{x}, \hat{y} for circumference and gap length respectively.

4.1.2 Mesh Setup & Boundary Conditions

The complexity of piston-cylinder geometry along with the non-linear behavior of the governing equations makes it infeasible to obtain an analytical solution for pressure generation in the fluid domain. From the unwrapped configuration of fluid film as discussed in the previous section, it can be seen that the computational domain is now a rectangular cartesian grid with gap height varying with both \hat{x}, \hat{y} coordinates. By principles of fluid mechanics, this would call for constructing a 3-D grid in fluid domain with \hat{z} axis representative of the gap height of the fluid element. However in practice, the lubricating gap domains are characterized by extremely small value of film thickness which is typically in the order of a few microns. At such miniature thickness values, the variation of fluid pressure in the \hat{z} direction can be safely neglected and pressure is considered a function of \hat{x}, \hat{y} only. This assumption is one of the key principles of lubrication theory that was developed by Reynolds in his classic paper [47]. Hence, the problem of solving for pressure distribution in fluid domain is reduced to a two dimensional problem \hat{x}, \hat{y} coordinates.

The simplified computational grid for the problem can be seen in Figure 30. An automatic mesh generator was developed to take into account the changing gap lengths for each time instant (angular position of the rotating shaft).

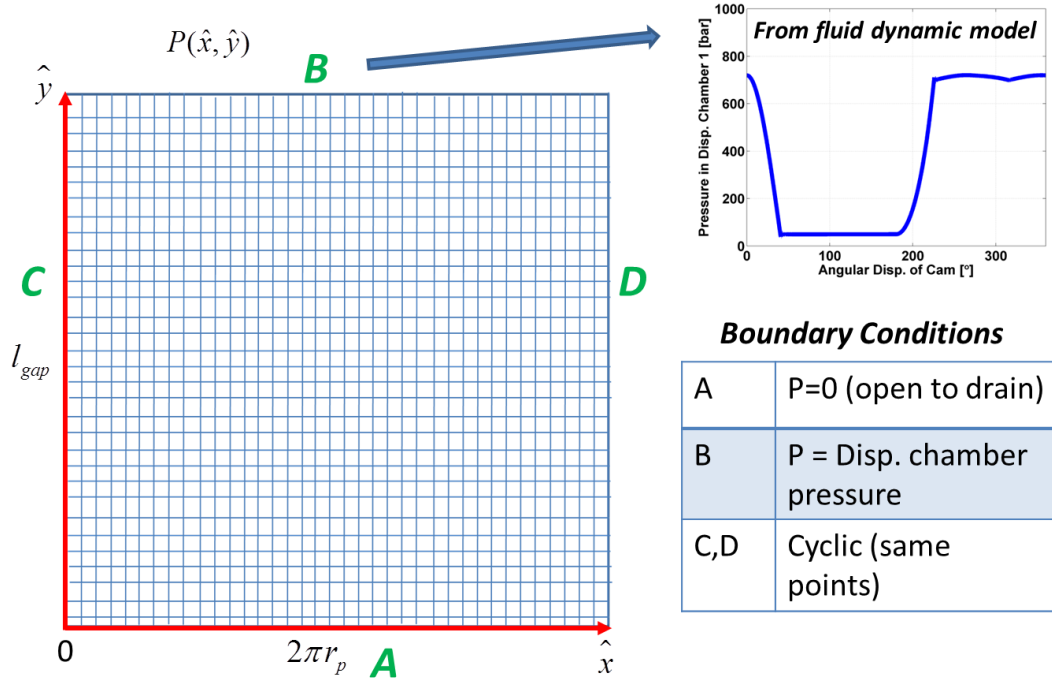


Figure 30: Computational grid for fluid domain with boundary conditions.

Figure 30 also shows the boundary conditions used for obtaining the numerical solution. It can be seen that the mesh boundary in contact with the displacement chamber has been assigned a constant pressure which is equal to the instantaneous displacement chamber pressure. This pressure is calculated through the fluid dynamic model as already explained in CHAPTER 3. The lower boundary of the mesh is set to constant ambient pressure (0 bar) since it is exposed to the drain. The boundaries on the left and right are defined as cyclic boundaries since they represent the same set of points in the actual wrapped configuration.

4.1.3 Solution Process

The fluid pressure generation in the lubricating gap domain is calculated using the Reynolds equation which forms the basis of modeling lubricant flow in common

tribological interfaces. The Reynolds equation is derived from the Navier-Stokes equation following specific assumptions for lubricating domain,

- The inertial force of the fluid is negligible compared to the viscous forces.
- The pressure variation along the gap height (z-direction) is neglected since the gap thickness is of the order of microns. Hence, $p = p(\hat{x}, \hat{y})$
- The velocity component normal to the gap plane can be neglected.
- The gradient of fluid velocity in the gap plane is negligible compared to the gradient along the gap thickness i.e. $\frac{\partial V}{\partial z} \gg \frac{\partial V}{\partial \hat{x}}$ and $\frac{\partial V}{\partial z} \gg \frac{\partial V}{\partial \hat{y}}$

These assumptions allow for the derivation of the well-known Reynolds equation [48]. However, this commonly used form of this equation has the capability to model surface features on only one boundary with the other required to be flat. This is insufficient for the model developed in this study since the deformation of both piston and cylinder surfaces are considered. Hence, an appropriate form of Reynolds equation for piston-cylinder interface of radial piston pump was developed as follows,

$$\nabla \cdot \left(\frac{\rho h^3}{12\eta} \nabla p \right) - \left(\frac{\rho V_b}{2} \right) \cdot \nabla h - \rho V_b \cdot \nabla h_b - \rho \frac{\partial h}{\partial t} = 0 \quad (4.3)$$

where $h = h_t - h_b$ as shown in Figure 31. The detailed derivation of Equation (4.3) is presented in APPENDIX B.

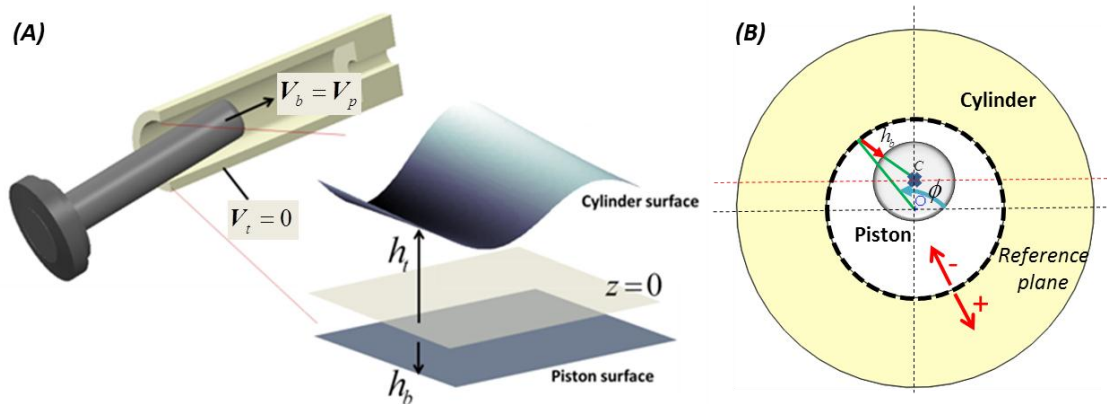


Figure 31: (A) Terms in Equation (4.2) : top surface (h_t); bottom surface (h_b); fixed cylinder (V_t); piston velocity (V_b). (B) Reference plane and sign convention.

The elastic deformation of both piston and cylinder surfaces is now taken into account. For calculating the gap height terms (h_t, h_b), the original un-deformed cylinder surface is taken as the reference plane. All values in the radially outward direction (towards cylinder surface) are taken as positive while the distances towards the piston surface are treated with negative sign. Under such considerations, the cylinder surface height (h_t) becomes equivalent to the deformation in cylinder surface (Δh_t),

$$h_t = \Delta h_t \quad (4.4)$$

while h_b can be written as,

$$h_b = -h_g + \Delta h_b \quad (4.5)$$

It can be seen from Figure 31 that the velocity of the top surface $V_t = 0$ since the cylinder is stationary while the velocity of the lower surface is equal to the translational velocity of the piston $V = V_p$. Since the piston is free to move in the radial direction during the reciprocating cycle, the squeeze velocity is modeled using the $\frac{\partial h}{\partial t}$ term in Equation (4.2).

It can be seen through the previous studies on lubricating gaps [49] that thermal effects are less pronounced in piston cylinder interface of positive displacement machines compared to the impact of elastic deformation on overall results. Since much higher operating conditions are considered in this study, the inclusion of elastic deformation is given more importance and the analysis is simplified by assuming isothermal conditions throughout the study. Incorporating the effects of heat generation and thermal deformation can be a part of future improvements of the FSI model.

The dependence of the fluid properties involved in Equation (4.3) (density and viscosity) are modeled using the relations found in [50],

$$\rho = \rho_0(1 + \beta_p(p - p_0)) \quad (4.6)$$

$$\eta = \eta_0 e^{\alpha_p p} \quad (4.7)$$

To solve the Reynolds equation, a Finite Volume Method (FVM) solver was implemented in C++ using the open source OpenFOAM libraries. The pressure is solved using the Preconditioned Conjugate-Gradient algorithm, with a Diagonalized Incomplete Cholesky preconditioner [51].

4.1.4 Evaluation of Performance Parameters

4.1.4.1 Leakage flow

The FSI solution algorithm calculates the lubricant film thickness and the pressure field in the gap. The pressure field can be used for finding the fluid velocity (\hat{x} and \hat{y} components) as follows:

$$u = \frac{1}{2\eta} \frac{\partial p}{\partial \hat{x}} [z^2 - z(h_t + h_b) + h_t h_b] - \frac{zu_b}{h_t - h_b} + \frac{h_t u_b}{h_t - h_b} \quad (4.8)$$

$$v = \frac{1}{2\eta} \frac{\partial p}{\partial \hat{y}} [z^2 - z(h_t + h_b) + h_t h_b] - \frac{zv_b}{h_t - h_b} + \frac{v_b}{h_t - h_b} \quad (4.9)$$

Since, the drain interface of the lubricating gap is at low pressure, there is a net leakage in fluid flow through the gap from the high pressure region (displacement chamber) as shown in Figure 28. Using the velocity field of the fluid, the leakage flow rate from the gap can be calculated by integrating it along the area of the film at drain interface:

$$Q_{leak} = \sum_i \int_0^{2\pi r_p h_t} \int_{h_b} \mathbf{v}_i \cdot \mathbf{n}_i dA \quad (4.10)$$

4.1.4.2 Power losses due to viscous friction

The relative motion between the piston surface and the fluid film in the lubricating gap generates viscous friction on the piston. These forces contribute to the power losses occurring in the gap domain. To calculate the resultant power loss due to fluid friction, shear stress acting on the piston surface is evaluated for each cell and summed across the piston surface:

$$P_{visc} = \int_0^{l_{gap}} \int_0^{2\pi r_p} \tau_{zy} u_b d\hat{x} d\hat{y}; (\tau_{zy})_{z=h_b} = \eta \left(\frac{du}{dz} \right)_{z=h_b} \quad (4.11)$$

4.2 Solid Deformation Solver

Since the fluid pressures generated in the gap domain are high, the elastic deformation of the piston-cylinder cannot be neglected, since a small change in gap height produces a significant change in the flow parameters. In this study, the solid deformation is modeled using a steady state FV stress/deformation solver developed in [52] which has been utilized for FSI modeling of gear pumps in the past [20,22],

$$\frac{\partial^2(\rho\mathbf{u})}{\partial t^2} - \nabla[2\vartheta + \lambda]\nabla\mathbf{u} - \nabla[\vartheta(\nabla\mathbf{u})^T + \lambda\text{Itr}(\nabla\mathbf{u}) - [(\vartheta + \lambda)\nabla\mathbf{u}] = \rho\mathbf{f} \quad (4.12)$$

The above equation is derived from the base governing equation used for modeling structural problems which is shown below,

$$\nabla \cdot \boldsymbol{\sigma} + \rho\mathbf{f} = 0 \quad (4.13)$$

This is coupled with a linearized definition of the strain and a linear elastic model using Hooke's law for stress and strain tensors,

$$\boldsymbol{\epsilon} = \frac{1}{2} [\nabla\mathbf{u} + (\nabla\mathbf{u})^T] \quad (4.14)$$

$$\boldsymbol{\sigma} = 2\xi\boldsymbol{\epsilon} + \lambda\text{tr}(\boldsymbol{\epsilon})\mathbf{Id} \quad (4.15)$$

where ξ and λ are Lamé's coefficients and defined as follows,

$$\xi = \frac{E}{2(1 + \nu)} \quad (4.16)$$

$$\lambda = \frac{\nu E}{(1 + \nu)(1 - 2\nu)} \quad (4.17)$$

The implicit and explicit grouping of the spatial derivative terms in Equation (4.12) promotes the stability of this algorithm with convergence speeds comparable to commercial FEM software. To solve for deformation \mathbf{u} in Equation (4.12), a 3-D FVM solver was developed in C++ using OpenFOAM libraries. The linear system is solved

using an implementation of Generalized Geometric-Algebraic Multi-Grid (GAMG) algorithm.

The first step in case setup for the solid solver is to discretize the solid domain for piston and cylinder by generating a computational grid. Figure 32 shows a sample mesh for piston and cylinder geometries for the reference pump design. The mesh is unstructured and made of tetrahedral elements so that it can conform close to the actual geometry of solid components.

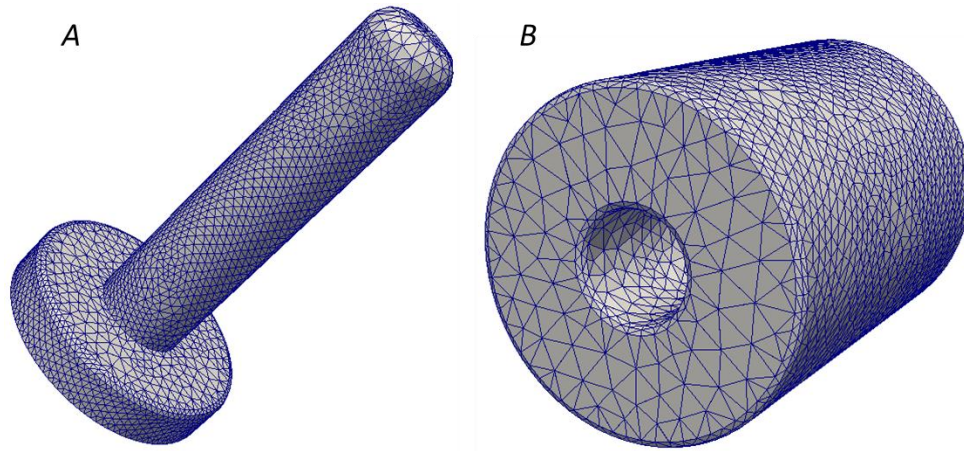


Figure 32: Solid mesh for piston and cylinder geometries.

4.2.1 Influence Method for Evaluating Material Deformation

The deformation of the piston and cylinder is evaluated by using an offline technique based on the influence operator. This technique is based on the assumption of linear elasticity of solid parts and has been used extensively in studying the elastic deformation in axial piston machines [49, 53], gear machines [20, 22] and for EHL studies [54-56]. In this approach, separate matrices E are generated for piston and cylinder which store the corresponding deformation for reference pressure loads applied to each individual boundary cell. Once the influence matrices (IM) are evaluated, the deformation of solid boundaries for actual pressure loads can be calculated using,

$$\delta h_i = \sum_j E_{ij} \frac{p_j}{p_{ref}} \quad (4.18)$$

where $i, j = 1, 2, \dots, N$ are the number of boundary faces on the gap interface of piston/cylinder and p_j is the pressure loading on these cells. The influence coefficient E_{ij} represents the deformation on the i^{th} face due to a reference pressure load acting on j^{th} face.

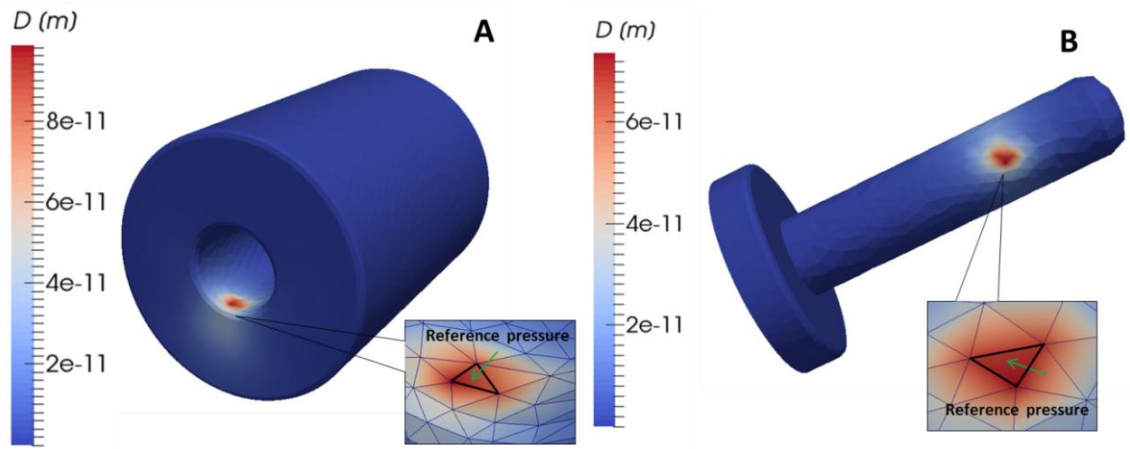


Figure 33: Deformation fields in cylinder (A) and piston (B) on application on reference pressure on a single cell. Ideal support constraint used for both geometries.

4.2.2 Ideal Support Constraint

The evaluation of elastic deformation in solid parts requires specific boundary conditions to start the computational process. These boundary conditions in case of solids pertain to the constraint conditions imposed on the solid which are critical in the process of calculating the deformation field and final results. Previous studies on FSI of lubricating interfaces in positive displacement machines (axial piston, gear machines) have seen the use of different constraint conditions on solid parts namely ideal support, fixed support and inertia relief methods [20,57]. The fixed support method constrains the movement of solid body along a fixed face/region while evaluating the deformation due to pressure forces. This constraint condition yields accurate results only if the constrained face/region does not move in the actual machine. The inertia relief method is best suited for freely floating bodies in which the solid part is assumed to be in equilibrium by application of an equal and opposite distributed force throughout the domain that cancels the effect of inertial forces.

For the present study, the ideal support constraint conditions are used wherein the axis of both piston and cylinder were constrained (refer Figure 34) to prevent the bending of the solid parts. This assumption permits to consider effects due to micro-surface deformation while preventing deflection or macro-deformation of the structure and has been found to agree well with experimental observations [58-60]. The inertia relief method is not well suited for current analysis since the piston experience high contact forces (at least during the delivery stroke) for the reference cases. The resulting displacement field is representative of the surface deformation which is important to analyze to account for pressure generation in the lubricating gap. The deformation of solid boundaries is then used to modify the film thickness values as detailed in Equations (4.4) and (4.5). A strong coupling between the fluid and solid solvers ensures that the pressure field changes significantly with a small deformation field in solid boundaries and thus opposes the large scale deformation in solid parts. Hence, neglecting the macro scale bending and deformation in piston, cylinder geometries present a valid assumption which is necessary to facilitate the FSI analysis. Also, the other constraint conditions are not applicable to the parts of the reference pump design since the piston, cylinder are not free floating bodies and are not constrained by a single fixed surface.

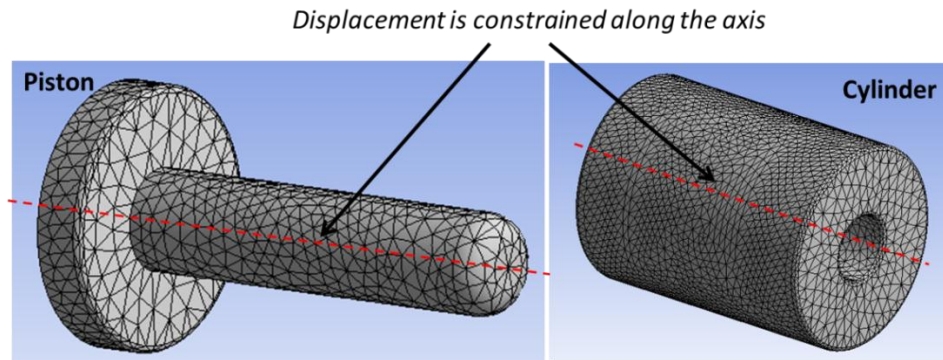


Figure 34: Ideal support constraint for piston & cylinder geometries.

4.3 Dynamic Linking of Fluid & Solid Meshes

The elastic deformation in solid surfaces changes the pressure field in the gap and vice-versa. Hence, it is necessary to link the solid and fluid meshes together to formulate a FSI model for the gap. Since, the fluid mesh for the gap was unwrapped to a Cartesian frame before solving for pressure, the boundary faces on the gap interface of piston and cylinder solid meshes also need to be unwrapped to a 2D co-ordinate system before the dynamic link can be established. The fluid mesh is made finer than the solid meshes for numerical considerations. The nearest-neighbor searching algorithm links each solid face to a group of fluid cells. The fluid pressure was transferred to the coarser solid mesh by full-weighting whereas injection was used to transfer the deformation values back to the fluid mesh. Figure 35 shows the dynamic link between the fluid and the piston solid mesh. A similar procedure is adopted for linking the cylinder mesh to fluid cells.

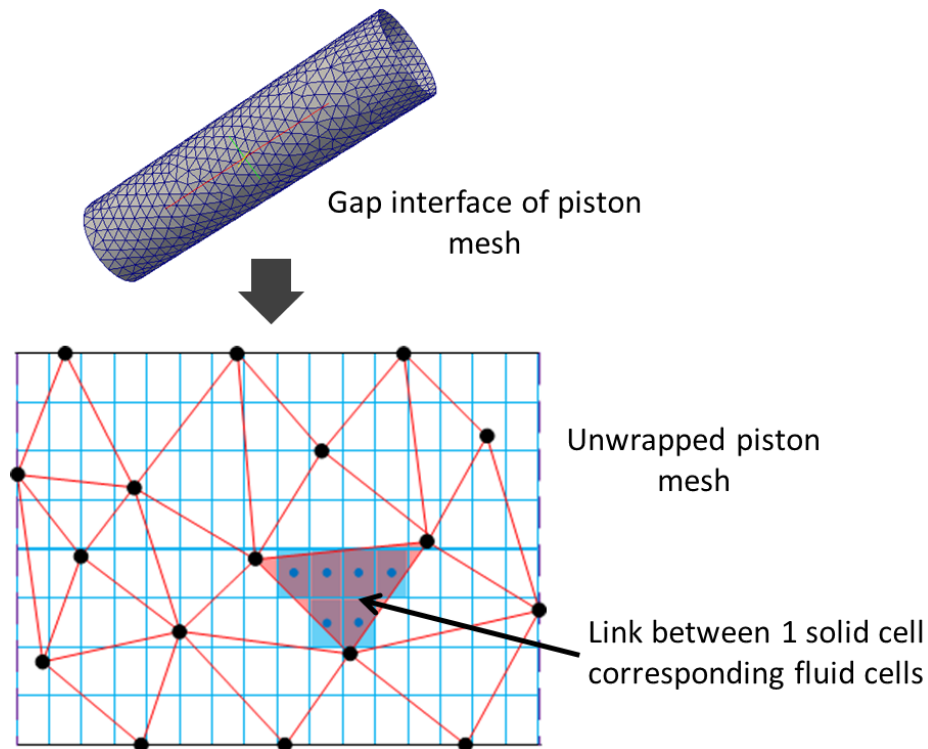


Figure 35: Dynamic link between fluid & solid mesh. Fluid mesh elements are shown in blue while red lines represent solid mesh faces.

4.4 Force Analysis of Piston

A quasi-static analysis of piston motion is assumed throughout the study wherein the piston must satisfy the equilibrium condition at every instantaneous position in the cycle. Essentially, a balance of forces acting on the piston must be performed to achieve prediction of the lubricating gap film thickness, since the forces arising from the lubricating film will have to balance out all the external forces acting on the piston in a steady state operation of a radial piston machine. This quasi-steady approach has been successfully applied and experimentally validated for other positive displacement machines [19, 61].

Figure 37 shows the different forces acting on the piston body during an operational cycle. The reaction forces exerted by the rotating cam on the pistons act along the x-y plane only since there are no forces acting on the driving shaft/cam axis (z direction) which is a typical feature of radial piston machines.

Table 2: Nomenclature for forces as shown in Figure 37.

<i>Symbol</i>	<i>Description</i>
F_{spring}	Force exerted by the spring.
F_{DK}	Force exerted by the disp. chamber pressure (P_{DC})
F_{CN}	Reaction force from the cam
F_{aK}	Inertial force acting on the piston
F_{Tf}	Viscous friction from fluid in the lubricating gap
F_{Cf}	Friction force from the cam
F_{TN}	Normal force exerted by fluid film in piston-cylinder interface

The high pressure in displacement chambers in the delivery stroke keeps the pistons tightly pressed against the rotating shaft. When the pressures are low, the springs connecting the piston head to the cylinder block (not shown in the figure) solve the same purpose. The spring force F_{spring} and the inertial force F_{aK} can be calculated using the piston kinematics that can be evaluated through the geometric model. The pressure force

from the displacement chamber F_{DK} is calculated using displacement chamber pressure P_{DC} obtained through the fluid dynamic model. The inertial forces acting on the piston were found to be small in comparison to the pressure forces and hence neglected in this analysis. From the geometry shown, it can be seen that both F_{spring} and F_{DK} act along the piston axis. By balancing the forces on the piston along the x direction, the reaction force from the cam F_{CN} can be obtained.

A critical factor which affects the side loads acting on the piston is the friction force exerted by the cam on the piston F_{Cf} . In the initial part of the study, this friction force F_{Cf} is calculated by assuming a constant value of friction coefficient $\mu = 0.1$ that is representative of a metal to metal sliding contact condition. Results from the FSI model based on this assumption are described in this chapter. An accurate evaluation of F_{Cf} using numerical methods presents a challenging problem in which the dynamics of the surfaces involved and the instantaneous loads have to be considered in detail along with an analysis of changing lubrication regimes in the interface. This problem has been addressed in a greater detail in CHAPTER 5 where a comprehensive EHL friction model has been developed that can generate instantaneous values of coefficient of friction μ that varies greatly within an operating cycle.

Due to absence of forces acting along the z direction as explained above, the piston micro-motion is considered only within a single plane with two degrees of freedom (e_1, e_2) sufficient to describe the instantaneous eccentric position of the piston.

To simplify the calculation process, all external forces and moments acting on the piston are resolved into an equivalent set of two forces $F_{e1} F_{e2}$ acting on either end of the lubricating gap as shown in Figure 37. This is achieved through the following steps,

Balancing the forces in x direction on the piston,

$$F_{CN} + F_{e2} + F_{spring} + F_{aK} + F_{DK} = 0 \quad (4.19)$$

Equating the set of forces $F_{e1} F_{e2}$ to the external force acting in y direction,

$$F_{e1} + F_{e2} + F_{Cf} = 0 \quad (4.20)$$

Performing moment balance about the point A (shown in Figure 37),

$$F_{e2} \cdot l_{gap} - [F_{CN} \cdot y_{cp} + F_{Cf} \cdot (x_A - x_{cp})] = 0 \quad (4.21)$$

where x_{cp}, y_{cp} are the coordinates of the contact point between cam and the piston.

The values of F_{e1} F_{e2} can be obtained by solving the Equations (4.19) - (4.21). In order for the piston to remain in static equilibrium, the external forces acting on the piston have to be balanced by the fluid pressure generated in the gap domain. However, if the resulting hydrodynamic forces are too small, the lubricating film is not able to support the external loads and there is solid-solid contact resulting in large forces acting on the piston and cylinder bodies. These contact forces lead to elastic deformation of solid parts wherein the loads are supported partly by the fluid film and partly by the asperity contact between the surfaces. A detailed analysis of such a condition requires developing a model for mixed lubrication between surfaces which is not considered in this study. For most cases, there is little or no solid contact and the contact forces need to be calculated only to ensure stability of the computational procedure. For this purpose, a minimum gap height (h_{min}) of $0.2 \mu m$ is assumed while solving for pressure distribution. Once the gap height at each grid point (h) is calculated using Equations (4.4) and (4.5), the strain due to elastic deformation caused by solid contact is defined as,

$$\epsilon_{el} = \begin{cases} 0 & \text{when } h > h_{min} \\ \frac{h_{min} - h}{2r_p} & \text{when } h < h_{min} \end{cases} \quad (4.22)$$

When gap heights go below h_{min} , a virtual contact pressure (p_c) is applied to simulate the effect of a possible solid contact between the piston and cylinder surface. The contact pressure is calculated by assuming the h_{el} as the strain produced in the piston,

$$p_c = \epsilon_{el} E_p \quad (4.23)$$

This approach has been successfully applied in studying the piston-cylinder interface of axial piston machines [61]. The resultant fluid force acting on the piston surface is now calculated by adding the hydrodynamic force and the contact pressure force. A similar process is adopted for resolving the net effect of the fluid forces into two forces F_{s1} F_{s2}

(as shown in Figure 36) by equating forces acting in y direction and balancing the moment about point A,

$$F_{s1} + F_{s2} = \iint_{x_A 0}^{x_A+l_{gap} 2\pi r_p} -(p + p_c)\sin\phi dx dy ; y = r_p \sin\phi \quad (4.24)$$

$$F_{s2} \cdot l_{gap} - \iint_{x_A 0}^{x_A+l_{gap} 2\pi r_p} -(p + p_c)x \sin\phi dx dy - \iint r_p \sin\phi dF_{visc} = 0 \quad (4.25)$$

where dF_{visc} represents the viscous force acting on the boundary element of piston which can be evaluated using Equation (4.11).

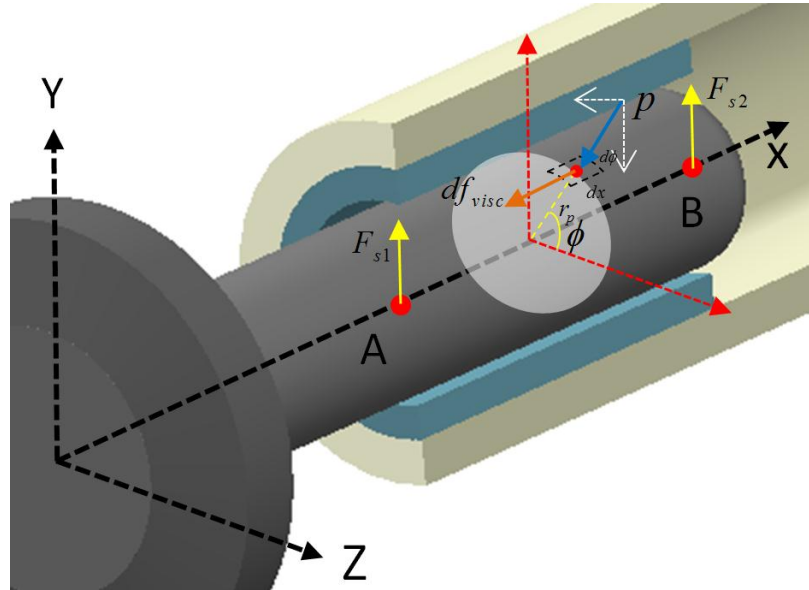


Figure 36: Detailed view of fluid forces acting on the piston for resolution of F_{s1}, F_{s2} .

Once the external and fluid forces have been resolved separately as shown, the equation of force balance of piston in y direction can be written as,

$$F_{e1} + F_{e2} + F_{s1} + F_{s2} = 0 \quad (4.26)$$

where the inertial forces are not considered in the y direction owing to quasi-steady assumption for piston micro-motion.

Equation (4.26) is used for checking the force-balance condition once the pressure field in the gap domain has been computed. The solution algorithm for the computational procedure is explained in detail in the next section.

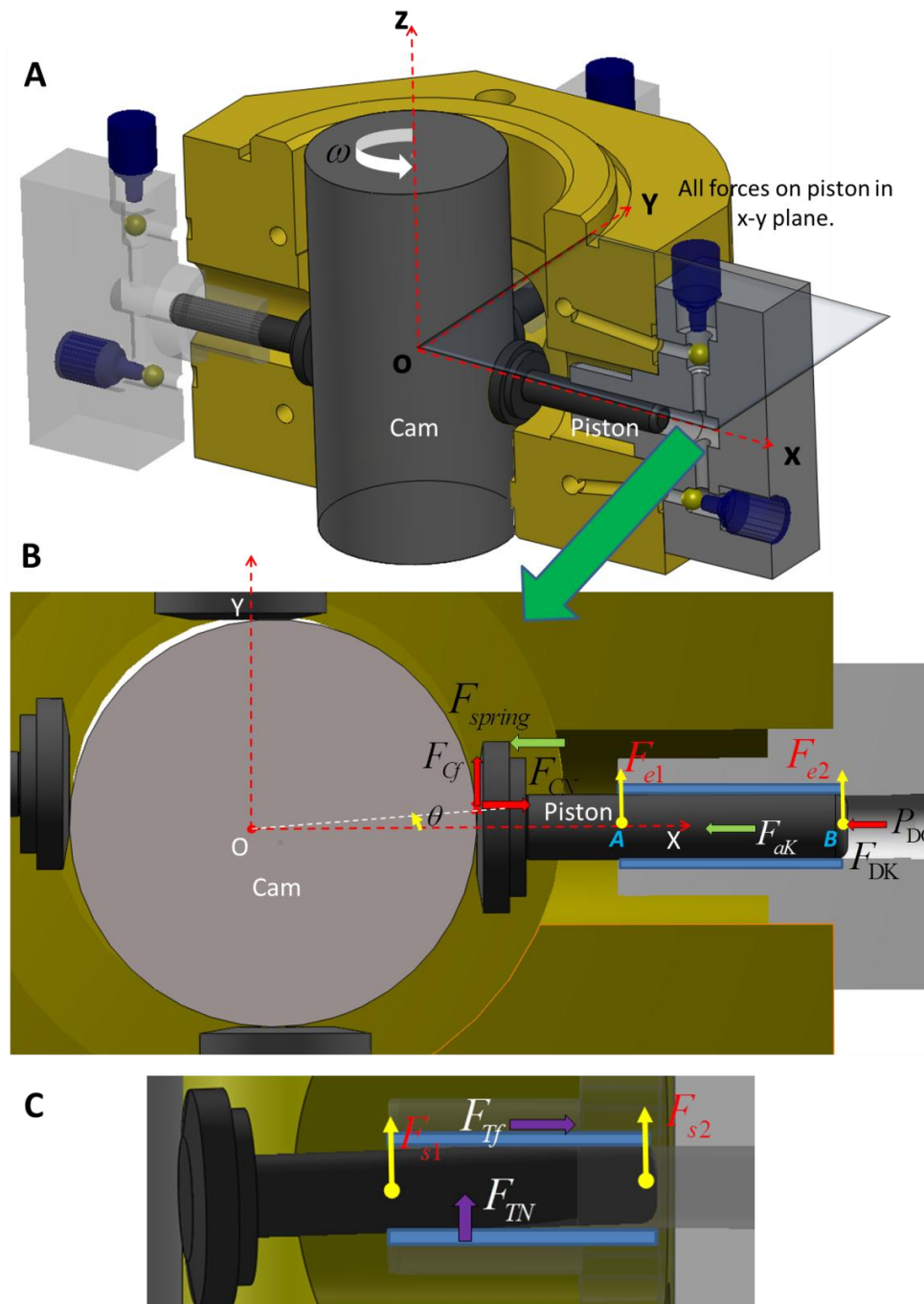


Figure 37: (A) 3D view of the piston and interacting components. (B) Free body diagram of the reciprocating piston. (C) Resolution of fluid forces.

4.5 FSI Solution Algorithm

The complete scheme for the FSI algorithm is shown in Figure 38. The numerical procedure consists of three main iterative loops:-

- Solution of fluid flow in the lubricating gap.
- Solution of deformation of piston and cylinder.
- Solution of piston micro motion by considering force balance of the piston at each time step.

The simulation process starts by estimating an eccentric position of the piston $\mathbf{e}^{(0)}$ for the initial time step. For the calculation of radial micro-motion of the piston, it is necessary to solve the equations of motion by estimating the squeeze velocities of the piston at every time instant. The squeeze velocity of the piston ($\frac{de}{dt}$) is varied through an iterative loop using the Powell's multidimensional root finding method that checks for the force balance of the piston at each successive step until the criteria is met. This forms the main iterative loop for the algorithm. For each value of squeeze velocity in the iterative process, an inner FSI loop is made to run. In this inner loop, the fluid pressure in gap domain is solved using the Reynolds equation and is then used to calculate deformation in the piston and cylinder faces. The new gap film thickness values are used to update the pressure field and these iterations run until both the fluid pressure and solid deformation values reach convergence. Once the squeeze velocity for a time instant is converged, the eccentric position of the piston is calculated for the next instant by numerically integrating the velocity over a time step using the Euler-explicit method,

$$\mathbf{e}^{(n+1)} = \mathbf{e}^{(n)} + \dot{\mathbf{e}}^n (t^{n+1} - t^n) \quad (4.27)$$

The criterion for stopping the calculations is the piston position \mathbf{e} at a shaft angle of $\theta = 0^\circ$ and $\theta = 360^\circ$. For the steady state solution, the calculated positions of the piston at $\theta = 0^\circ$ and $\theta = 360^\circ$ should be same. Therefore, the calculations are done for several revolutions until this convergence is reached.

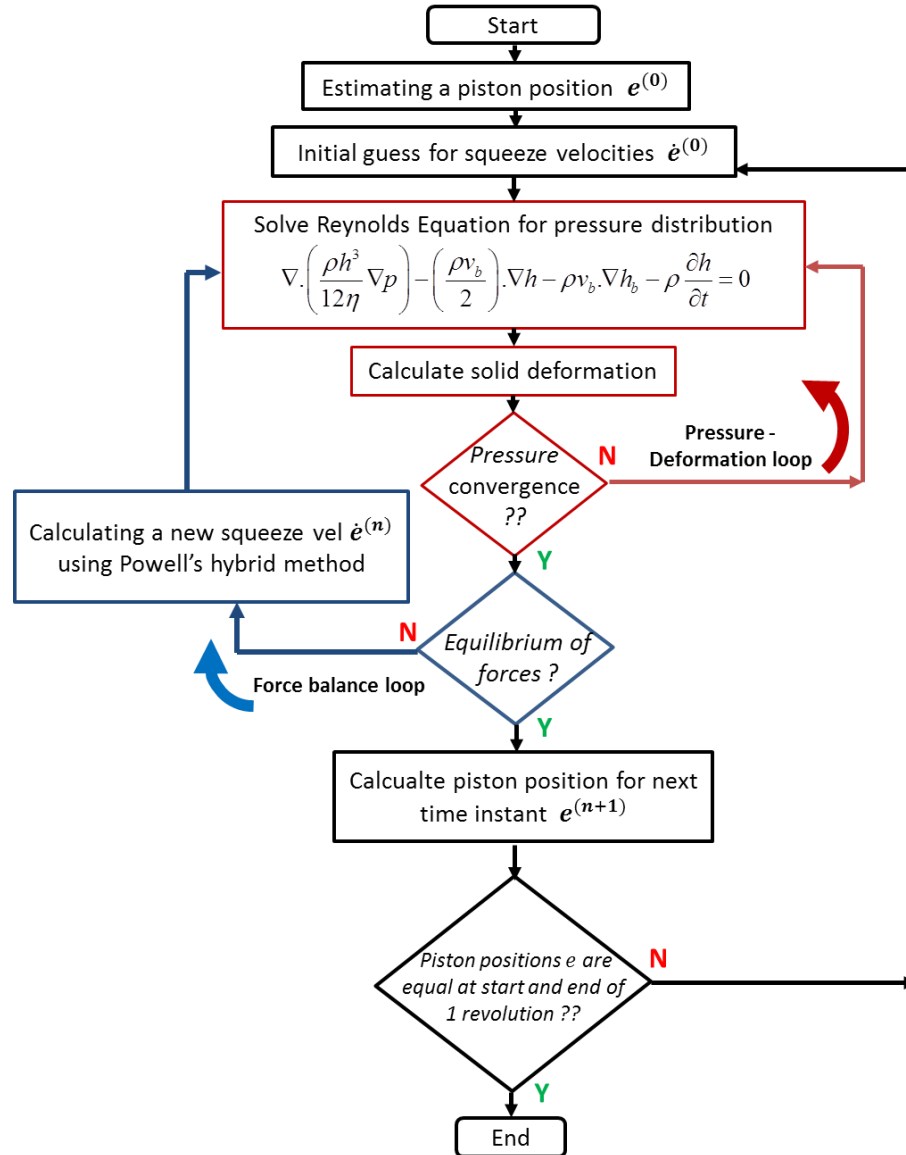


Figure 38: Numerical algorithm for FSI coupled force balance model.

4.6 Results

In this section, the results from the FSI model for piston-cylinder interface are discussed in detail. The FSI model developed in this study is versatile and capable of handling a wide range of operating conditions. All the simulation results depicted in this section correspond to the converged values when the piston eccentricities stop changing with time. Figure 39A shows the typical variation of piston eccentricities (e_1, e_2) with simulation time. As can be seen, the simulation starts with the initial assumption of

eccentricities and after several iterations, the variation of e_1, e_2 during a pump cycle stops varying. Figure 39B shows a closer look at this variation by plotting the change in eccentricities ($\Delta e_1, \Delta e_2$) with number of pump revolutions for which the simulation is run.

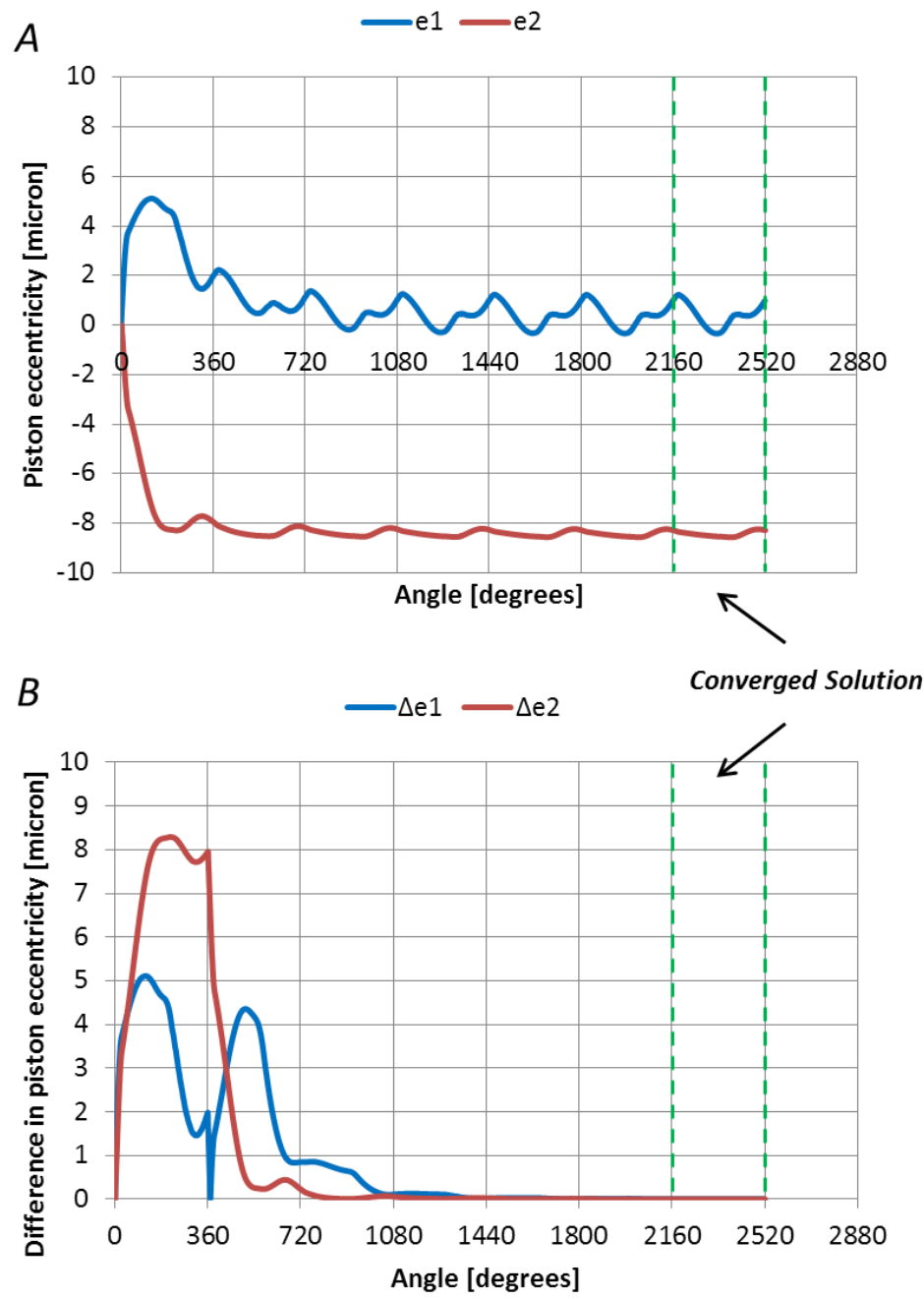


Figure 39: Typical convergence plot from the FSI model.

Details of the reference design, working fluid and information regarding solid components are provided in Table 3.

Table 3: Details of the reference pump, working fluid and solid component parameters used in simulations.

<i>Details of reference pump</i>	
Displacement	1.0 cc/rev
Nominal clearance between piston and cylinder	8 μm
<i>Working fluid</i>	
	ISO VG 32 Hydraulic Oil
Density @15°C	869 kg/m ³
Viscosity @15°C	0.02 Pa-s
<i>Piston & Cylinder</i>	
	Steel
Young's modulus	200 GPa
Poisson's ratio	0.29
Density	7850 kg/m ³

The instantaneous displacement chamber pressures calculated using the global fluid dynamic model for sample operating conditions are shown in Figure 40. These are used as boundary conditions for running FSI simulations the results of which are discussed in detail in the following sections,

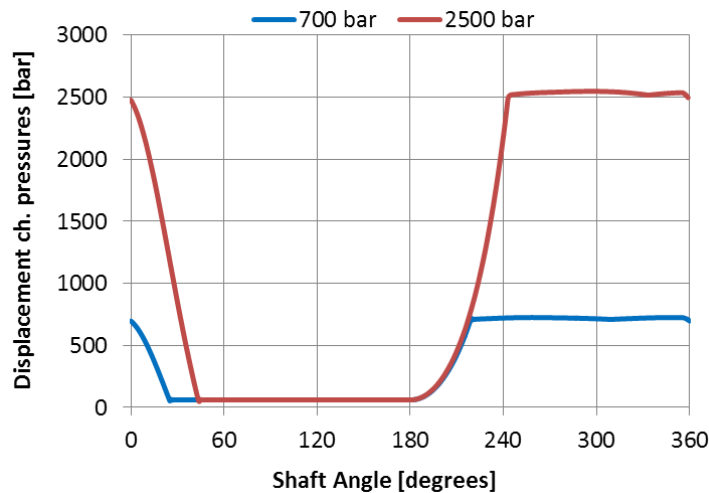


Figure 40: Displacement chamber pressures obtained through global fluid dynamic model for outlet pressures of 700 bar and 2500 bar. Shaft speed=1800 rpm.

4.6.1 Result Comparison between FSI and Rigid Body Model

This section highlights the importance of simulating elastic deformation for piston and cylinder parts while modeling radial piston units. The reference pump is analyzed for pump outlet pressures as high as 700-2500 bar where deformation of solid parts cannot be neglected. To demonstrate the effect of deformation on lubrication performance, a comparison is drawn between the results obtained when piston and cylinder are considered as rigid bodies against the FSI results.

Figure 41 and Figure 42 show the pressure field and film thickness distribution in the lubricating gap domain respectively at different shaft angles in a pump cycle for the rigid model at an operating condition of 2500 bar outlet pressure and 1800 rpm shaft speed. This operating condition is representative of ultra-high operating pressures and the results obtained need to be studied carefully. The figure illustrates the instantaneous pressure fields over every 45° of shaft revolution. The pressure field is shown in unwrapped configuration where ϕ represents the circumferential angle over a cross-section, \hat{y} represents the gap length along the cylinder axis. Throughout this study, the pressure and film thickness plots correspond to the displacement chamber 1 as shown in Figure 41. A shaft angle (θ) of 0° represents the position when the piston 1 is at its bottom dead center and the suction stroke starts. The suction stroke continues till the shaft angle 180° when the piston reaches the top dead center. During the second half of the pump cycle, the piston describes the discharge stroke pressurizing the fluid in displacement chamber and pushing it to the outlet. The pressures in the gap domain are low during the intake stroke and high in the discharge stroke when the fluid is compressed.

A closer look at the pressure fields at different instants highlights the pressure peaks that are generated due to the squeeze effects in the gap domain though piston micro-motion. These peaks are usually observed in regions where film thickness is low and piston squeeze velocities are high. Similarly, in regions where the squeeze velocities are high when the piston moves away from the cylinder surface, a trough characterized by low pressures (dark blue regions in the plot) is observed as seen at shaft angles 270° and 315° in the Figure 41.

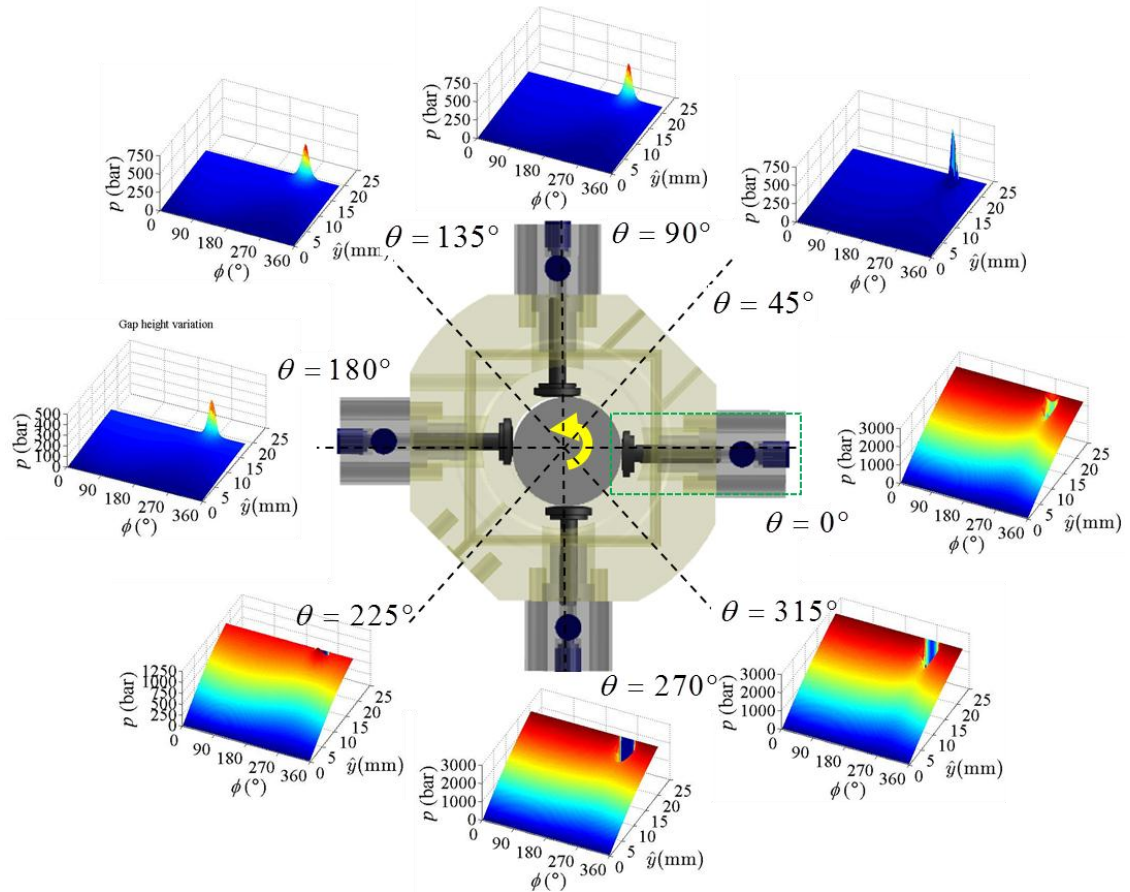


Figure 41: Instantaneous pressure field in lubricating gap domain over one shaft revolution using rigid body model. *Operating condition: Outlet pressure=2500 bar, Shaft speed=1800 rpm.*

Figure 42 shows the gap film thickness values for the same operating condition. It can be seen by comparing the two figures that regions of high pressures exist where film thickness is low and the squeeze velocities are high. Regions of low film thickness (indicated by dark blue regions in the film thickness plots) are observed more during instants when gap pressures are high ($270^\circ - 360^\circ$). The presence of extremely low gap heights in a region highlights the risk of contact that is likely to occur between the cylinder and the piston.

Figure 43 and Figure 44 illustrate the pressure field and film thickness in the gap domain respectively when results were generated using the fully coupled FSI model. Once again,

the pressure peaks and troughs are observed in regions of low film thickness due to high squeeze velocities.

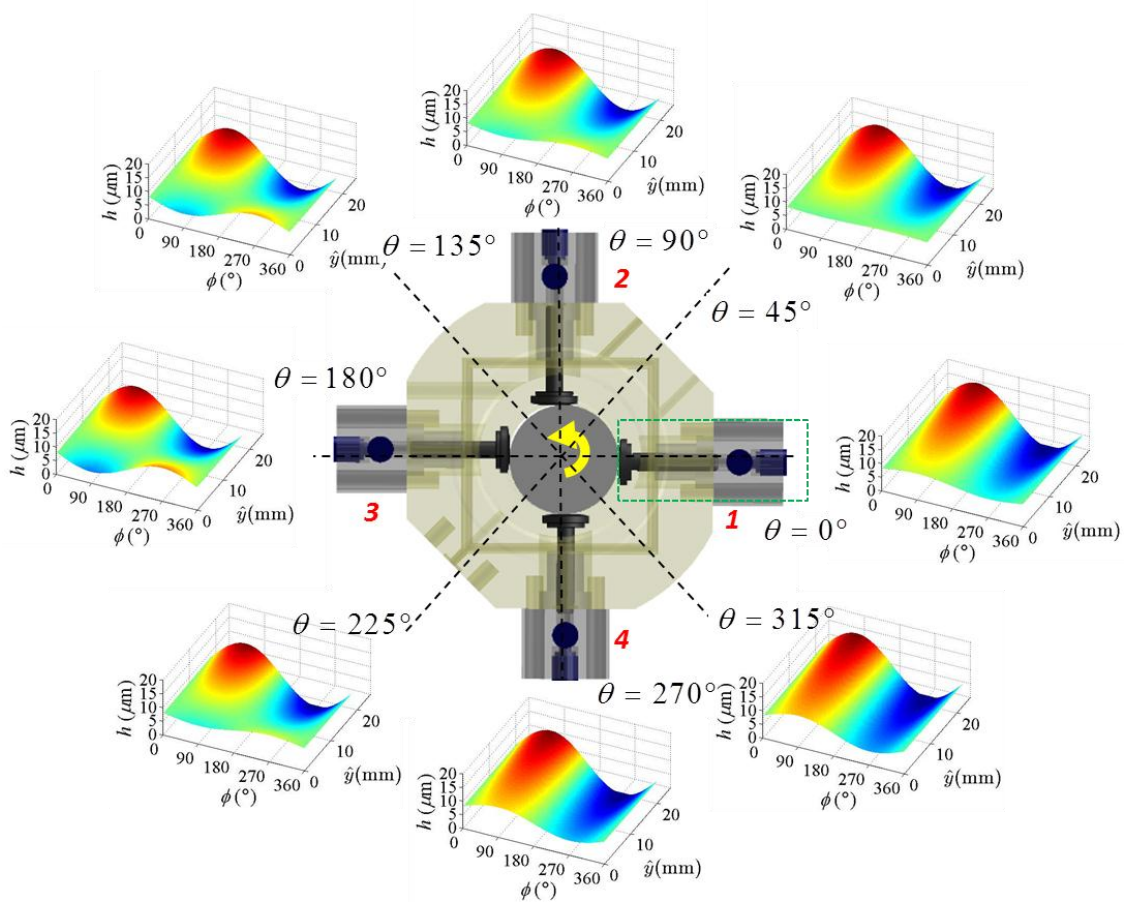


Figure 42: Instantaneous film thicknesses in lubricating gap domain over one shaft revolution using rigid body model. *Operating condition: Outlet pressure=2500 bar, Shaft speed=1800 rpm.*

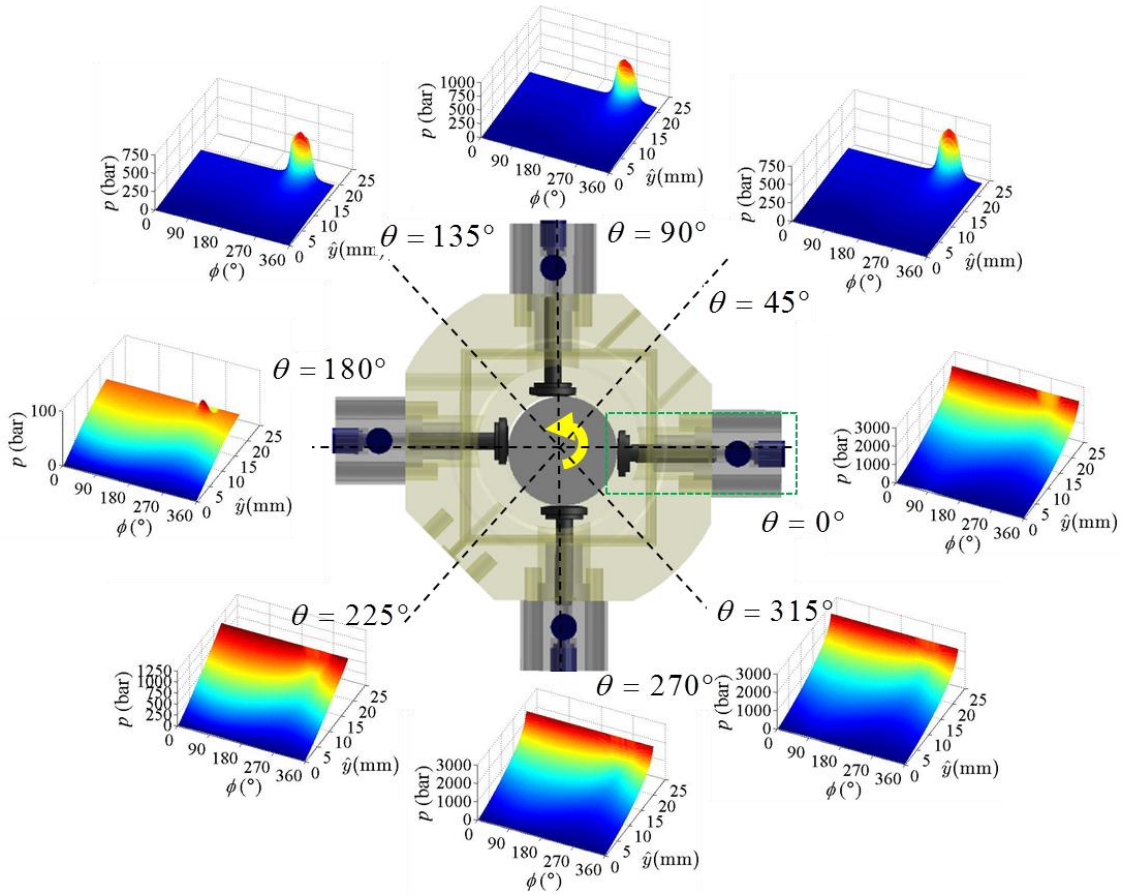


Figure 43: Instantaneous pressure field in lubricating gap domain over one shaft revolution using FSI model. *Operating condition: Outlet pressure=2500 bar, Shaft speed=1800 rpm.*

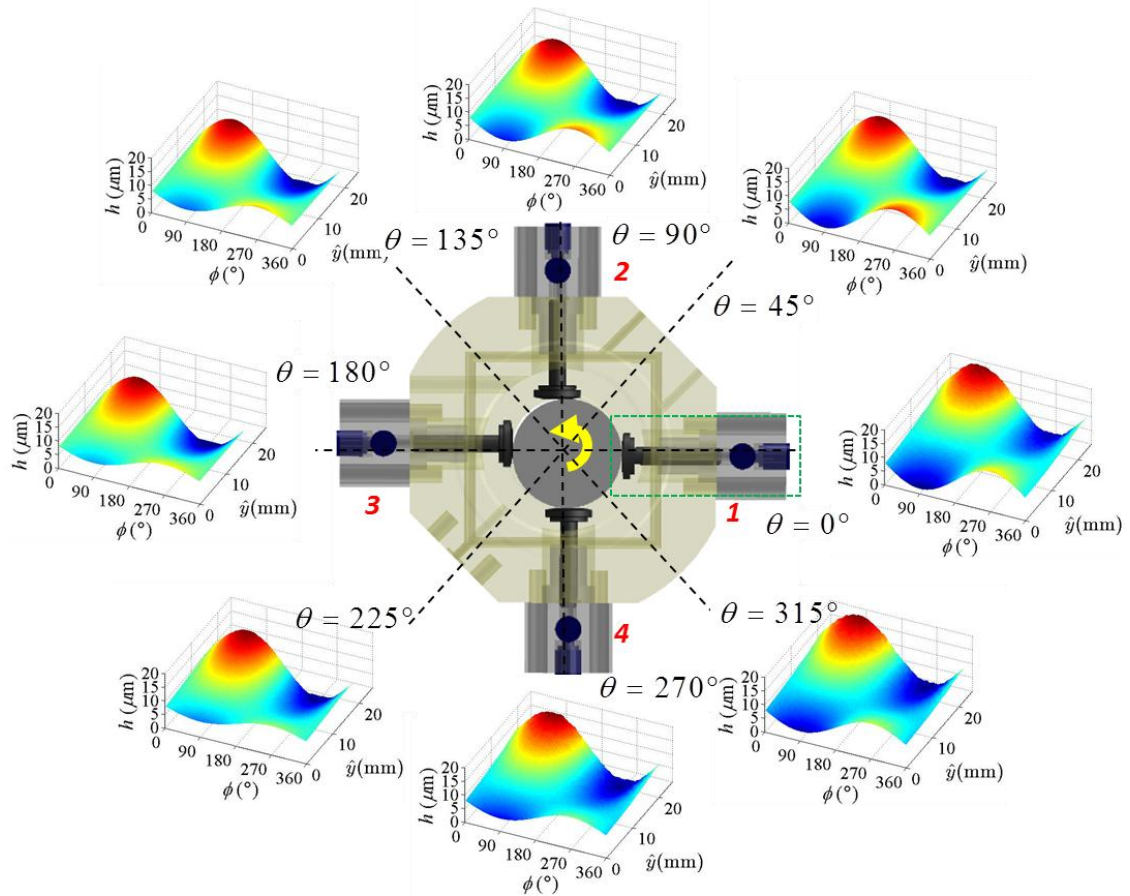


Figure 44: Instantaneous film thicknesses in lubricating gap domain over one shaft revolution using FSI model. *Operating condition: Outlet pressure=2500 bar, Shaft speed=1800 rpm.*

The FSI results show that surface deformations in the order of $1 - 5 \mu\text{m}$ are generated in the gap domain which has a significant effect on the overall hydrodynamic pressure generation in the lubricating interface. Figure 46 shows the comparison between the rigid and FSI models for minimum film thickness at varying shaft angles. The rigid model predicts extremely low film thickness ($\approx 0.2 \mu\text{m}$) in most instants in shaft revolution which implies contact between the solid surfaces. However, in actual pump operation this contact may not be observed since the elastic deformation in surfaces increases the gap height in those critical regions and hydrodynamic effects in the oil film are sufficient to support the loads. This effect is better captured using the FSI model as seen in Figure 46 which predicts more accurate film thickness values over the shaft revolution. Therefore,

the results obtained using the FSI model are more realistic and are used for subsequent analysis throughout the study.

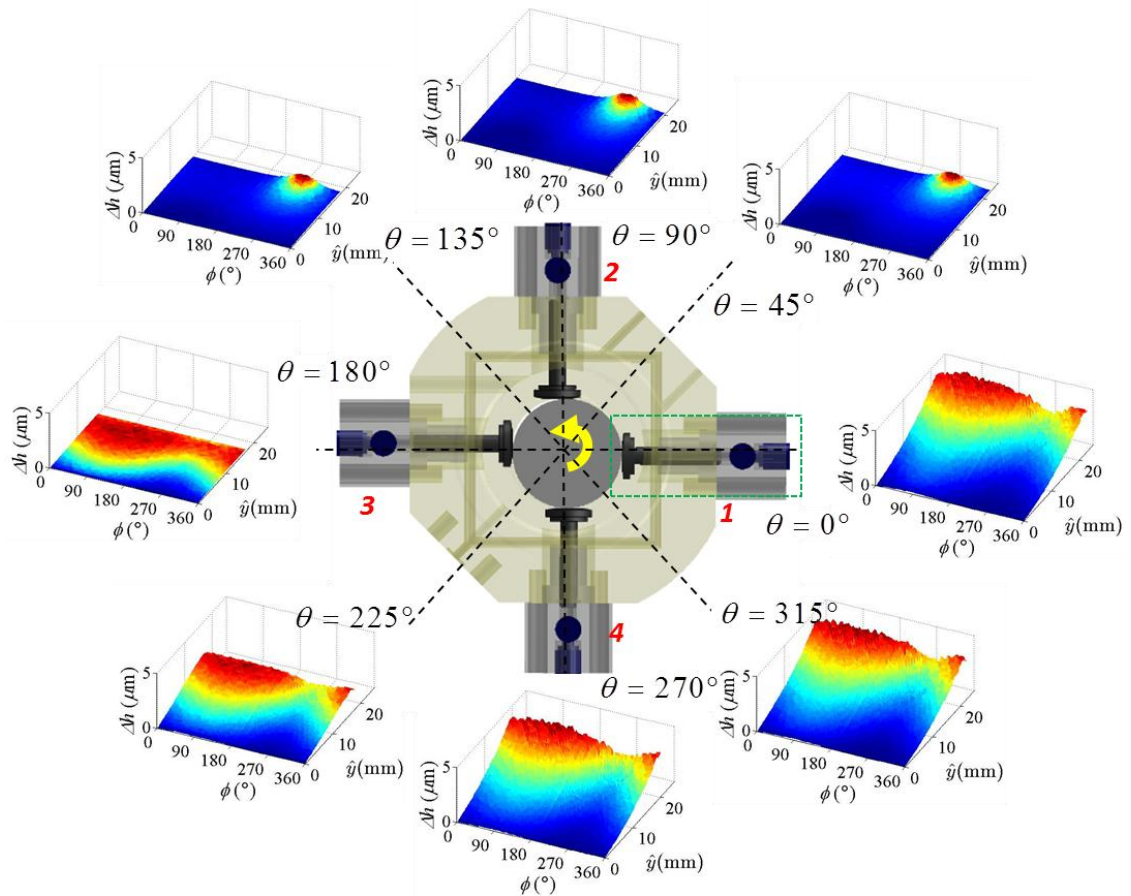


Figure 45: Instantaneous elastic deformation in lubricating gap domain over one shaft revolution. *Operating condition: Outlet pressure=2500 bar, Shaft speed=1800 rpm.*

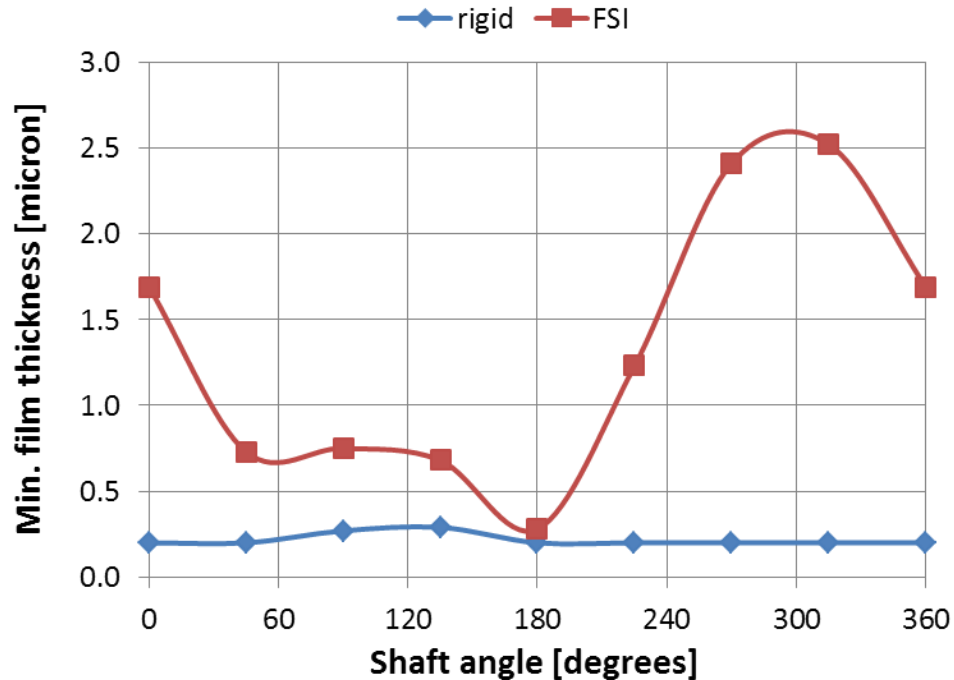


Figure 46: Comparison of minimum film thickness generated using rigid body model and FSI model. *Operating condition: Outlet pressure=2500 bar, Shaft speed=1800 rpm.*

4.6.2 Evaluation of Performance Parameters using the FSI Model

This section discusses the simulation results pertaining to the critical performance parameters associated with the pump operation. The gap model is capable of predicting,

- The leakage flow occurring through the gap interface that determines the volumetric efficiency of the pump.
- Power losses due to viscous forces acting on the moving piston which affect the mechanical efficiency of the pump.

Figure 47 shows the variation of leakage flow through a single piston-cylinder gap region with shaft angle in a single pump operating cycle. The leakage flow is found to be more when there are higher pressures in the displacement chamber and is significantly less when the pressures are low ($\approx 45^\circ - 170^\circ$). The mean leakage flow rate can be calculated by adding leakage flows from all four displacement chambers and averaging over a pump cycle. The instantaneous viscous friction forces acting on the piston are shown in Figure 48.

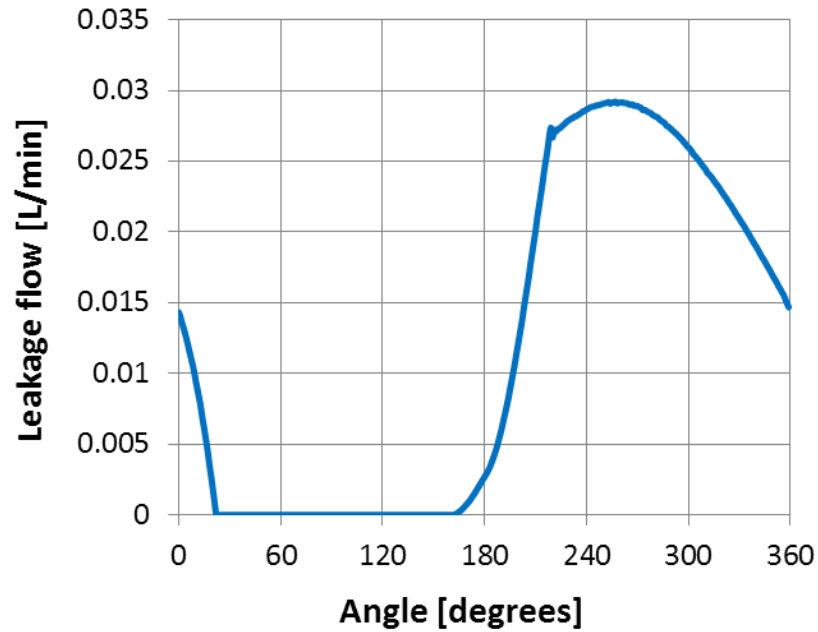


Figure 47: Instantaneous leakage flow rate through a single piston-cylinder interface. *Operating condition: Outlet pressure=700 bar, Shaft speed=1800 rpm.*

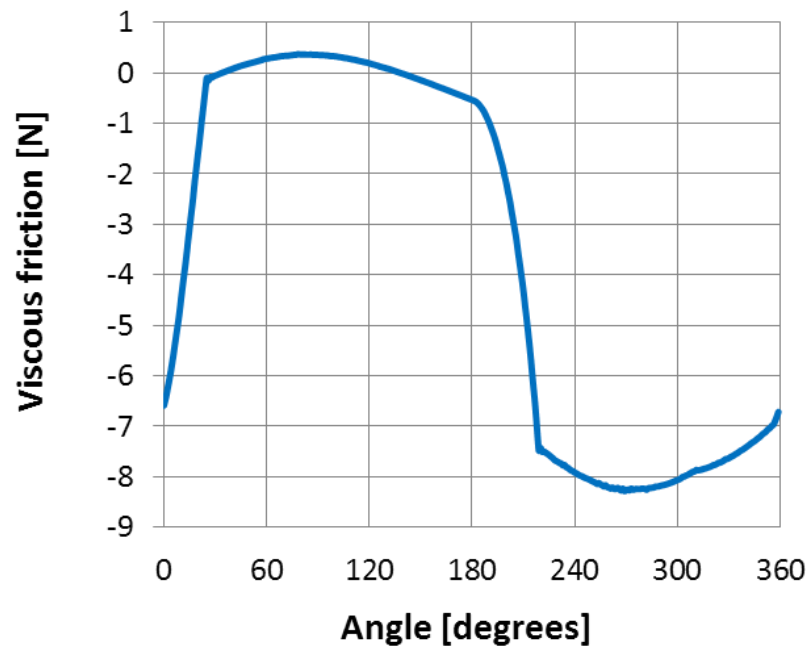


Figure 48: Instantaneous viscous friction force acting on a single piston. *Operating condition: Outlet pressure=700 bar, Shaft speed=1800 rpm.*

In order to study the correlation between the performance parameters and pump operating conditions, multiple simulations were run at different outlet pressures. Figure 49 shows

the change in leakage flow and the viscous friction power losses as the outlet pressure of the pump is increased from 700 to 2500 bar. It is easy to observe that an increase in pump outlet pressure increases the pressure gradient between the displacement chamber and the drain area which results in more fluid leaking through the interface. Also, the shear stress acting in the piston surface due to viscous friction forces is dependent on the pressure gradient existing in the gap domain. At higher pressures, a higher gradient results in an increased viscous forces which translated into more viscous power losses. These results demonstrate the capability of the simulation tool to handle a wide range of operating conditions and generate performance parameters. Though the leakage and viscous loss results need to be verified experimentally, the numerical procedure predicts a correct variation of these parameters with changing shaft angles and also with a change in operating conditions. The correlations observed in the plots shown above agree well with the simplified analytical models that do not take into account the piston micro-motion and hydrodynamic pressure generation.

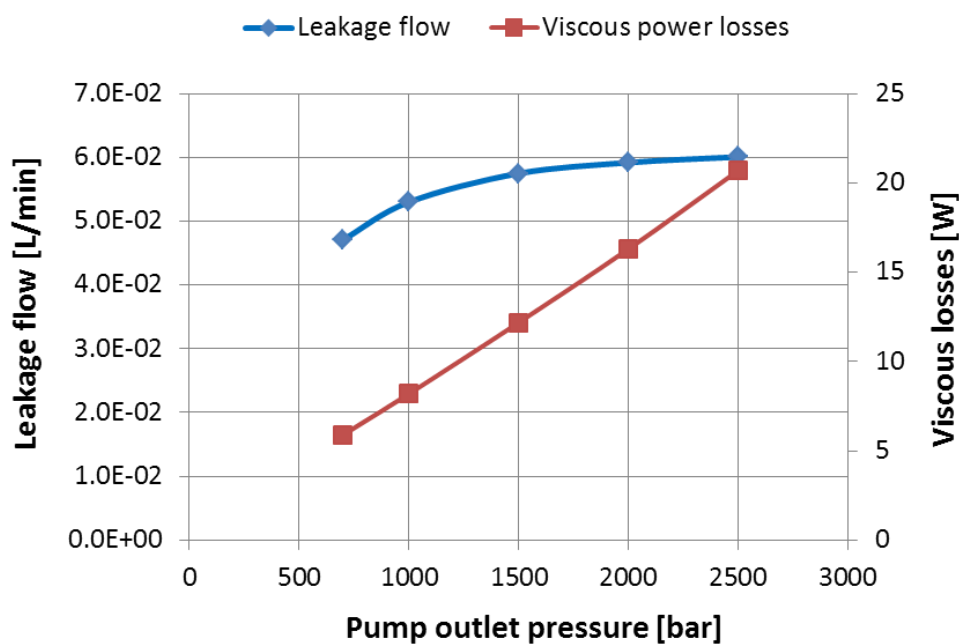


Figure 49: Leakage flow and viscous power losses at different outlet pressures. *Shaft speed=1800 rpm.*

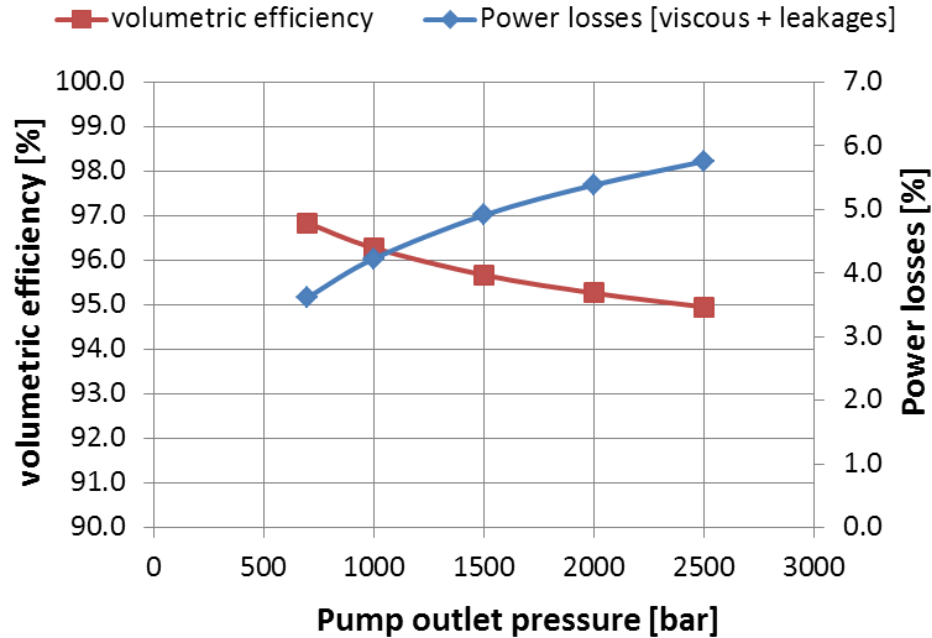


Figure 50: Volumetric efficiencies and outlet flow rates at different outlet pressures. *Shaft speed=1800 rpm.*

4.6.3 Effect of Changing Clearance on Simulation Results

It was seen in the previous section that at ultra-high outlet pressures ($\approx 2500 \text{ bar}$), the FSI simulations predicted a large leakage flow occurring through the piston-cylinder interface. Figure 50 shows the variation of volumetric efficiency over the same range of outlet pressures keeping the shaft speed constant. It is important to note that the actual volumetric efficiency of the pump system will be less than shown values since the flow losses due to check valves and charge pump are not taken into account. Since the inlet flow remains unchanged due to fixed shaft speeds, an increase in leakage flow implies a decrease in volumetric efficiency. Also, the power losses occurring due to leakage flow and viscous losses are found to increase at higher operating pressures.

In order to test the potentials of the simulation tool and check if a change in clearance between the piston and cylinder can bring improvements in volumetric efficiencies at high pressures, simulations were run at different values of clearances. The piston-cylinder clearance is a critical factor that governs the amount of leakages flow and hence the volumetric efficiency of the pump. Intuitively, a smaller clearance implies a decreasing

flow area for the gap domain which reduces the leakage flow occurring through the lubricating interface. However, a smaller clearance increases the possibility of contact between the piston and cylinder which can be detrimental to the pump performance by causing wear of the solid parts.

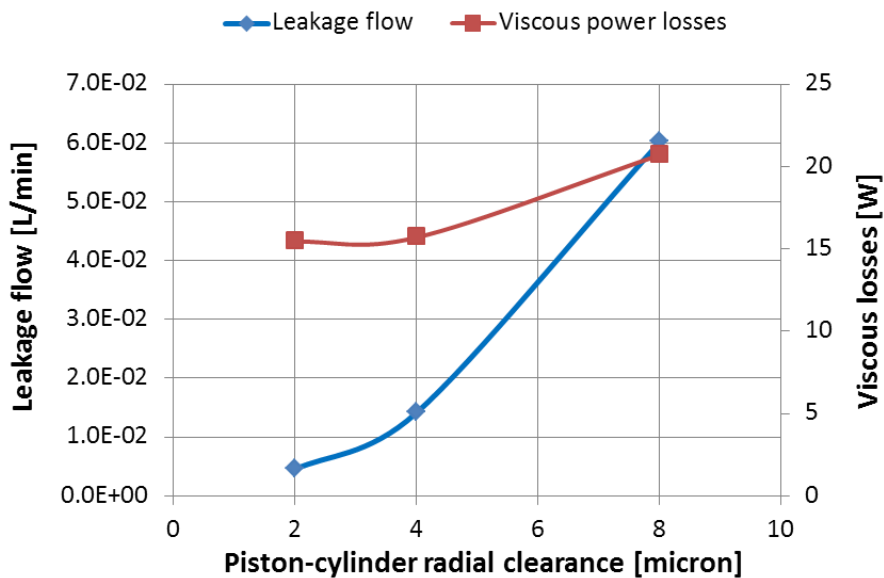


Figure 51: Leakage flow and viscous power losses at different piston-cylinder clearances. *Outlet pressure= 2500 bar, Shaft speed=1800 rpm.*

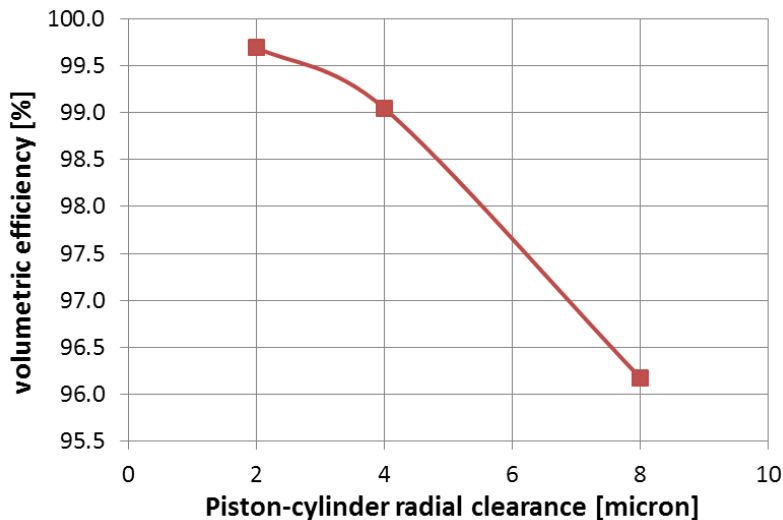


Figure 52: Volumetric efficiency at different piston-cylinder clearances. *Outlet pressure = 2500 bar, Shaft speed=1800 rpm.*

Figure 51 and Figure 52 show a comparison between the performance parameters obtained at different clearance values. It can be seen from the figures that decreasing the clearance between the piston and cylinder is instrumental in increasing the pump volumetric efficiency by minimizing the leakage flow. However, the viscous friction losses which were expected to increase at low clearances are also found to decrease. This can be explained by the analyzing the simulation results at low clearances.

Figure 53 shows the surface deformation field at varying shaft angles in a pump revolution for radial clearance of $2\mu\text{m}$ between the piston and cylinder. It is observed that the order of elastic deformation is significantly higher ($\approx 5\mu\text{m}$) than the clearance itself. This causes the gap heights to increase during pump operation and the actual distance between piston and cylinder is now much larger which leads to a decrease in viscous losses.

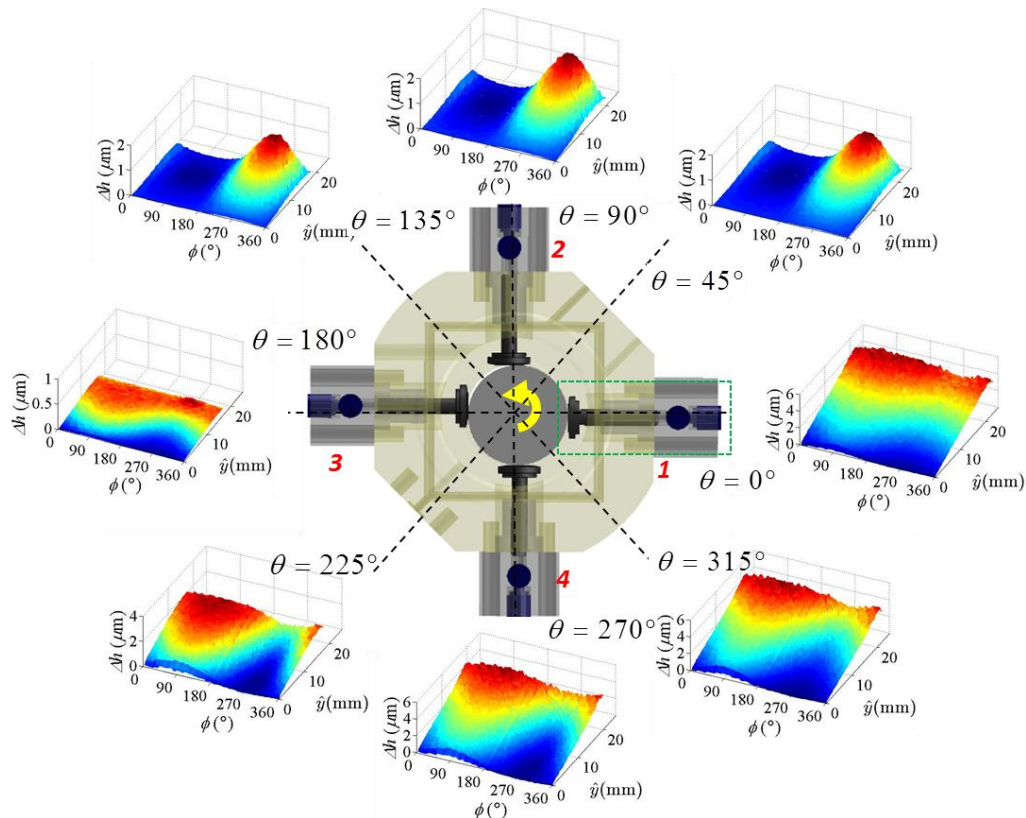


Figure 53: Instantaneous elastic deformation in lubricating gap domain over one shaft revolution for piston-cylinder radial clearance= $2\mu\text{m}$. Operating condition: Outlet pressure= 2500 bar , Shaft speed= 1800 rpm .

The decrease in viscous friction losses predicted by the numerical model might not be true in actual pump operation since at low clearances, there are possibilities of asperity contact occurring between solid surfaces. Figure 54 shows the film thickness distribution for the same operating condition. It is seen that there are large number of regions (dark blue regions in the figure) when the film thicknesses are extremely low.

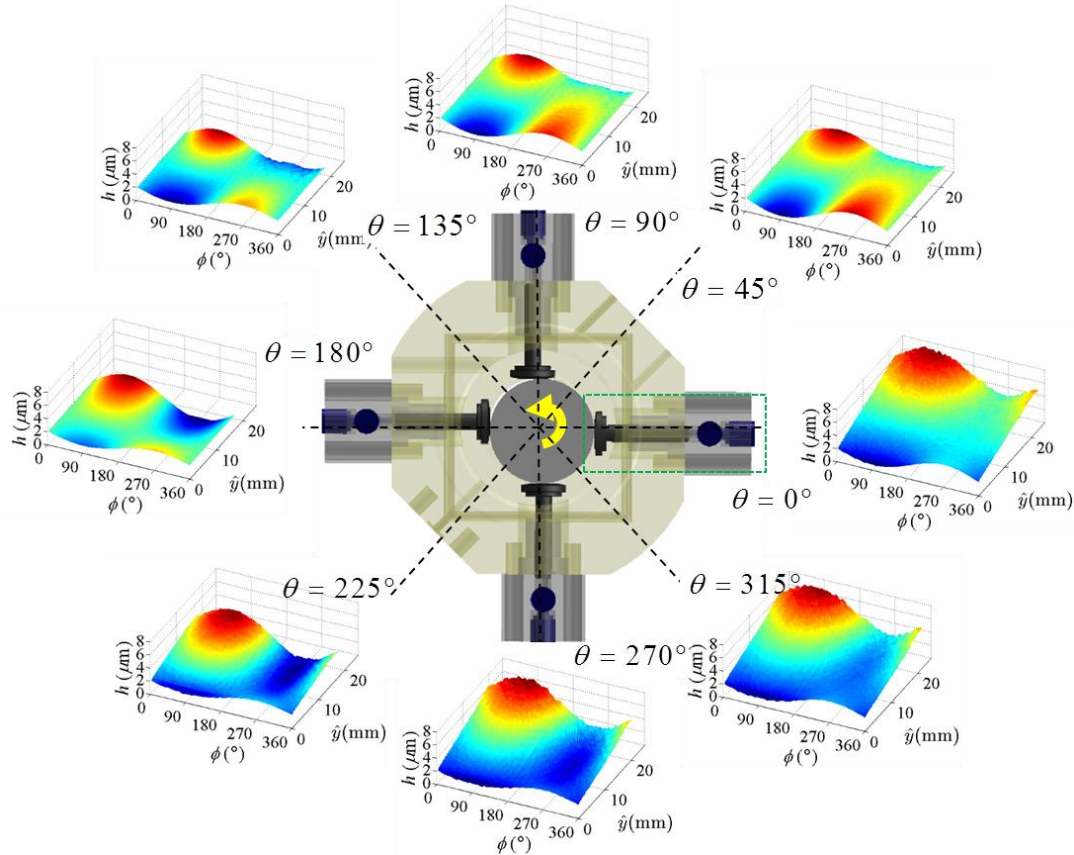


Figure 54: Instantaneous film thickness over one shaft revolution for piston-cylinder radial clearance= $2\mu\text{m}$. Outlet pressure = 2500 bar, Shaft speed=1800 rpm.

The minimum film thickness values are found close to $1\mu\text{m}$ (refer Figure 55) which hints at possible contact between the piston and cylinder surfaces. Contact between the solid surfaces creates large shear stresses on the moving piston which increase the frictional losses drastically. This results in a poor mechanical efficiency and wear of the piston surface. In order to analyze the regime of such low film thicknesses accurately, a mixed/partial EHL lubrication model needs to be developed that can predict the flow parameters and power losses more accurately. Moreover, the current EHL model is based

on an isothermal assumption while high shear stresses acting on solid parts imply large heat generation which affects the fluid behavior significantly. These considerations might be included as a future improvement over the current model.

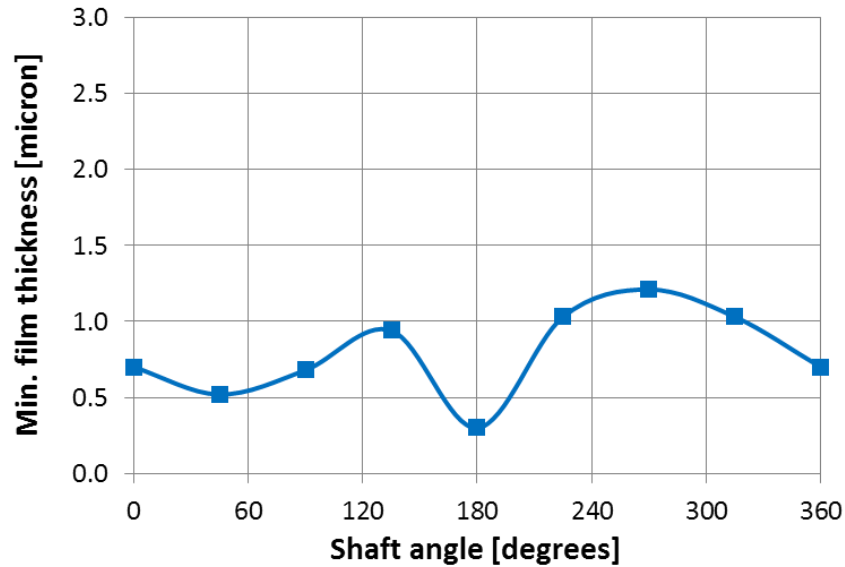


Figure 55: Minimum film thickness over one shaft revolution for piston-cylinder radial clearance = $2\mu\text{m}$. *Outlet pressure = 2500 bar, Shaft speed = 1800 rpm.*

It is important to note that the current EHL model based on FSI is successful in predicting the impact of elastic deformation on the behavior of the fluid film in the piston – cylinder interface at low clearances. Since there is significant elastic deformation at piston and cylinder surfaces (as seen in the figure), there is still scope of finding an optimum design at such low clearances which can prevent a possible contact if the design is changed suitably and appropriate materials chosen.

CHAPTER 5. CAM-PISTON INTERFACE

This chapter presents a detailed discussion on modeling of the cam-piston lubricating interface. Figure 56 shows the geometry of the cam-piston interface as present in a pump prototype that is similar to the reference pump design. The springs and the rolling element bearings present in the pump are not depicted in the CAD illustrations for the same but are important components for smooth pump operation. In CHAPTER 4, it was demonstrated that the numerical model for piston-cylinder interface is capable of generating results at varied operating conditions which confirm well with theory. However while evaluating the force balance of the piston (as shown in Figure 56), a major assumption was made by considering a constant friction coefficient ($\mu = 0.1$) between the cam and piston which is representative of a pure sliding condition. In actual pump geometry, the dynamic conditions of contact load and cam and piston velocities govern the value of friction coefficient which can vary greatly during the operating cycle.

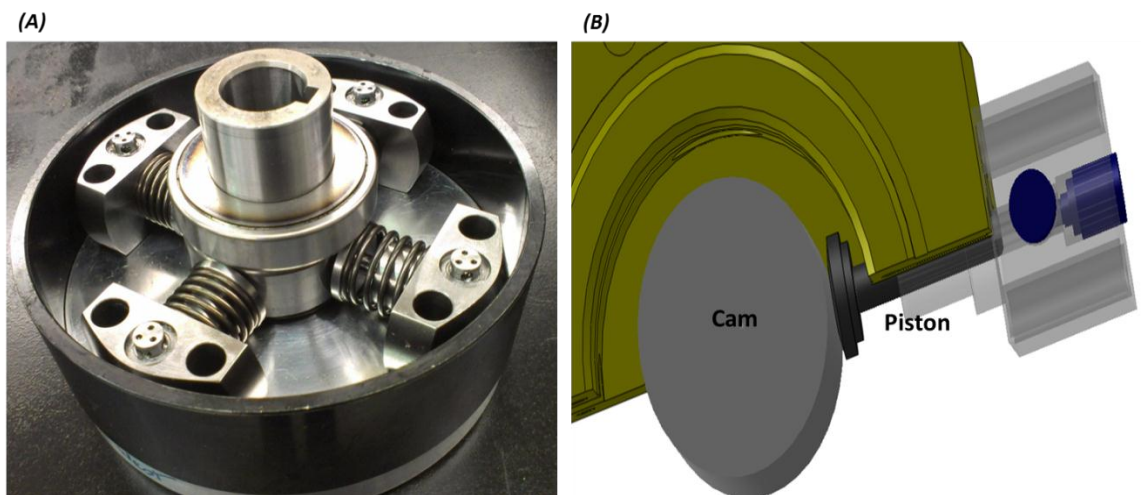


Figure 56: Cam-piston lubricating interface. (a) Reference pump geometry (b) CAD illustration for the same.

The problem of finding an accurate prediction of the instantaneous friction forces can be approached by using different methods. The experimental method involves performing measurements using a customized test rig that simulates the actual dynamics of the cam and piston motion and measure the traction coefficient in the line contact between the solid surfaces. However, such a process would involve construction of a test setup which is time consuming and costly. Also, measurements need to be taken for a wide range of operating conditions before reliable curve fit data can be generated. A second approach for solving the same is by using empirical models. Though there are many empirical relations available in literature [62-67] for predicting the film thickness for line EHL conditions, few such models exist for predicting the friction force acting in the interface [40-43]. Another drawback of using an empirical approach is that most of the available models are not generic and are applicable for a specific set of material and fluid properties.

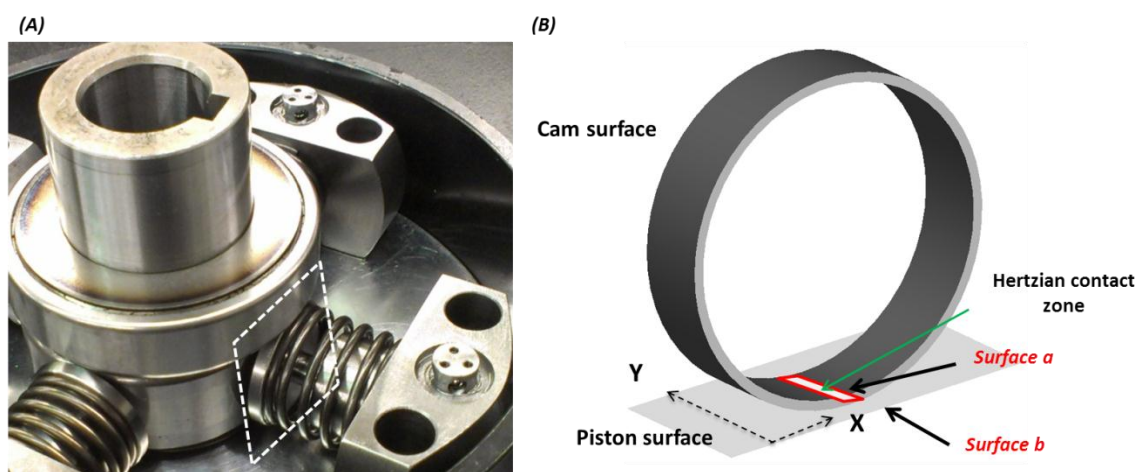


Figure 57: Geometry of the cam piston contact interface. (a) in reference pump geometry
(b) equivalent line contact geometry between a cylinder and a plane.

In this study, the numerical procedure developed in [64] is adopted to evaluate the pressure field and film thickness in the interface under lubricating conditions. The geometry of the contact region between the cam and piston is equivalent to a line contact between a cylinder and a plane as shown in Figure 57. This section presents the details of the friction model that was developed to simulate the line contact between the cam and piston operating in EHL regime followed by the simulation results.

5.1 EHL Model

Radial piston pumps are typically operated at higher operating pressures particularly when they are used for generating high forces in hydraulic tools. High pressures in displacement chambers of these machines result in large loads acting at the cam-piston interface. An efficient design of this interface requires the friction between cam and piston to be minimum so that there is less wear in the contacting surfaces. This can be achieved by changing the contact geometry in multiple ways as shown in Figure 58,

- Using a hydrostatic slipper that receives high pressure fluid from the piston bore as commonly found in axial piston machines.
- By using a roller at the piston end, similar to cam-tappet interfaces in camshafts of IC engines that reduces the relative motion between contacting surfaces.
- Incorporating the eccentric cam in rolling element bearings with the outer race in contact with the moving piston.

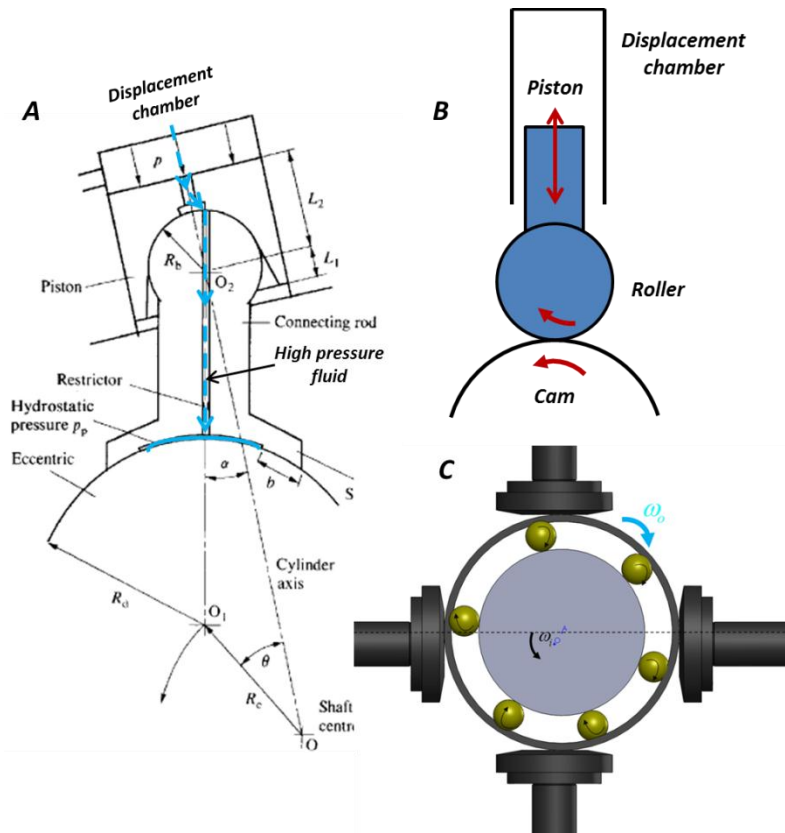


Figure 58: Different configurations of cam-piston contact. (A) Hydrostatic slipper as analyzed in [1] (B) Roller support (C) Rolling element bearing.

Each of these modified designs are governed by different dynamics corresponding to lubricant flow, relative motion and contact loads. However, high loads acting at the contacting interface result in the EHL lubrication regime between the moving surfaces. In this section, development of a generic line EHL friction model is discussed which can compute the instantaneous friction existing in a line contact for a wide range of input conditions corresponding to surface velocities and loads. The contact loads acting in the interface can be easily calculated using the given parameters and piston kinematics while surface velocities of cam and piston need to modeled accurately or experimentally measured as an input to the friction model. The following sub-sections detail out the complete procedure used for developing the numerical model,

5.1.1 Governing Equations

Figure 57b shows the geometry of the cam-piston interface which is essentially a line contact between cam and piston. The flow of the lubricant through a line contact is governed by the 1-D Reynolds equation [48] which can be stated as,

$$\frac{d}{dx} \left(\frac{\rho h^3}{12\eta} \frac{dp}{dx} \right) - u_e \frac{d(\rho h)}{dx} = \frac{dh}{dt} \quad (5.1)$$

The squeeze term $\frac{dh}{dt}$ in Equation (5.1) is neglected to simplify the analysis. Also, isothermal conditions are assumed in the contact throughout this study. The film thickness existing in the lubricating domain can be defined as,

$$h(x) = h_0 + S(x) + \delta(x) \quad (5.2)$$

where h_0 =constant, $S(x)$ = separation due to geometry of undeformed solids, $\delta(x)$ = elastic deformation of solids. The geometric separation while assuming a parabolic approximation of cylinder-place contact is, $S(x) = \frac{x^2}{2R_x}$

Owing to the small contact region and high loads, the pressures generated in the contact zone are extremely high which leads to significant elastic deformation of contacting bodies at the interface.

This deformation can be calculated by,

$$\delta = -\frac{2}{\pi E'} \int_{x_{min}}^{x_{max}} p \ln(x - x')^2 dx \quad (5.3)$$

where x is the point where deformation is being calculated and p is a function of x' varying from x_{min} to x_{max} . The effective modulus of elasticity of the two contacting surfaces E' is defined as [48],

$$\frac{1}{E'} = \frac{1}{2} \left(\frac{1 - \nu_a^2}{E_a} + \frac{1 - \nu_b^2}{E_b} \right) \quad (5.4)$$

At steady state conditions, the pressure generated by the fluid film should be sufficient to bear the contact load, which gives the force-balance condition,

$$w' = \int p dx \quad (5.5)$$

The dependence of the density involved in equation is modeled using the Dowson and Higginson relation [68]. The Barus viscosity expression [69] is used to model the change in viscosity with pressure.

$$\rho = \rho_0 \left(1 + \frac{0.6p}{1 + 1.7p} \right) \quad (5.6)$$

$$\eta = \eta_0 e^{\alpha_p p} \quad (5.7)$$

The variation of viscosity is a critical factor that influences the fluid behavior in a line EHL contact since the viscosity of lubricant increases drastically as it enters the contact zone. The system of equations as stated above is non-dimensionalized by defining the following set of parameters,

$$\bar{P} = \frac{p}{p_H}, X = \frac{x}{R_x}, \bar{\rho} = \frac{\rho}{\rho_0}, \eta = \frac{\eta}{\eta_0}, H = \frac{h R_x}{b^2}, b = R_x \sqrt{\frac{8W'}{\pi}}, W' = \frac{w'_z}{E' R_x} \quad (5.8)$$

$$U_e = \frac{\eta_0 u_e}{E' R_x}, G = \alpha_p E'$$

where p_H is the Hertzian pressure developed in the line contact region defined as $p_H =$

$$E' \sqrt{\frac{W'}{2\pi}}$$

and b is the half Hertzian width.

Using the above non-dimensional parameters, Equation (5.1) neglecting the squeeze term can be rewritten in the following form:-

$$\frac{d}{dX} \left(\xi \frac{d\bar{P}}{dX} \right) - \frac{d(\bar{\rho}H)}{dX} = 0 \quad (5.9)$$

$$\text{where } \xi = \frac{\bar{\rho}H^3}{\eta\lambda} \text{ and } \lambda = \frac{3u_e}{4} \left(\frac{\pi}{W'} \right)^2$$

The grouping of the terms is done in this manner to separate out the parameter ξ which depends on the load parameter and governs the stability of the numerical scheme employed to solve the Reynolds equation.

Similarly, the dimensionless film thickness equation can be written as,

$$H(X) = H_0 + \frac{X^2}{2} - \frac{1}{\pi} \int_{X_a}^{X_b} \bar{P}(X) \ln |X - X'| dX \quad (5.10)$$

It is important to note the difference in velocity terms involved in this study for solving the EHL problem. The velocity parameter (u_e) defined in Equation (5.8) is representative of the lubricant entrainment velocity which is equal to rate of lubricant flow in the inlet region of the contact. Similarly, the sliding velocity parameter (u_s) represents the relative motion between the solid surfaces involved in the contact. The ratio of the sliding velocity to the entrainment speed is defined as the slide-roll ratio (*SRR*). These velocity parameters can be defined mathematically in terms of surfaces velocities as,

$$u_e = (u_1 + u_2)/2 \quad (5.11)$$

$$u_s = (u_1 - u_2) \quad (5.12)$$

$$SRR = \frac{u_s}{2u_e} \quad (5.13)$$

where u_1, u_2 are velocities of upper and lower surface respectively with respect to the contact point between the surfaces [70].

5.1.2 Discretization of Lubricating Domain

In order to solve for pressure generation for lubricant flow in the contact region, the domain is discretized into a 1-D grid along contact length as shown in Figure 59 with the length of the domain ranging from X_{min} to X_{max} .

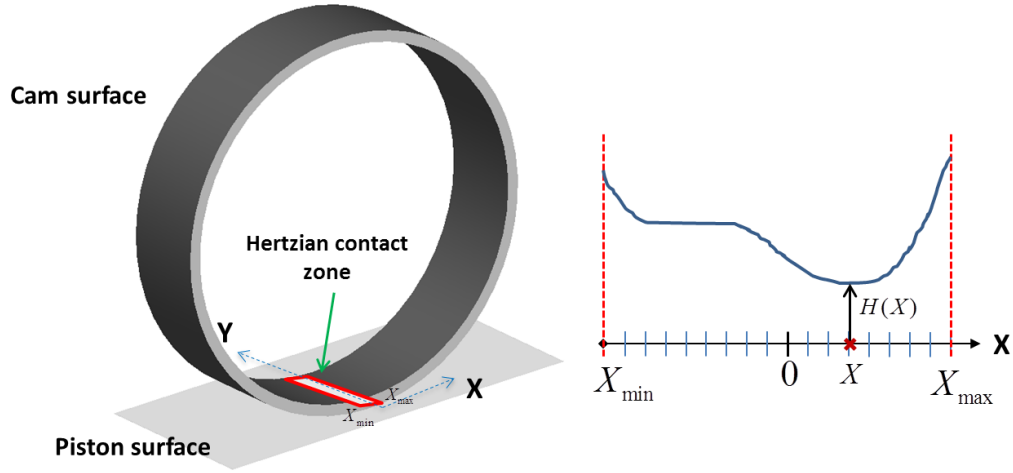


Figure 59: Lubricating gap domain between the piston and cylinder in line EHL.

Equation (5.9) is discretized using a second order central discretization for the Poiseuille term and first order upstream discretization for the wedge term in order to keep the iterative process stable. Using such a scheme, the discretized equation at point i can be written as,

$$\frac{(\xi_{i-\frac{1}{2}}\bar{P}_{i-1} - (\xi_{i-\frac{1}{2}} + \xi_{i+\frac{1}{2}})\bar{P}_i + \xi_{i+\frac{1}{2}}\bar{P}_{i+1})}{(\Delta X)^2} - \frac{(\bar{\rho}_i H_i - \bar{\rho}_{i-1} H_{i-1})}{\Delta X} = 0 \quad (5.14)$$

Discretization of Equation (5.10) results in,

$$H_i = H_0 + \frac{X_i^2}{2} - \frac{1}{\pi} \sum_{j=1}^n K_{ij} \bar{P}_j \quad (5.15)$$

where K_{ij} are the associated influence coefficients and can be defined as,

$$K_{ij} = \left(i - j + \frac{1}{2}\right) \Delta X \left(\ln\left(\left|i - j + \frac{1}{2}\right| \Delta X\right) - 1\right) - \left(i - j - \frac{1}{2}\right) \Delta X \left(\ln\left(\left|i - j - \frac{1}{2}\right| \Delta X\right) - 1\right) \quad (5.16)$$

The dimensionless force balance equation, stating that the integral over the pressure should be equal to the externally applied load, reads as,

$$\Delta X \sum_{j=1}^{n-1} \frac{\bar{P}_j + \bar{P}_{j+1}}{2} = \frac{\pi}{2} \quad (5.17)$$

5.1.3 Incorporating Non-Newtonian Fluid Behavior

One of the key factors which influence the friction behavior in a line contact interface is the sliding motion that exists between the surfaces. In ideal cases, a line contact is characterized by a pure rolling motion associated with the movement of cylinder over flat plane. However, real time situations may involve large sliding velocities existing between surfaces in addition to a rolling component that changes the behavior of the fluid entering the contact zone. High sliding velocities result in large shear stresses acting at the surfaces. At such high values of shear stress, the fluid can no longer be treated as a Newtonian fluid and appropriate non-Newtonian models have to be incorporated in order to obtain a realistic prediction of the traction/friction forces. Since the radial piston pump can have large variations of rolling and sliding speeds at the cam-piston interface, a versatile EHL model that is capable of generating accurate solutions at both low and high sliding velocities is required. As described earlier, several non-Newtonian models have been used to model the lubricant behavior in EHL contacts [35-37]. However in this study, a simplified non-Newtonian model developed in [71] is used. Figure 60 shows the effect of the shear stress on shear strain rate for the present model and that of a Newtonian fluid. From the figure, it is observed that in the present model, if the Newtonian shear stress exceeds the limiting shear stress, the shear stress is set equal to the limiting shear stress. The fluid model is Newtonian except when the shear stress reaches the shear strength value. At that point, slippage occurs and shear stress is saturated to the shear strength value.

The limiting shear stress used in the present non-Newtonian model can be defined as,

$$\tau_L = \tau_0 + \gamma p \quad (5.18)$$

where τ_0 represents the shear strength and γ is the limiting shear strength proportionality constant.

To incorporate in the numerical procedure, the shear stress term can be non-dimensionalized as,

$$\bar{\tau} = \frac{\tau}{E'} \quad (5.19)$$

Using the above relation, Equation (5.18) can be non-dimensionalized as,

$$\bar{\tau}_L = \bar{\tau}_0 + \gamma \bar{P} \quad (5.20)$$

The value of $\bar{\tau}_0$ usually ranges from 10^{-5} to 10^{-4} while γ can vary from 0.04 and 0.1. For the simulation results shown in this study, $\bar{\tau}_0 = 9 \times 10^{-5}$ and $\gamma = 0.07$.

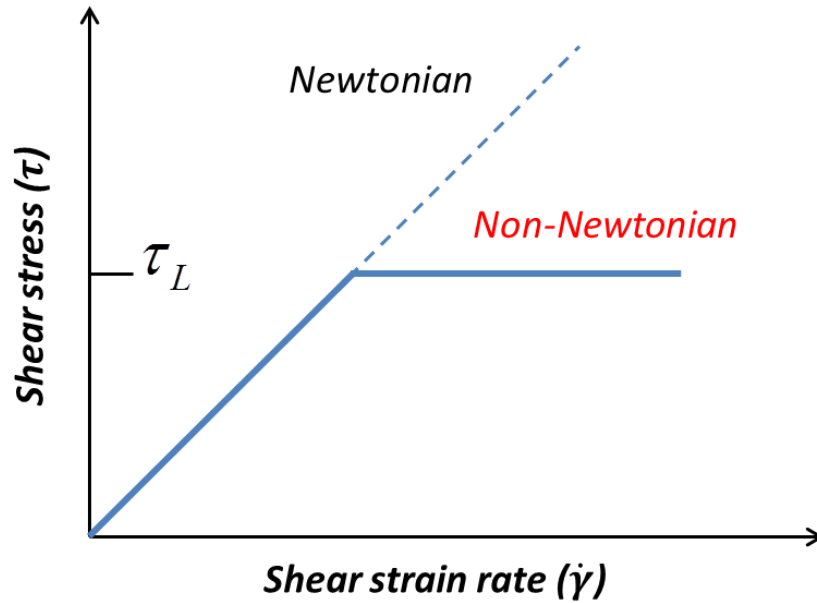
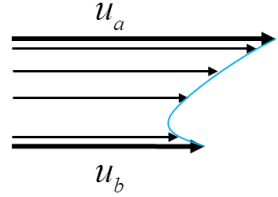
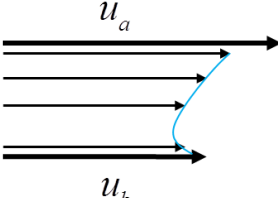
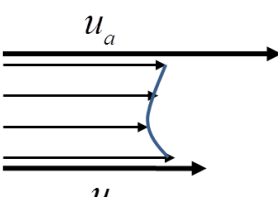
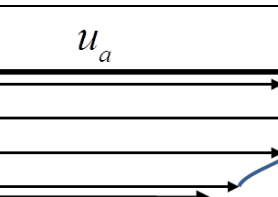
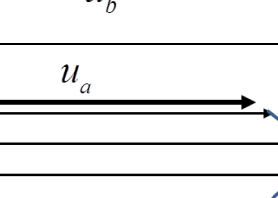


Figure 60: Lubricant model used in Jacobson, Hamrock [12].

Using such a non-Newtonian model, the fluid velocity can be described in terms of five distinct zones that might exist in the elastohydrodynamic conjunction. Table 4 shows a brief description of each zone in terms of velocity field and shear stress (non-dimensional) values [71].

Table 4: Velocity distributions in different lubricating conditions.

Zone no.	Velocity Distribution	Slippage condition	Shear stress at both surfaces
0 (Newtonian)		No slippage	$\bar{\tau}_a < \bar{\tau}_L, \bar{\tau}_b < \bar{\tau}_L$
1 (non-Newtonian)		Slippage at surface a	$ \bar{\tau}_a > \bar{\tau}_L, \bar{\tau}_b < \bar{\tau}_L$
2 (non-Newtonian)		Slippage at surface b	$\bar{\tau}_a < \bar{\tau}_L, \bar{\tau}_b > \bar{\tau}_L$
3 (non-Newtonian)		Slippage at both surfaces	$\bar{\tau}_a > \bar{\tau}_L, \bar{\tau}_b < -\bar{\tau}_L$
4 (non-Newtonian)		Slippage at both surfaces	$\bar{\tau}_a < -\bar{\tau}_L, \bar{\tau}_b > \bar{\tau}_L$

In order to incorporate the effects of non-Newtonian fluid behavior in the numerical procedure, the pressure field is generated by solving the Newtonian form of Reynolds equation.

This pressure field is used to evaluate the shear stresses acting on both surfaces ($\bar{\tau}_a$ and $\bar{\tau}_b$) at each point in the computational domain using,

$$\bar{\tau}_a = \frac{\pi}{4W'} \frac{U_e(SRR)\bar{\eta}}{H} + \frac{W'H}{\pi} \left(\frac{d\bar{P}}{dX} \right) \quad (5.21)$$

$$\bar{\tau}_b = \frac{\pi}{4W'} \frac{U_e(SRR)\bar{\eta}}{H} - \frac{W'H}{\pi} \left(\frac{d\bar{P}}{dX} \right) \quad (5.22)$$

The evaluated shear stresses are compared with conditional criteria shown in Table 4 to find out the corresponding zone for each point in the domain. Henceforth, an appropriate non-Newtonian formulation of Reynolds equation is chosen for the point as listed in Table 5. Derivation of each of these formulations can be followed in [71]. Solving the corresponding equations for respective zones, each point in pressure field is updated to complete one sweep across the mesh.

Table 5: Non-Newtonian formulation of Reynolds equation.

Zone	Reynolds equation formulation using non-Newtonian model
0	(<i>Newtonian</i>) Same as Equation (5.9)
1	$\left(\frac{8W'}{\pi} \right)^2 \frac{d}{dX} \left[\frac{\bar{\rho}}{\bar{\eta}} H^3 \frac{d\bar{P}}{dX} \right] = 6U_e \sqrt{\frac{2W'}{\pi}} \left[(1 - SRR) \frac{d(\bar{\rho}H)}{dX} + \frac{4W'}{\pi U_e} \frac{d}{dX} \left[\frac{\bar{\rho}}{\bar{\eta}} \bar{\tau}_L H^2 \right] \right]$
2	$\left(\frac{8W'}{\pi} \right)^2 \frac{d}{dX} \left[\frac{\bar{\rho}}{\bar{\eta}} H^3 \frac{d\bar{P}}{dX} \right] = 6U_e \sqrt{\frac{2W'}{\pi}} \left[(1 + SRR) \frac{d(\bar{\rho}H)}{dX} - \frac{4W'}{\pi U_e} \frac{d}{dX} \left[\frac{\bar{\rho}}{\bar{\eta}} \bar{\tau}_L H^2 \right] \right]$
3	$\frac{d\bar{P}}{dX} = 4 \sqrt{\frac{2W'}{\pi}} \frac{\bar{\tau}_L}{H}$
4	$\frac{d\bar{P}}{dX} = -4 \sqrt{\frac{2W'}{\pi}} \frac{\bar{\tau}_L}{H}$

5.1.4 Solution Algorithm

Equations (5.14)-(5.17) present certain difficulties when a numerical solution is attempted. Due to the exponential viscosity-pressure relation (5.7), the coefficient ξ varies several orders of magnitude over the computational domain. In the inlet region, $\xi \gg 1$ since $\bar{\eta}$ is small and H^3 is large. On the other hand, the Hertzian region is characterized by $\xi \ll 1$ since $\bar{\eta}$ is very large and H^3 is small. The mathematical behavior of Equation (5.9) changes drastically for different values of ξ which makes it difficult to design a stable relaxation scheme for line contact problem that works effectively for all range of loads acting at the interface. To tackle this problem, a novel numerical scheme was designed in [72, 73] which is stable for a large range of contact loads. This method uses a hybrid relaxation approach that combines Gauss-Seidel relaxation which works well on large ξ values with Jacobi distributive relaxation which works well with small ξ .

Figure 61 depicts the typical loads acting at the cam-piston line contact interface of the reference radial piston pump. For pump operating conditions ranging from 700-2500 bar outlet pressures and shafts speeds of 1200-1800 rpm, the contact loads (Hertzian pressure) range from 0.1-0.6 GPa. In this particular range of contact loads, the one point Gauss-Seidel relaxation scheme is stable for achieving convergence. An accurate solution of the EHL problem requires both the pressure distribution ($P(X)$) and the minimum gap height parameter (H_0) to converge. This is achieved by performing several Gauss-Seidel relaxations for pressure followed by a single relaxation of the force balance equation to update the value of H_0 ,

$$\bar{P}_i^{n+1} = \omega_{gs} \bar{P}_i^{n+1} + (1 - \omega_{gs}) \bar{P}_i^n \quad (5.23)$$

$$H_0^{n+1} = H_0^n + \omega_{H0} \left(\frac{\pi}{2} - \Delta X \sum_{j=1}^{n-1} \frac{\bar{P}_j + \bar{P}_{j+1}}{2} \right) \quad (5.24)$$

where ω_{gs} represents the under-relaxation parameter used for iterations for pressure solution whereas ω_{H0} represents the under-relaxation parameter for H_0 .

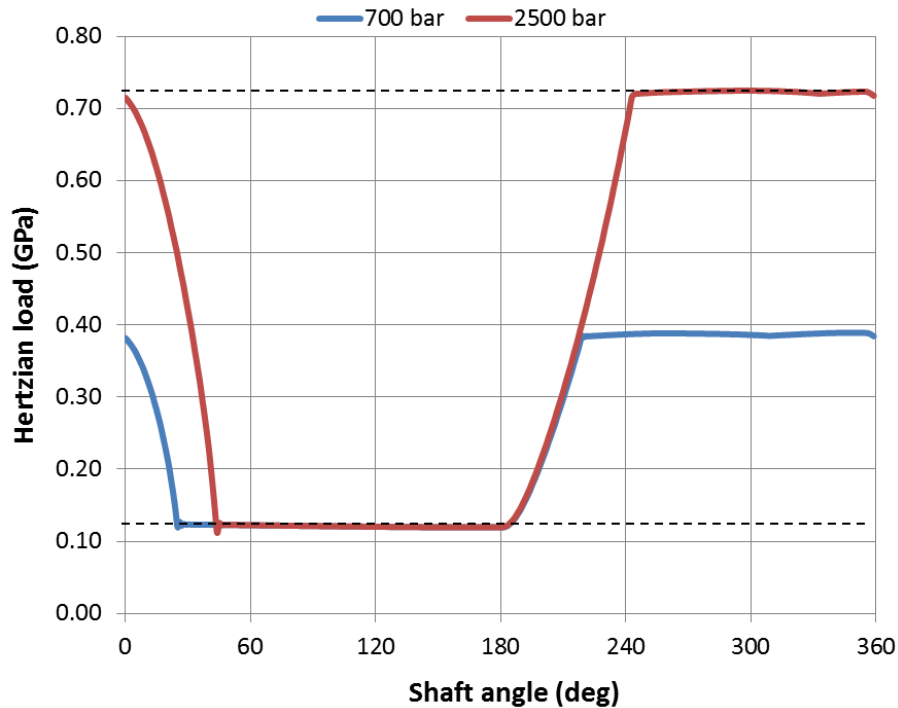


Figure 61: Range of contact loads between cam and piston at Outlet pressures: 700-2500 bar, Shaft speeds: 1200-1800 rpm.

Figure 62 represents the flowchart for the numerical algorithm employed to obtain a converged solution for the EHL problem. The solution process is similar to the one used for FSI analysis of piston-cylinder interface as described in detail in section 4.5. There are two iterative loops which form the integral part of the complete numerical procedure,

- Solution for pressure-deformation coupling of cylinder and plane surface
- Solution for force-balance condition based on pressure generation in the interface.

The simulation process starts by estimating initial values for $\bar{P}(X)$ and H_0 . For the estimated configuration of the two surfaces, the Reynolds equation for pressure distribution is solved using a Newtonian formulation as described in Equation (5.9). Using the intermediate pressure distribution, the shear stress acting on both the contacting surfaces are evaluated and the pressure values are modified by solving a non-Newtonian formulation as described in Table 5. Based on the pressure distribution obtained in each iteration, the elastic deformation of the surfaces is solved which gives the change in surface gap heights. The new gap film thickness values are used to update the pressure

field and these iterations run until both the fluid pressure and solid deformation values reach convergence. This is followed by checking if the load supported by pressure field is sufficient to bear the contact loads acting at the interface and H_0 is changed accordingly. Finally, the calculations are stopped if the force-balance condition is satisfied.

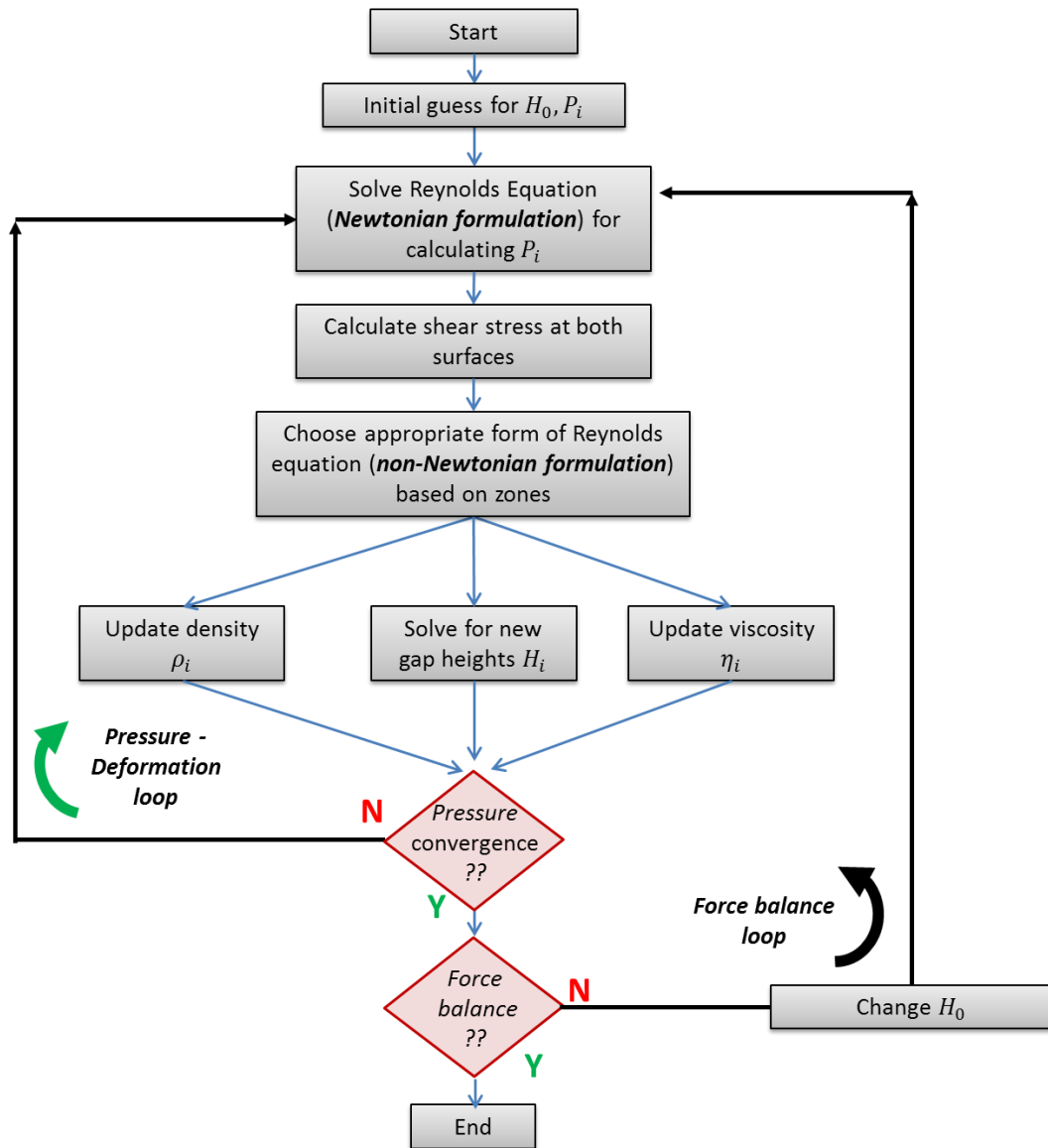


Figure 62: Solution algorithm flowchart for EHL line contact problem.

5.1.5 Prediction of Traction/friction Forces in EHL Contact

The solution algorithm for the EHL described in the previous section is capable of generating converged values for pressure distribution and film thickness in the lubricating domain. Using these results, the traction/friction forces acting between the surfaces can be easily calculated. The shear stress acting on the lower surface (representative of the piston surface) is defined as,

$$\tau(x) = - \underbrace{\frac{h(x)}{2} \frac{dp}{dx}}_{\text{rolling}} + \underbrace{\eta(x) \frac{(u_1 - u_2)}{h(x)}}_{\text{sliding}} \quad (5.25)$$

As shown in above equation, the first term represents the shear stress generated due to rolling component associated with surface velocities while the second term is representative of shear stress due to sliding velocities of surfaces. The net friction force can be obtained by integrating the shear stress along the length of contact region. Dividing the traction force by the normal load acting at the interface provides the friction coefficient,

$$\mu = \frac{\int_{x_{min}}^{x_{max}} \tau dx}{w'_z} \quad (5.26)$$

5.1.6 Potentials of the EHL Model

In this section, results from the EHL model developed in this study are presented for sample input parameters for contact loads, relative velocities and material parameters. The model is versatile and can be used as an effective tool for evaluating the friction forces acting in the interface, local stresses generated at the interface and also the associated power losses. Figure 63 shows the pressure generated in a typical line EHL contact for sample input parameters along with the variation in gap height along the contact length. It can be observed that the lubricant pressure increases steadily from the inlet zone towards the central contact region and rises abruptly to a high value near the outlet region before it drops to ambient pressure again at the exit. Presence of steep pressure gradients near the outlet region in the EHL conjunction would otherwise increase the flow rate and lead to flow continuity problems. Hence, a gap closing and an

abrupt rise in pressure occurs near the outlet referred to as the “pressure spike”. The numerical approach adopted in this study is capable of capturing the pressure spike for a wide range of operating conditions.

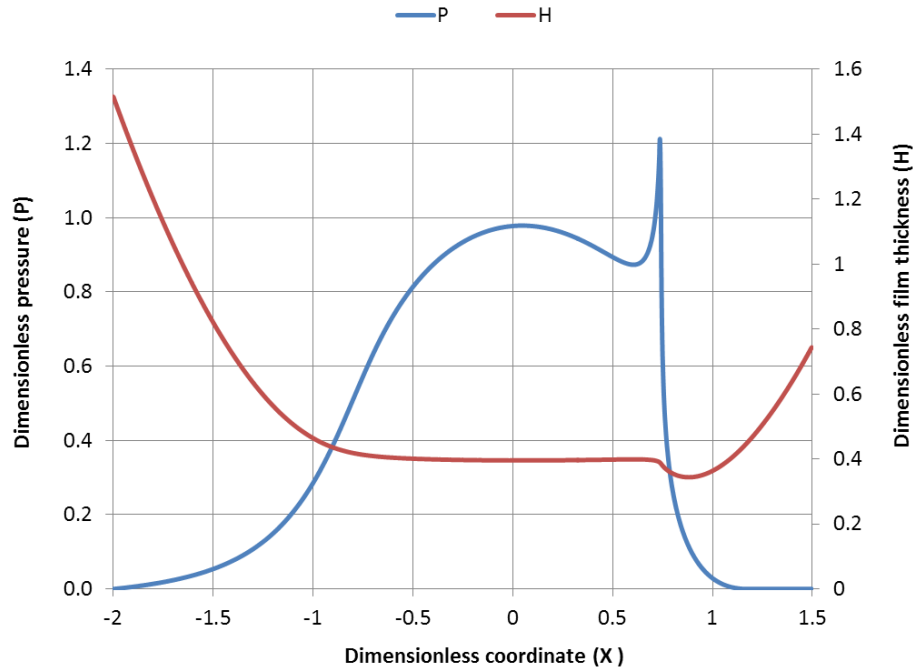


Figure 63: Pressure field and film thickness (dimensionless) in a typical line EHL contact. Input parameters: $W' = 1.3 \times 10^{-4}$, $U_e = 1.0 \times 10^{-11}$, $SRR = 0$, $G = 5007$.

Figure 64 shows the corresponding fluid viscosity variation in the EHL contact for same operating parameters. It is important to note that the viscosity of the lubricant increases by $\approx 10^4$ times as the lubricant flows from the inlet towards the contact region. Near the pressure spike region, the viscosity also experiences an abrupt rise in value before the fluid reaches the outlet. The EHL model developed is capable of simulating a wide range of input parameters corresponding to loads, entrainment speeds. Figure 65 shows the change in the pressure field in the EHL contact at different entrainment speeds. An increase in entrainment speed parameter U_e leads to an increased pressure generation in the contact region as can be seen through the figure. Also, the load carrying ability of the film increases which is governed by the area under the curve.

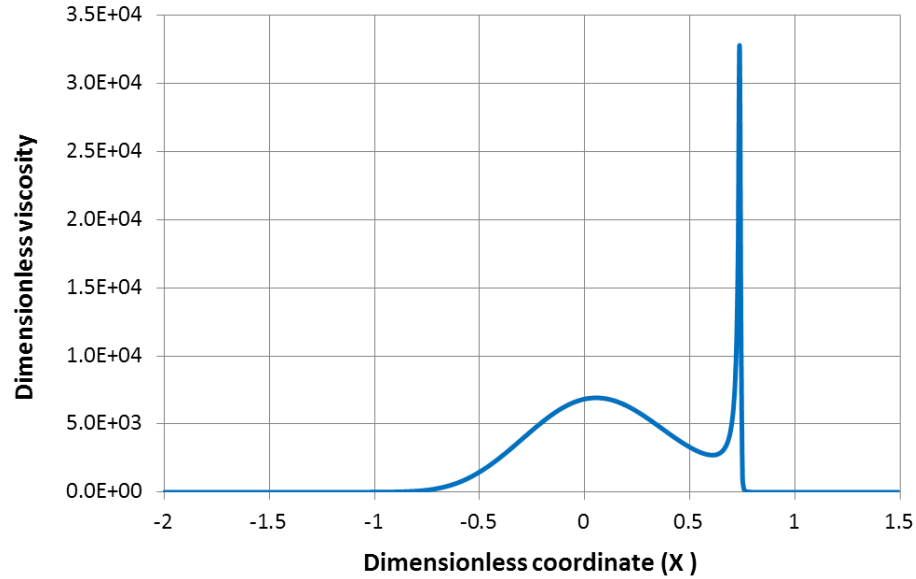


Figure 64: Fluid viscosity variation in a typical line EHL contact. Input parameters: $W' = 1.3 \times 10^{-4}$, $U_e = 1.0 \times 10^{-11}$, $SRR = 0$, $G = 5007$.

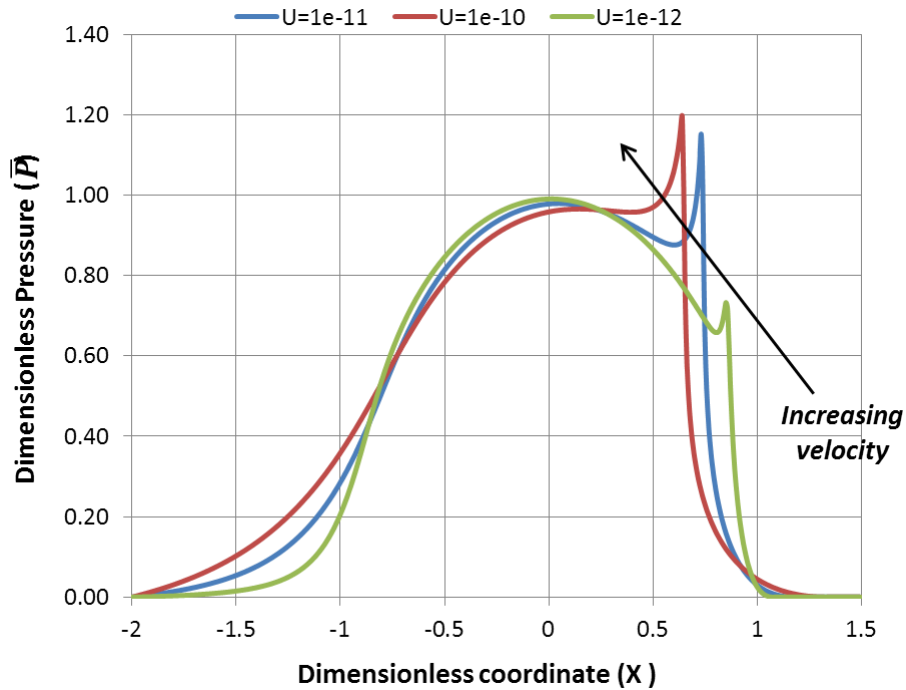


Figure 65: Dependence of pressure field on varying velocity parameter (U_e). $W' = 1.3 \times 10^{-4}$, $SRR = 0$, $G = 5007$.

The results depicted above are based on $SRR = 0$ assuming no sliding velocity. Results at varying slide-roll ratios will be presented now. Figure 66 shows the friction coefficient

at different loads (W') and slide-roll ratios (SRR) using the Newtonian model. It can be seen from the figure that the correlation between the friction coefficient and slide-roll ratio is almost linear and at high values of SRR , the Newtonian model would result in significant over-prediction of the friction coefficient values.

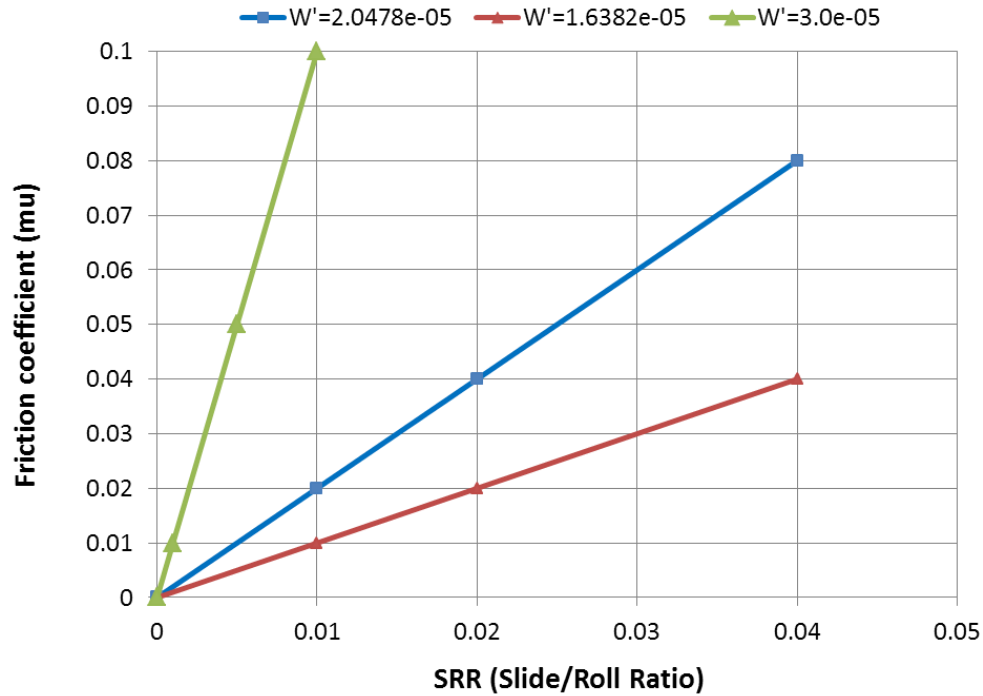


Figure 66: Friction coefficient using the Newtonian model. $U_e = 1.0 \times 10^{-11}$, $SRR = 0$, $G = 5007$.

Figure 67 shows a comparison between the friction coefficient values as calculated using the Newtonian and non-Newtonian models separately. Using the non-Newtonian model, the friction coefficient reaches a limiting value and at higher slide-roll ratios, the values predicted are more realistic. All the results depicted for the EHL model are found to match closely with literature [71].

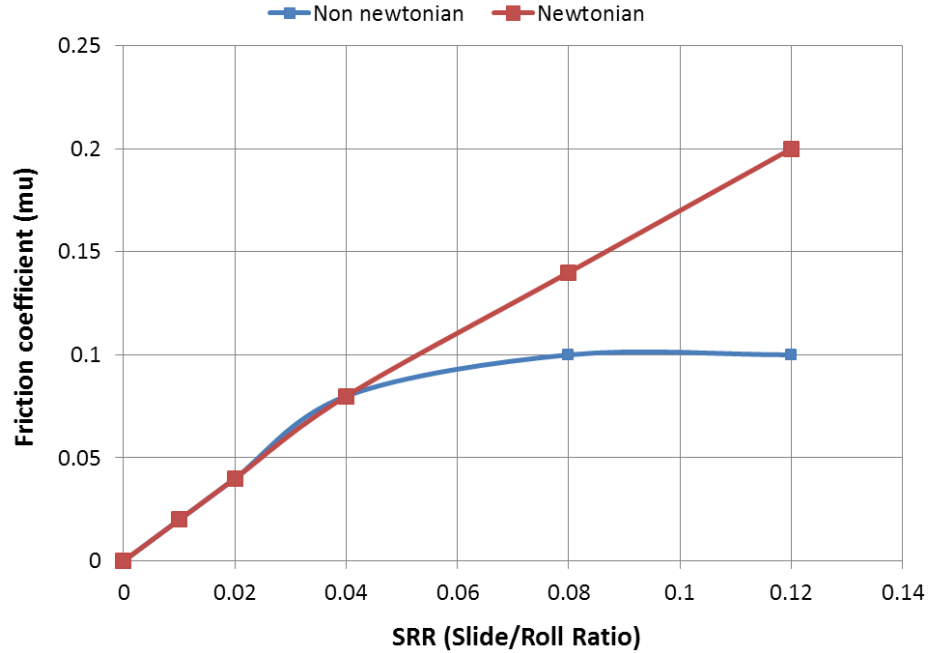


Figure 67: Comparison of friction coefficient as obtained using the Newtonian and non-Newtonian fluid model. $W' = 2.0478 \times 10^{-5}$, $U_e = 1.0 \times 10^{-11}$, $G = 5007$.

5.2 Application of EHL Model to Reference Pump Geometry

The previous section details out the simulation results obtained using a wide range of input parameters. Hence, the EHL friction model can be used as a generic tool to generate instantaneous friction values in the operating cycle in the radial piston pumps. However, to obtain the accurate values of friction at each instant, correct input parameters (W' , U_e , SRR) need to be determined for the actual pump design in operation. As shown in Figure 61, evaluation of contact loads follows directly from the force-balance equation for the piston. However, to evaluate the actual surface velocities (u_1 , u_2) at each time instant during cam rotation, a detailed analysis of the cam-piston kinematics has to be performed and analytical/numerical models need to be formulated. One of the easiest methods to generate the accurate values of surface velocities is to experimentally measure the same for large range of operating conditions and formulate curve fit data which can be used in conjunction with friction model.

This section presents a sensitivity analysis for various cam-piston kinematic assumptions. An attempt is made to investigate how the EHL friction model responds to different

situations before the actual kinematic parameters (mainly surface velocities) governing cam-piston motion can be determined. To consider many possible alternatives, different configurations for cam-piston interface are analyzed in order to make a realistic prediction of motion parameters required as inputs to the friction model.

5.2.1 Cam-piston Interface with Direct Cam-piston Contact

To analyze the basic configuration of the cam-piston interface when no additional components are present to reduce relative motion or facilitate hydrodynamic lubrication, a direct contact between cam-piston is analyzed to study the variation of friction coefficient during an operating cycle of pump. The presence of rolling element bearings in the reference design is neglected here. Figure 68 shows the contact interface between the piston and eccentric-cam under such conditions.

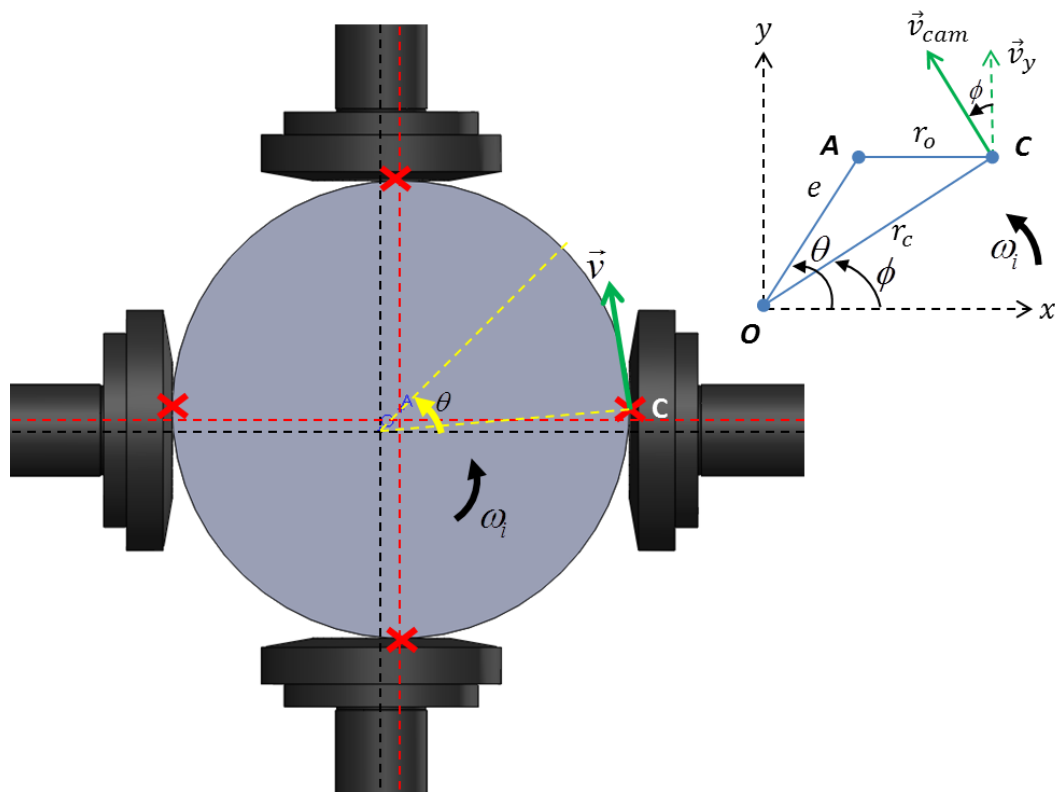


Figure 68: Cam-piston interface with direct cam-piston contact. Resolution of velocity at contact point is shown on top right.

Using geometrical relations, the instantaneous surface velocities of cam and piston (u_1, u_2) at the contact point with respect to a stationary frame (O) can be defined as,

$$u_1 = v_y = v_{cam} \cos \phi = r_c \omega_i \cos \phi \quad (5.27)$$

$$u_2 = 0, u_c = \frac{dy_c}{dt} = e \omega_i \cos \theta \quad (5.28)$$

$$SRR = \frac{u_s}{2u_e} \quad (5.29)$$

where u_c the velocity of the contact point as it changes with shaft angle.

Using the definitions in Equations (5.11)-(5.13), the velocity parameters associated with the EHL contact can be evaluated,

$$u_e = \left(\frac{r_o \omega_i - e \omega_i \cos \theta}{2} \right) \quad (5.30)$$

$$u_s = |r_o \omega_i + e \omega_i \cos \theta| \quad (5.31)$$

$$SRR = \frac{u_s}{2u_e} \quad (5.32)$$

With the velocity parameters and contact loads calculated, all the parameters required as inputs to the friction model can be generated. The input parameters for pump operating condition of 700 bar outlet pressure and 1800 rpm shaft speed are shown in Figure 69. Simulations were run for each instant in pump cycle using the EHL model in order to obtain instantaneous friction values. The results obtained are shown in Figure 70. It can be seen from the results that there is a significant variation in friction coefficient (viscous friction in EHL) during a pump cycle. However, extremely low film thickness values ($< 0.05 \mu m$) are obtained through simulation results which indicates that there is a significant asperity contact between the surfaces.

An accurate modeling of friction at such operating conditions would require an investigation into the mixed friction modeling of the contact interface and coefficient of asperity contact friction will need to be added to the viscous friction coefficient. Nevertheless, the EHL model developed in this study was successful in predicting the

contact conditions that exist when the pump is operated with a direct cam-piston contact under lubricating conditions. The viscous friction values evaluated using the EHL model at instants when film thickness values $> 0.1 \mu\text{m}$ can be considered accurate. It can be concluded from the present set of results that a direct cam-piston contact is insufficient to lubricate the cam-piston interface and the surfaces will undergo wear in continued operation. Also, by including the effect of asperity contact, the results using this kinematic assumption would correspond to a situation where the friction coefficient is constant for different shaft angles ($\mu \approx 0.1$) which was discussed in CHAPTER 4.

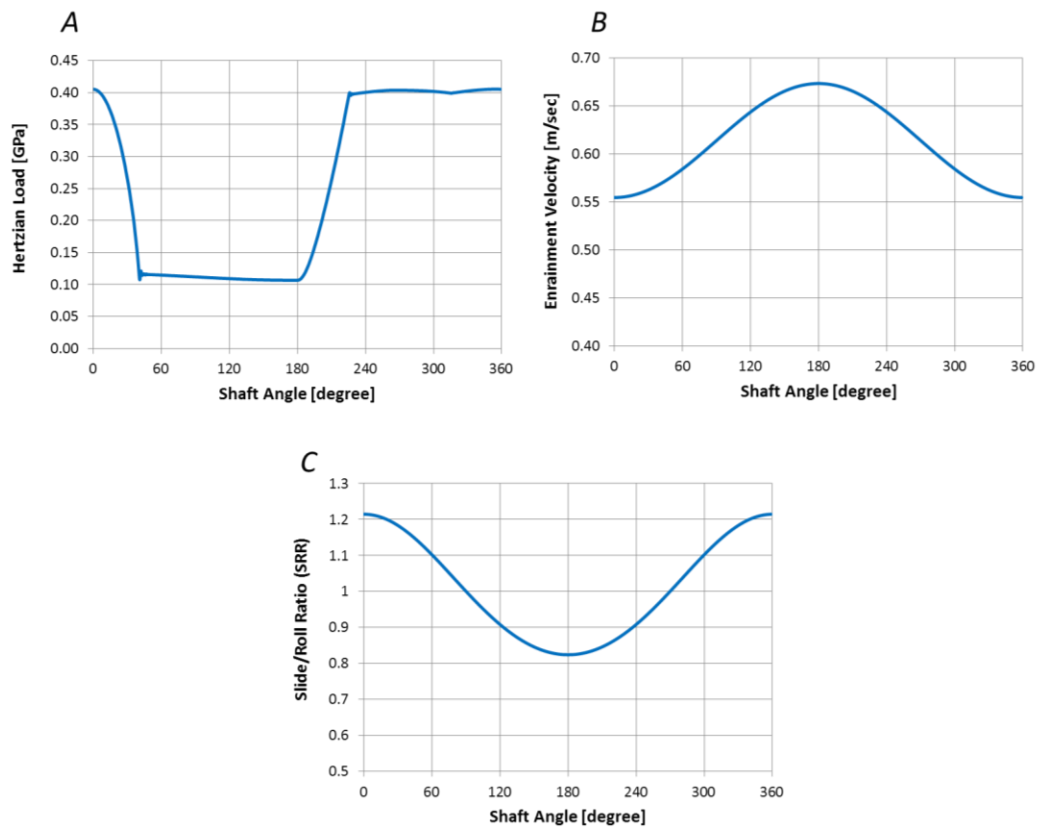


Figure 69: Input parameters for EHL friction model for *Pump outlet pressure: 700 bar*, *Shaft speed = 1800 rpm*. (A) Contact load in terms of Hertzian pressures. (B) Entrainment speed of lubricant. (C) Slide-roll ratio.

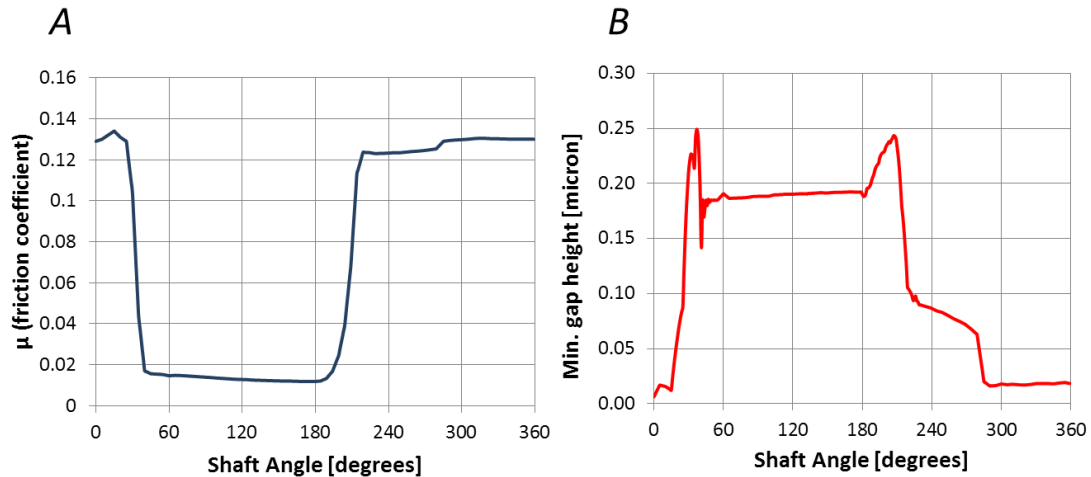


Figure 70: Results from friction model for *Pump outlet pressure: 700 bar, Shaft speed = 1800 rpm*. (A) Friction coefficient variation with shaft angle. (B) Minimum film thickness with varying shaft angle.

5.2.2 Cam-piston Interface with Rolling Element Bearing and Outer Race

Figure 71 shows the geometry of the cam-piston contact in the reference pump design. It was observed that a direct cam-piston contact results in high sliding velocities and low values of film thicknesses that would imply high wear for prolonged pump operation. Hence, a modified design with rolling element bearings present between the inner eccentric shaft and a freely rotating outer race serves to reduce the relative motion between the surfaces. Precise values of surface velocities in such an arrangement are dependent on the friction forces acting between the rolling element bearings and inner/outer races. Also, since the outer race is free to rotate about its center, its angular velocity is dependent on the friction acting exerted by the piston thereby making the dynamic model coupled with the friction model. Development of such a detailed model would require modeling of dynamics of each rolling element along with race and cage interactions and is out of scope of this study. However, such bearing models do exist in tribology literature [74, 75] and can be utilized in conjunction with the friction model to obtain a precise numerical calculation of surface velocities and friction at the contact interface.

In this study, a simplified approach is taken by assuming that the contact between the outer race and piston with the highest instantaneous load undergoes pure rolling at each time instant. Using such an assumption, the instantaneous angular velocity of the outer race can be easily determined. Moreover, making this assumption is justified from practical observations since only a rolling contact can ensure continuous operation of the pump without wear in moving surfaces.

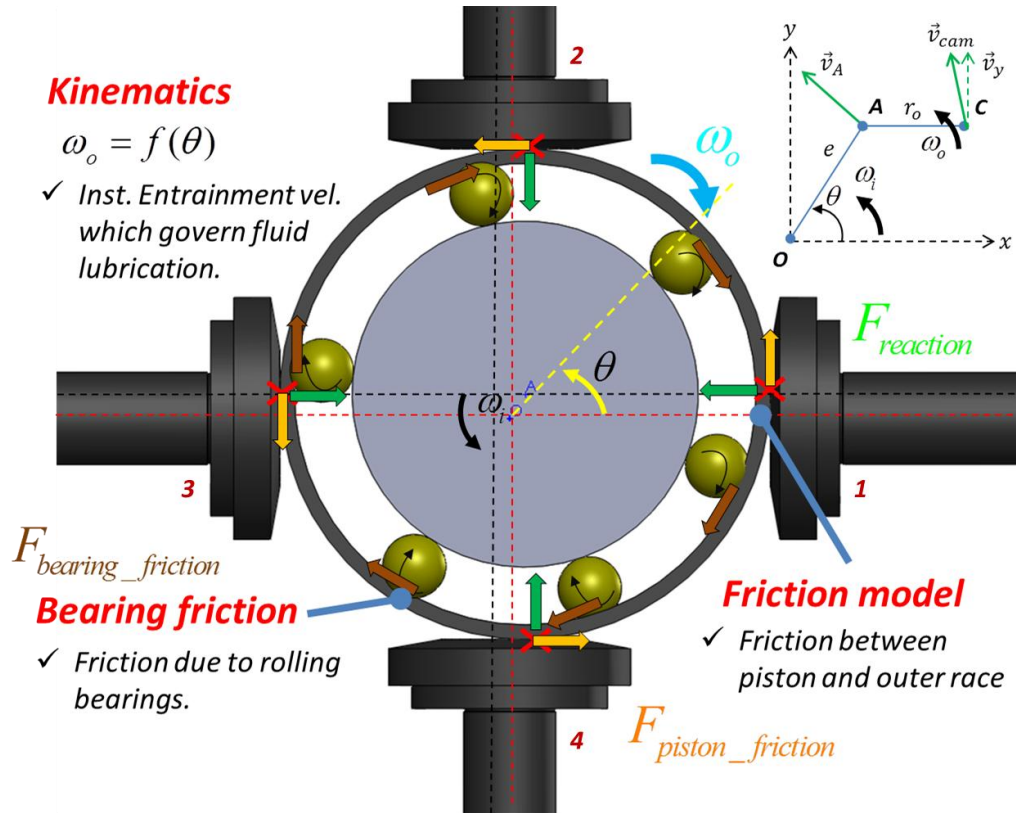


Figure 71: Cam-piston interface with rolling element bearings and outer race.

The equations governing the velocity parameters have to be modified for the present geometry since the outer race only oscillates about the rotating point and is free to rotate about its geometric center ($\vec{v}_{cam} = \vec{v}_A + \vec{\omega} \times \vec{r}_o$). For the geometry shown in Figure 71, the velocity parameters can be defined as,

$$u_e = \left(\frac{r_o \omega_o - e \omega_i \cos \theta}{2} \right) \quad (5.33)$$

$$u_s = |r_o \omega_o + e \omega_i \cos \theta| \quad (5.34)$$

$$SRR = \frac{u_s}{2u_e} \quad (5.35)$$

The only unknown in the above set of equations is the angular velocity of outer race ω_o . Using the assumption of pure rolling at highest loaded piston, ω_o can be calculated by setting the net velocity at the contact point of highest loaded piston to zero at each instant,

$$u_1 = e \omega_i \cos \theta + r_o \omega_o = 0 \quad (5.36)$$

which gives,

$$\omega_o = -\frac{e \omega_i \cos \theta}{r_o} \quad (5.37)$$

where $\theta \rightarrow \theta$ when highest loaded piston is piston 1, $\theta \rightarrow \theta - 90^\circ$ for piston 2, $\theta \rightarrow \theta - 180^\circ$ for piston 3 and $\theta \rightarrow \theta - 270^\circ$ for piston 4.

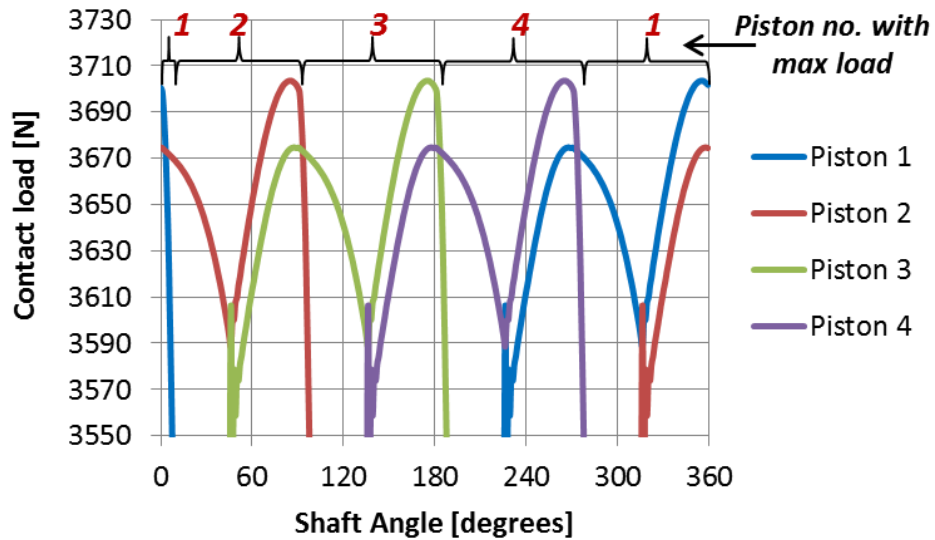


Figure 72: Instantaneous contact loads on each piston with maximum loaded piston shown for each shaft angle. *Pump outlet pressure: 700 bar, Shaft speed = 1800 rpm.*

It can be seen through Figure 72 how the piston with maximum load was chosen based on the instantaneous loads for each of the 4 pistons. Figure 73 shows the input parameters obtained by using the described assumption for outer race kinematics. The values of slide-roll ratio obtained were extremely low ($SRR \approx 0.0$) since the assumption of pure

rolling removes the sliding components associated with the surface velocities. Also, the simulation results predict low entrainment speeds throughout the pump cycle. Using this set of input parameters, it was found that the pressure field and friction coefficient do not vary significantly with shaft angle. Hence, simulations were run only for a small set of shaft angles rather than every instant of pump cycle. Figure 74 shows the typical simulation result which is representative of the pressure field at different shaft angles in a pump cycle. Table 6 shows the output parameters for the same simulation results.

The results for this specific cam-piston configuration imply that the friction between the cam and the piston is predominantly governed by rolling friction and sliding component associated with surface velocities is much smaller. At such low relative speeds between the surfaces, the EHL friction model is unable to predict a significant pressure generation in the fluid film and the stress distribution obtained is almost close to a Hertzian contact between solid surfaces. The viscous friction component acting on the interface is negligible and friction behavior is governed by the asperity contact between solid surfaces. However, the friction forces acting during such conditions are expected to be much smaller than previous cases ($\mu \approx 0.001$) and hence the pump can function smoothly over a wide range of operating conditions owing to minimal relative motion between the cam and piston. This hypothesis agrees well with the practical observations where the reference pump design can function effectively up to rated pressures of 700 bar.

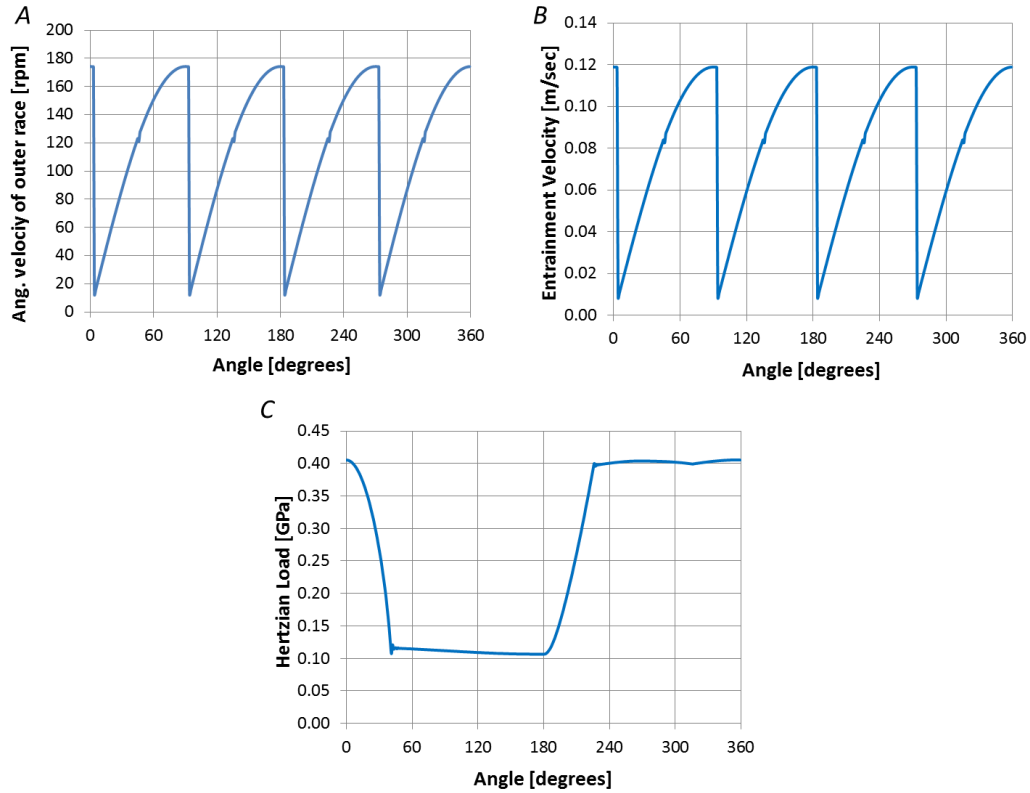


Figure 73: Input parameters for EHL friction model for *Pump outlet pressure: 700 bar*, *Shaft speed = 1800 rpm*. (A) Angular velocity of outer race (B) Entrainment speed of lubricant. (C) Contact load in terms of Hertzian pressures.

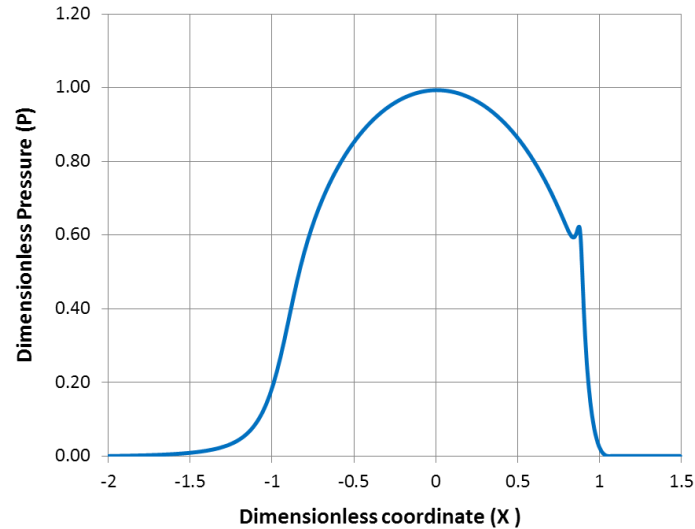


Figure 74: Results from friction model for $\theta = 0^\circ$. Input parameters: $W' = 1.97 \times 10^{-5}$, $U_e = 4.66 \times 10^{-13}$, $SRR = 0$ *Pump outlet pressure: 700 bar*, *Shaft speed = 1800 rpm*.

Table 6: Output parameters for the operating condition shown in Figure 74.

Film thickness (μm)	0.07
Friction coefficient	$\approx 1 \times 10^{-5}$

5.3 Results from the Fully Coupled Pump Model

This section discusses the results obtained when the cam-piston EHL friction model is coupled with the lubricating gap model for piston-cylinder interface. As explained earlier, all results depicted in CHAPTER 4 were based on constant friction assumption between the piston and cam which was representative of pure sliding condition ($\mu = 0.1$). Using the cam-piston EHL model as a generic tool, the dynamic models described in previous section (direct cam-piston contact, rolling element bearing) are analyzed individually and separate set of results are generated for piston-cylinder lubricating gap. The results for each of these cam-piston configurations are discussed now,

5.3.1 Results for Direct Cam-piston Contact

The kinematic details of this cam-piston design have been explained in 5.2.1. Using the input parameters as shown in Figure 68, simulations were run for piston-cylinder interface at pump outlet pressure of 700 bar and 1800 rpm shaft speed. Figure 75 and Figure 76 show the pressure distribution in the piston-cylinder lubricating gap domain along with film thicknesses.

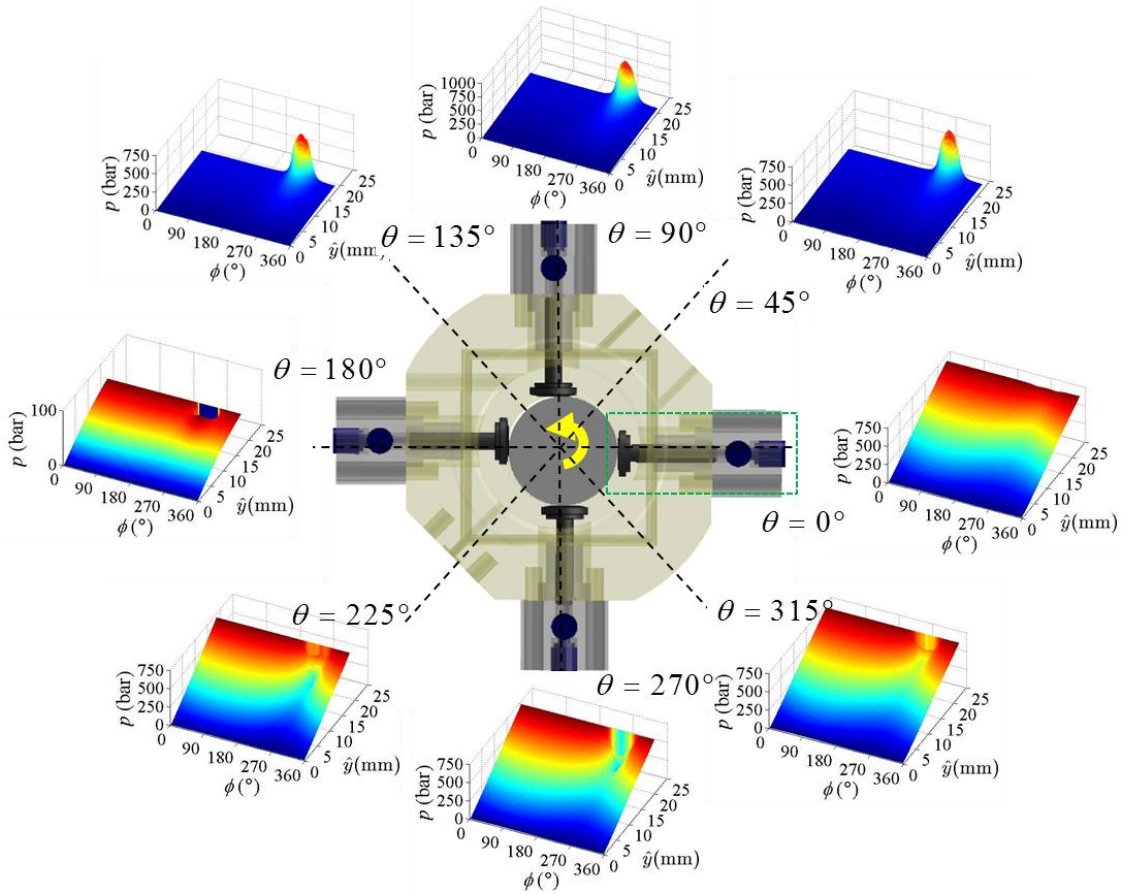


Figure 75: Instantaneous pressure field in lubricating gap domain over one shaft revolution for direct contact type cam-piston interface. *Operating condition: Outlet pressure=700 bar, Shaft speed=1800 rpm.*

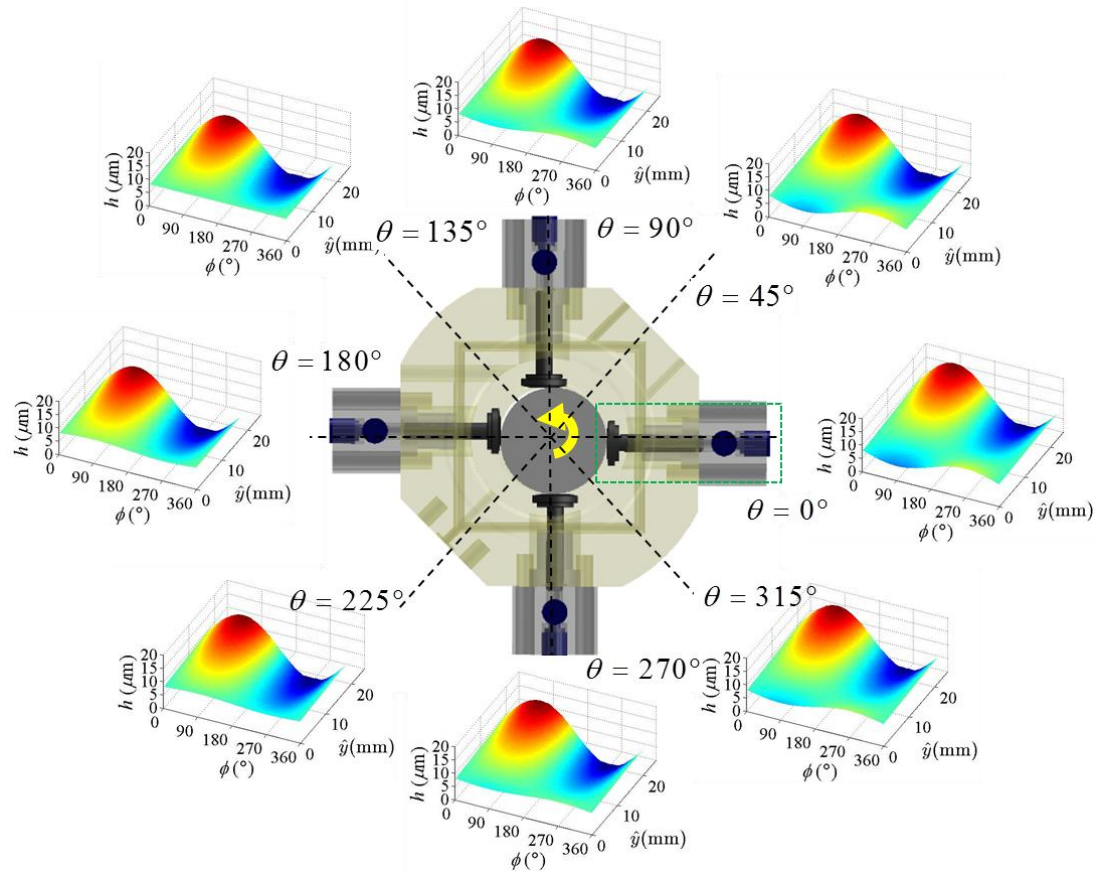


Figure 76: Instantaneous film thicknesses in lubricating gap domain over one shaft revolution for direct contact type cam-piston interface. *Operating condition: Outlet pressure=700 bar, Shaft speed=1800 rpm.*

5.3.2 Results for Rolling Element Bearing type Interface

A detailed analysis of the cam-piston contact with rolling element bearings, as done in 5.2.2, resulted in the conclusion that an accurate calculation of velocity parameters requires experimental measurements or development of a coupled numerical model for the complete bearing system which is complicated. In this section, results will be presented for the simplified case which assumes that there is an instantaneous pure rolling contact between the outer race and the piston with highest load. The input parameters corresponding to this condition were shown in Figure 73 and it was concluded from the simulation results the rolling friction coefficient for steel-steel interface can be

assumed for the entire pump cycle. Figure 77 and Figure 78 shows the pressure field and film thickness distribution in the piston-cylinder gap domain.

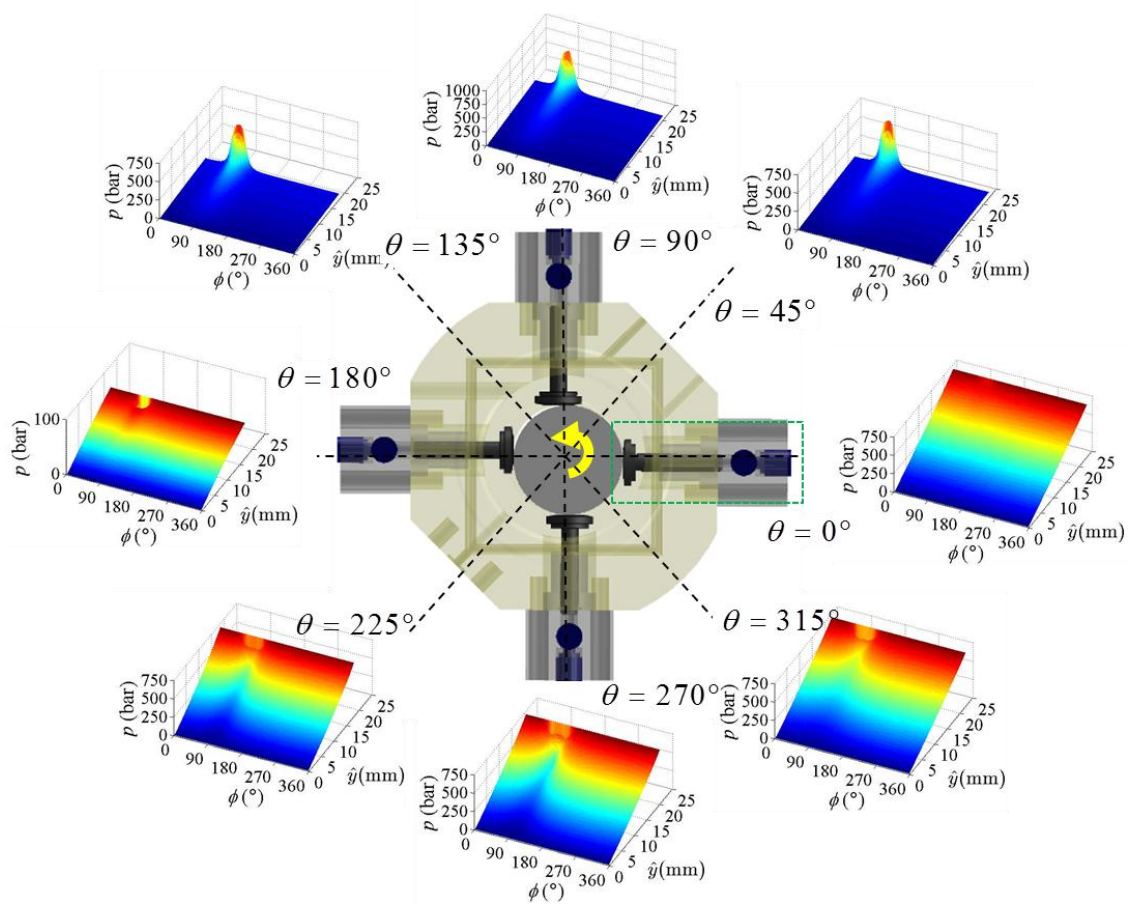


Figure 77: Instantaneous pressure field in lubricating gap domain over one shaft revolution when pure rolling is assumed in the rolling element bearing type cam-piston interface. Operating condition: Outlet pressure=700 bar, Shaft speed=1800 rpm.

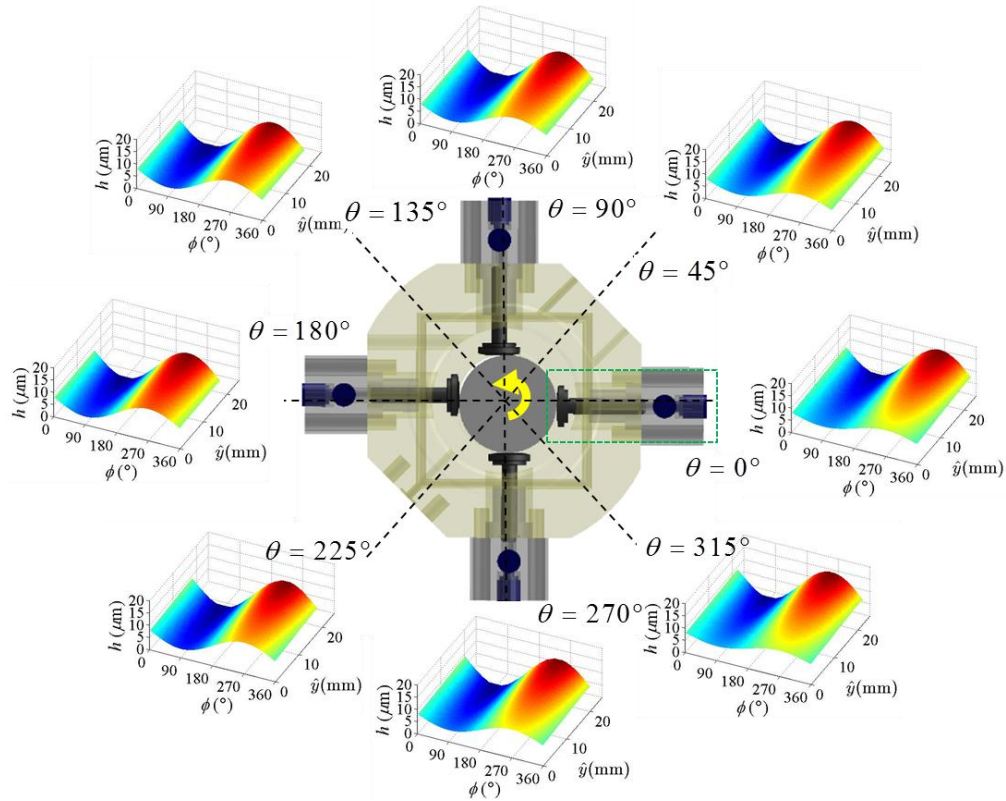


Figure 78: Instantaneous film thicknesses in lubricating gap domain over one shaft revolution when pure rolling is assumed in the rolling element bearing type cam-piston interface. *Operating condition: Outlet pressure=700 bar, Shaft speed=1800 rpm.*

5.3.3 Result Comparison for Different Cam-piston Configurations

The pressure field and gap height distribution as shown in the previous sections do not show a significant difference between the results obtained when friction values corresponding to different cam-piston configurations were used. This is because solid-solid contact is observed over a larger part of pump cycle for both configurations due to which the performance parameters obtained are almost similar. However, the magnitude and location of solid contact region varies in both cases which need to be analyzed in detail. Figure 79 shows a comparison between the piston eccentricities obtained for rolling and direct contact conditions which highlights the difference in contact locations.

As shown in section 4.4, the radial micro-motion of the piston is caused by two important factors – the friction forces exerted by cam surface and the moment generated (by normal reaction force) due to motion of the contact point between the cam and piston.

Though the instantaneous contact moments remain same in both situations, the friction forces change significantly (refer sections 5.3.1, 5.3.2) leading to a change in the resultant tilting moment acting on the piston as shown in Figure 80.

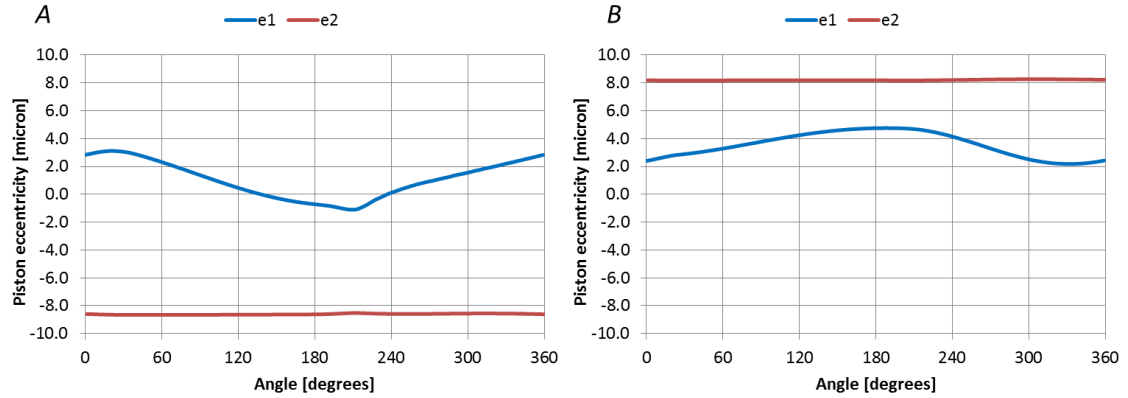


Figure 79: Piston eccentricities over one shaft revolution. (A) Direct cam-piston contact (B) Pure-rolling contact.

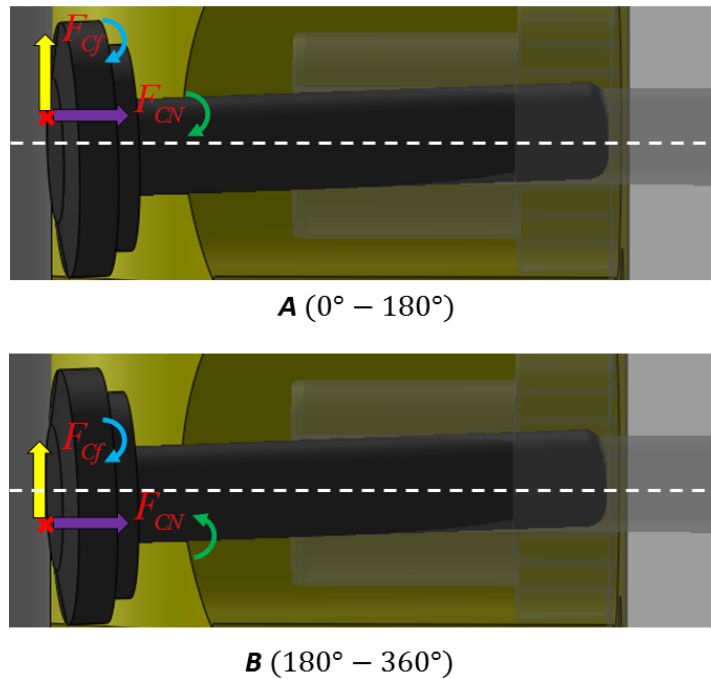


Figure 80: Side loads/moments acting on piston. F_{cf} : friction force, F_{CN} : normal contact force.

In direct cam-piston contact, the friction coefficients obtained ($\approx 0.02 - 0.12$) are much higher than the pure rolling case (≈ 0.001). Hence, in the latter half of the cycle ($0^\circ -$

180°), when contact forces are larger due to high displacement chamber pressures, the frictional moment dominates the moment generated by normal force which cause the piston to tilt in clockwise direction. In pure rolling case, the frictional moment is always negligible compared to that generated by normal force which causes the piston to tilt in clockwise direction when normal forces are high (0° – 180°).

The ϵ_{el} field (representative of solid penetration) obtained through simulation results are plotted for both configurations in Figure 81 and Figure 82. The different locations of solid-solid contact region are observed and the contact stresses vary since the side loads acting on the piston are different. The contact stresses in direct cam piston contact are found to be higher than the pure rolling case.

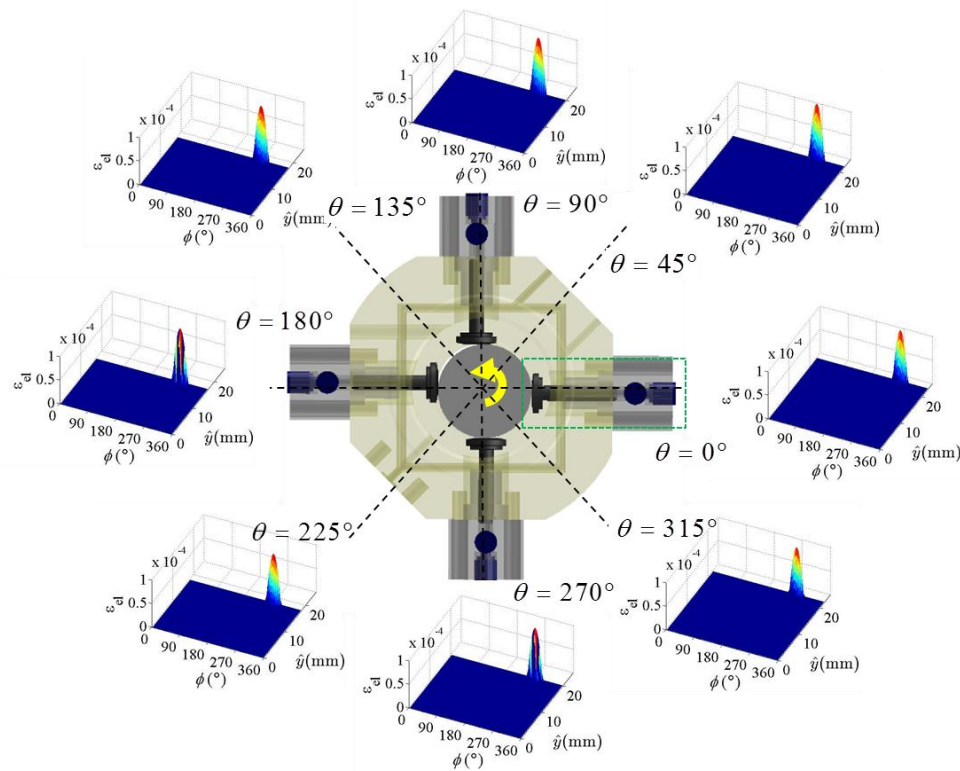


Figure 81: ϵ_{el} field in piston-cylinder lubricating gap domain over one shaft revolution for direct cam-piston contact type interface. *Operating condition: Outlet pressure=700 bar, Shaft speed=1800 rpm.*

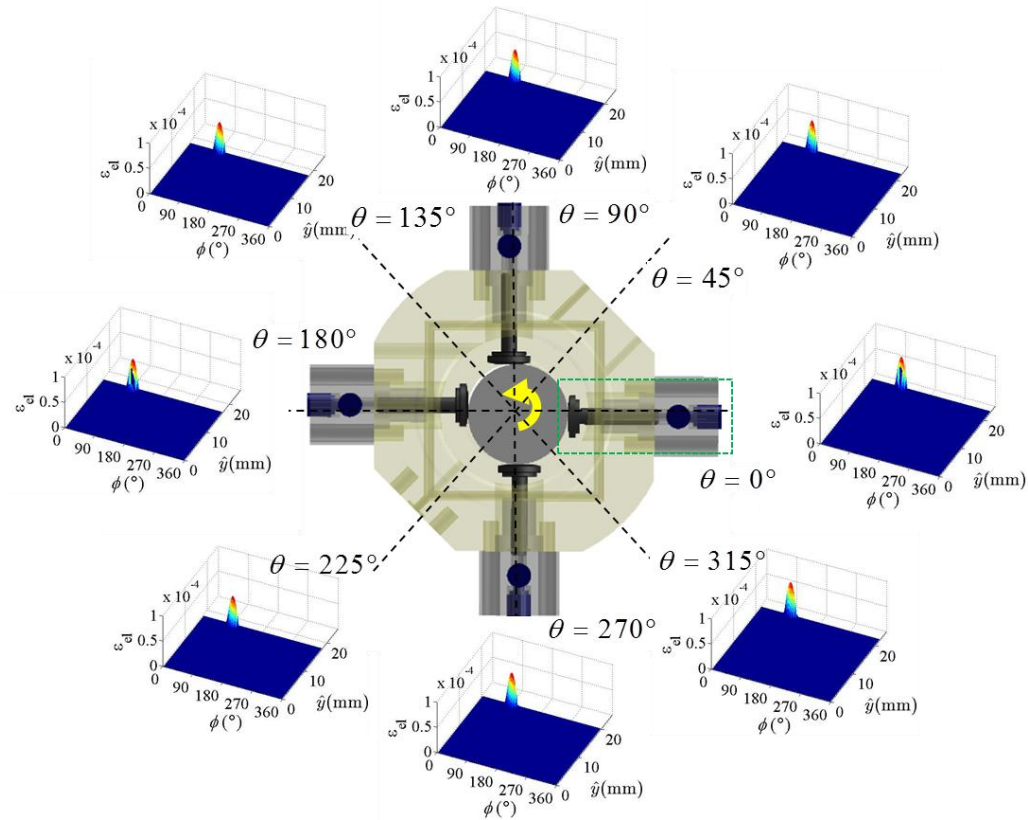


Figure 82: ϵ_{el} field in piston-cylinder lubricating gap domain over one shaft revolution for pure rolling cam-piston contact. *Operating condition: Outlet pressure=700 bar, Shaft speed=1800 rpm.*

5.3.4 Design Directions for Reference Pump using the Developed EHL Model

This study demonstrates the versatility of the EHL friction model by showing the detailed results obtained when different kinematic assumptions are used. The simulation results did not show significant change in performance parameters of the pump when friction forces were varied by changing the cam-piston design configurations. This is because piston-cylinder solid contact was always observed for the three different kinematic/friction force assumptions employed in the study – a constant sliding coefficient of friction, a variable friction coefficient using direct cam-piston contact and a pure rolling contact. Based on the simulation results, the following inferences can be drawn regarding design modifications for reference pump,

1. Since both cam-piston kinematic assumptions lead to prediction of a significant solid contact between piston and cylinder in the reference design experimental

measurement of surface velocities is the first step to obtain a clear idea of the instantaneous velocity parameter and direction of friction force which are critical parameters required for EHL friction model.

2. From Figure 73, it can be seen that the rotational velocity of outer race has large discontinuities if the pure rolling condition has to be satisfied at each instant at the highest loaded piston. This hints at the fact that the friction force might change direction in actual pump operation depending upon the loads, the bearing friction and other bearing parameters that have an impact on the cam-piston kinematics. An example of a theoretical condition which was analyzed in the study is the case where the friction force changes direction with the velocity of contact point displacement i.e. friction force acts upward for $0^\circ < \theta < 90^\circ$, $270^\circ < \theta < 360^\circ$ and downwards for other shaft angles. Also, friction coefficient is assumed to be constant and representative of pure sliding condition similar to the analysis presented in 4.6. Simulation results for this theoretical case are shown in Figure 83, Figure 84. It is observed that a changing friction direction with pure sliding predicts solid contact only for a small duration of pump cycle ($\approx 240^\circ - 280^\circ$) wherein ϵ_{el} is found to be much smaller than previous cases. This demonstrates that results can vary significantly depending upon the friction magnitude and direction.
3. To ensure that the cam-piston contact operates in full EHL regime, the developed model can be used to predict the minimum lubricant entrainment velocity (u_e) required for a given range of load parameters.

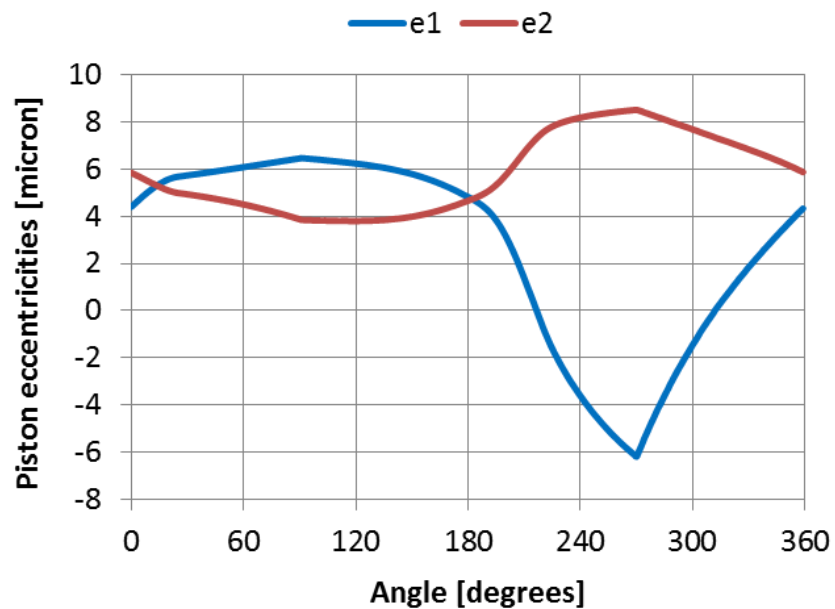


Figure 83: Piston eccentricities over one shaft revolution when friction direction changes.
Operating condition: Outlet pressure=700 bar, Shaft speed=1800 rpm.



Figure 84: ϵ_{el} field in piston-cylinder lubricating gap domain for $\theta = 250^\circ$.

CHAPTER 6. CONCLUSION & FUTURE WORK

The study presented a novel approach for modeling radial piston machines by developing a multi-domain simulation tool that accurately captures the complex physics associated with kinematics, the fluid flow through the main chambers and lubricating gaps and also the power losses occurring in the machine. This was achieved by developing separate modules for modeling each of the mentioned features with a close interaction across each of them in the form of data exchange. A global fluid dynamic model based on lumped parameter approach has been developed that predicts the main flow parameters of the radial piston pumps with sufficient accuracy. This module is versatile and can be easily coupled with a generic hydraulic system to incorporate the effects of other components (pumps, valves) and generate results that are representative of the complete system operation. In particular, the study modeled the reference pump within a hydraulic system which is suitable for operating high pressure hydraulic tools such as bolt tensioner, rock splitters. The system consists of two pumps and a control valve which permit the operation of the radial piston pump only during the high pressure phase of the working cycle. The lumped parameter model is used to generate the necessary boundary conditions for the simulation of the internal lubricating gaps of the unit.

An advanced model was created for a detailed evaluation of flow features in each lubricating gap interface present in the pump: the piston-cylinder interface and the cam-piston interface. A fluid-structure interaction based model was developed for the piston-cylinder interface for operation in the elastohydrodynamic lubrication regime. An isothermal analysis of fluid film was coupled with the calculation of solid bodies' surface deformation. The pressure generation in fluid film is solved using the Reynolds equation. A finite volume method based solver is developed to numerically solve the Reynolds equation in the complex geometry along with a separate solver to evaluate the

deformation of piston and cylinder surfaces. An efficient and flexible exchange of information is ensured between the two numerical domains through linking of fluid and solid meshes. This model allows a precise analysis of fluid film behavior over one machine shaft revolution by evaluating the micro-motion of the piston by the external time changing load conditions. Detailed results for pressure and gap height fields, together with the leakage flow and power loss were presented for pump outlet pressures ranging from 700-2500 bar. Also, the variation of these parameters with outlet pressure and clearance is demonstrated. These results highlight the potentials of the model for being used as designing tool for these kinds of positive displacement machines.

In order to obtain an accurate prediction of piston micro-motion which has a direct impact on the final results obtained through simulation, it is critical to determine the precise external loads on the piston. One of the key forces that generate radial loads on the reciprocating piston is the friction exerted by the eccentric shaft (cam). An attempt to evaluate a precise instantaneous value of this friction was made in this study by developing a numerical model for line contact EHL that can solve for pressure generation in the lubricant film that squeezes between surfaces. The EHL model incorporates the non-Newtonian fluid behavior that occurs due to a large sliding motion between two surfaces.

Using this model, results for pressure field and friction coefficient were generated by using a wide range of input parameters. However, the generic friction model can be utilized to its true potential for radial piston pump design only if correct input parameters (relative velocities between surfaces, loads, material parameters) are calculated. This would require experimental measurement of surface velocities since development of analytical/numerical to model the complicated dynamics of moving pump parts is tedious and time consuming. When the correct nature of cam-piston kinematics is known, it will be possible to come with better designs of radial piston pumps using the developed simulation tool that can operate without solid-solid contact and at even higher operating pressures.

Nevertheless, the importance of the friction model in determining accurate values of film thickness and piston-cylinder contact was highlighted by presenting coupled results using simplified dynamic models for the rotating cam based on certain assumptions.

The results of this research show that the numerical models developed can form an important base for investigations of fluid flow in radial piston machines and hence the multi-domain simulation tool can be used as an effective tool for designing radial piston pumps. Future developments of the simulation tool might include incorporation of thermal effects in the analysis of lubricating gap flows, experimental validation of the simulation results, development of a detailed model for cam-piston kinematics using experimental measurements and enhancement of friction model by including squeeze effects and mixed friction regime.

LIST OF REFERENCES

LIST OF REFERENCES

- [1] Chappie, P. J. (1992). Modelling of a radial-piston hydraulic motor. Proceedings of the Institution of Mechanical Engineers, Part I: Journal of Systems and Control Engineering, 206(3), 171-180.
- [2] Kleist, A. (1997). Design of Hydrostatic Static Bearing and Sealing Gaps in Hydraulic Machines. In 5th Scandinavian International Conference on Fluid Power, Linköping, Sweden, May (pp. 28-30).
- [3] Kleist, A. (1995). Berechnung von hydrostatischen Dichtstellen in hydraulischen Maschinen. Olhydraulik und Pneumatik, 39(10), 767.
- [4] Mortensen, K. A., Henriksen, K. H., (2011). Efficiency Analysis of a Radial Piston Pump Applied in a 5MW Wind Turbine with Hydraulic Transmission. Master Thesis, Aalborg University, Aalborg, Denmark.
- [5] Johansen, P., Roemer, D. B., Andersen, T. O., & Pedersen, H. C. (2013, October). Multibody Dynamics of a Fluid Power Radial Piston Motor Including Transient Hydrodynamic Pressure Models in Lubricating Gaps. In ASME/BATH 2013 Symposium on Fluid Power and Motion Control (pp. V001T01A039-V001T01A039). American Society of Mechanical Engineers.
- [6] Ehsan, M., Rampen, W. H. S., & Salter, S. H. (2000). Modeling of digital-displacement pump-motors and their application as hydraulic drives for nonuniform loads. Journal of dynamic systems, measurement, and control, 122(1), 210-215.
- [7] Borghi, M., Milani, M., Paltrinieri, F., & Zardin, B. (2005). Pressure transients in external gear pumps and motors meshing volumes (No. 2005-01-3619). SAE Technical Paper.
- [8] Vacca, A., & Guidetti, M. (2011). Modelling and experimental validation of external spur gear machines for fluid power applications. Simulation Modelling Practice and Theory, 19(9), 2007-2031.

- [9] Eaton, M., Keogh, P. S., & Edge, K. A. (2006). The modelling, prediction, and experimental evaluation of gear pump meshing pressures with particular reference to aero-engine fuel pumps. *Proceedings of the Institution of Mechanical Engineers, Part I: Journal of Systems and Control Engineering*, 220(5), 365-379.
- [10] Mancò, S., Nervegna, N., & Rundo, M. (2002). A contribution to the design of hydraulic lube pumps. *International Journal of Fluid Power*, 3(1), 21-32.
- [11] Wieczorek, U., & Ivantysynova, M. (2002). Computer aided optimization of bearing and sealing gaps in hydrostatic machines—the simulation tool CASPAR. *International Journal of Fluid Power*, 3(1), 7-20.
- [12] Manring, N. D. (2000). The discharge flow ripple of an axial-piston swash-plate type hydrostatic pump. *Journal of dynamic systems, measurement, and control*, 122(2), 263-268.
- [13] Leonhard, L., Murrenhoff, H., Lang, J., & Knoll, G. (2011). Aus Wissenschaft und Forschung-Tribological Analysis of the Piston/Cylinder Interface of Hydrostatic Piston Machines—Elastohydrodynamic Simulation Technique and Experimental Validation. *Tribologie und Schmierungstechnik*, 58(5), 5.
- [14] Pelosi, M., & Ivantysynova, M. (2012). A geometric multigrid solver for the piston–cylinder interface of axial piston machines. *Tribology Transactions*, 55(2), 163-174.
- [15] Bergada, J. M., Watton, J., Haynes, J. M., & Davies, D. L. (2010). The hydrostatic/hydrodynamic behaviour of an axial piston pump slipper with multiple lands. *Meccanica*, 45(4), 585-602.
- [16] Schenk, A., & Ivantysynova, M. (2011, October). An Investigation of the Impact of Elastohydrodynamic Deformation on Power Loss in the Slipper Swashplate Interface. In *Symposium on Fluid Power (Vol. 2011)*.
- [17] Ivantysynova, M., & Baker, J. (2009). Power loss in the lubricating gap between cylinder block and valve plate of swash plate type axial piston machines. *International Journal of Fluid Power*, 10(2), 29-43.
- [18] Zecchi, M. (2013). A novel fluid structure interaction and thermal model to predict the cylinder block/valve plate interface performance in swash plate type axial piston machines (Doctoral dissertation, Purdue University).
- [19] Dhar, S., Vacca, A. (2012). A novel CFD–Axial motion coupled model for the axial balance of lateral bushings in external gear machines. *Simulation Modelling Practice and Theory*, 26, 60-76.

- [20] Dhar, S., Vacca, A. (2013). A fluid structure interaction—EHD model of the lubricating gaps in external gear machines: Formulation and validation. *Tribology International*, 62, 78-90.
- [21] Schenk, A., Zecchi, M., & Ivantysynova, M. (2013, October). Accurate Prediction of Axial Piston Machine's Performance Through a Thermo-Elasto-Hydrodynamic Simulation Model. In *ASME/BATH 2013 Symposium on Fluid Power and Motion Control* (pp. V001T01A034-V001T01A034). American Society of Mechanical Engineers.
- [22] Dhar, S., Vacca, A., & Lettini, A. (2013, October). A Novel Fluid–Structure–Thermal Interaction Model for the Analysis of the Lateral Lubricating Gap Flow in External Gear Machines. In *ASME/BATH 2013 Symposium on Fluid Power and Motion Control* (pp. V001T01A049-V001T01A049). American Society of Mechanical Engineers.
- [23] Thiagarajan, D., Dhar, S., & Vacca, A. (2014). A Novel Fluid Structure Interaction-EHD Model and Optimization Procedure for an Asymmetrical Axially Balanced External Gear Machine. *Tribology Transactions*, (in press).
- [24] Petrusevich, A. I. (1951). Fundamental conclusions from the contact-hydrodynamic theory of lubrication. *Izv. Akad. Nauk SSR (OTN)*, 2, 209-233.
- [25] Dowson, D., & Higginson, G. R. (1959). A numerical solution to the elasto-hydrodynamic problem. *Journal of Mechanical Engineering Science*, 1(1), 6-15.
- [26] Dowson, D., & Higginson, G. R. (1961). New roller bearing lubrication formula. *Engineering (London)*, 192(4972), 158-159.
- [27] Dowson, D., Higginson, G. R., & Dowson, D. (1977). *Elasto-hydrodynamic lubrication (Vol. 2)*. Oxford: Pergamon Press.
- [28] Crook, A. W. (1963). The lubrication of rollers IV. Measurements of friction and effective viscosity. *Philosophical Transactions of the Royal Society of London. Series A, Mathematical and Physical Sciences*, 255(1056), 281-312.
- [29] Dyson, A. H. A. R., Naylor, H., & Wilson, A. R. (1965, June). Paper 10: The Measurement of Oil-Film Thickness in Elastohydrodynamic Contacts. In *Proceedings of the Institution of Mechanical Engineers, Conference Proceedings (Vol. 180, No. 2, pp. 119-134)*. SAGE Publications.
- [30] Houpert, L. G., & Hamrock, B. J. (1986). Fast approach for calculating film thicknesses and pressures in elastohydrodynamically lubricated contacts at high loads. *Journal of Tribology*, 108(3), 411-419.

- [31] Venner, C. H., & Lubrecht, A. A. (1994). Numerical simulation of a transverse ridge in a circular EHL contact under rolling/sliding. *Journal of tribology*, 116(4), 751-761.
- [32] Hughes, T. G., Elcoate, C. D., & Evans, H. P. (2000). Coupled solution of the elastohydrodynamic line contact problem using a differential deflection method. *Proceedings of the Institution of Mechanical Engineers, Part C: Journal of Mechanical Engineering Science*, 214(4), 585-598.
- [33] Hu, Y. Z., & Zhu, D. (2000). A full numerical solution to the mixed lubrication in point contacts. *Journal of Tribology*, 122(1), 1-9.
- [34] Liu, S., Wang, Q., & Liu, G. (2000). A versatile method of discrete convolution and FFT (DC-FFT) for contact analyses. *Wear*, 243(1), 101-111.
- [35] Conry, T. F., Wang, S., & Cusano, C. (1987). A Reynolds-Eyring equation for elastohydrodynamic lubrication in line contacts. *Journal of tribology*, 109(4), 648-654.
- [36] Peiran, Y., & Shizhu, W. (1990). A generalized Reynolds equation for non-Newtonian thermal elastohydrodynamic lubrication. *Journal of Tribology*, 112(4), 631-636.
- [37] Salehizadeh, H., & Saka, N. (1991). Thermal non-Newtonian elastohydrodynamic lubrication of rolling line contacts. *Journal of tribology*, 113(3), 481-491.
- [38] Zhu, D., & Wang, Q. J. (2011). Elastohydrodynamic lubrication: a gateway to interfacial mechanics—review and prospect. *Journal of Tribology*, 133(4), 041001.
- [39] Wu, S., & Cheng, H. S. (1991). A friction model of partial-EHL contacts and its application to power loss in spur gears. *Tribology Transactions*, 34(3), 398-407.
- [40] Jacod, B., Venner, C. H., & Lugt, P. M. (2001). A generalized traction curve for EHL contacts. *Journal of tribology*, 123(2), 248-253.
- [41] Jacod, B. C. H. P. M., Venner, C. H., & Lugt, P. M. (2003). Extension of the friction mastercurve to limiting shear stress models. *Journal of tribology*, 125(4), 739-746.
- [42] Jacod, B., Venner, C. H., & Lugt, P. M. (2004). Influence of longitudinal roughness on friction in EHL contacts. *Journal of tribology*, 126(3), 473-481.
- [43] Morales-Espejel, G. E., & Wemekamp, A. W. (2004). An engineering approach on sliding friction in full-film, heavily loaded lubricated contacts. *Proceedings of the Institution of Mechanical Engineers, Part J: Journal of Engineering Tribology*, 218(6), 513-527.

- [44] Xu, H., Houser, D. R., & Kahraman, A. (2005). A Model to Predict Friction Losses by Hypoid Gears. AGMA.
- [45] Merritt, H. E. (1967). Hydraulic control systems. John Wiley & Sons.
- [46] AMESim 4.2 User manual. Available at: <http://nupet.daelt.ct.utfpr.edu.br/> . Accessed Nov 20, 2014.
- [47] Reynolds, O. (1886). On the Theory of Lubrication and Its Application to Mr. Beauchamp Tower's Experiments, Including an Experimental Determination of the Viscosity of Olive Oil. Proceedings of the Royal Society of London, 40(242-245), 191-203.
- [48] Hamrock, B. J., Schmid, S. R., & Jacobson, B. O. (2004). Fundamentals of fluid film lubrication (Vol. 169). CRC press.
- [49] Pelosi, M., & Ivantysynova, M. (2010). A fully coupled thermo-elastic model for the rotating kit of axial piston machines. In ASME/Bath Symposium on Fluid Power and Motion Control, Bath, UK, Sept (pp. 15-17).
- [50] Ivantysyn, J., & Ivantysynova, M. (2001). Hydrostatic pumps and motors. New Delhi: Academic Books International.
- [51] OpenFOAM: The Open Source CFD toolbox. Available at: www.openfoam.com.
- [52] Jasak, H., & Weller, H. G. (2000). Application of the finite volume method and unstructured meshes to linear elasticity. International journal for numerical methods in engineering, 48(2), 267-287.
- [53] Pelosi, M., & Ivantysynova, M. (2011, January). Surface Deformations Enable High Pressure Operation of Axial Piston Pumps. In ASME 2011 Dynamic Systems and Control Conference and Bath/ASME Symposium on Fluid Power and Motion Control (pp. 193-200). American Society of Mechanical Engineers.
- [54] Oh, K. P., & Goenka, P. K. (1985). The elastohydrodynamic solution of journal bearings under dynamic loading. Journal of Tribology, 107(3), 389-394.
- [55] Wang, Q. J., Shi, F., & Lee, S. C. (1997). A mixed-lubrication study of journal bearing conformal contacts. Journal of tribology, 119(3), 456-461.
- [56] Xiong, S., Lin, C., Wang, Y., Liu, W. K., & Wang, Q. J. (2010). An efficient elastic displacement analysis procedure for simulating transient conformal-contact elastohydrodynamic lubrication systems. Journal of Tribology, 132(2), 021502.

- [57] Pelosi, M., & Ivantysynova, M. (2013). The Impact of Axial Piston Machines Mechanical Parts Constraint Conditions on the Thermo-Elastohydrodynamic Lubrication Analysis of The Fluid Film Interfaces. *International Journal of Fluid Power*, 14(3), 35-51.
- [58] Stefani, F. A., & Reborá, A. U. (2002). Finite element analysis of dynamically loaded journal bearings: influence of the bolt preload. *Journal of tribology*, 124(3), 486-493.
- [59] Piffeteau, S., Souchet, D., & Bonneau, D. (2000). Influence of thermal and elastic deformations on connecting-rod big end bearing lubrication under dynamic loading. *Journal of tribology*, 122(1), 181-191.
- [60] Shi, F. (2011). An analysis of floating piston pin (No. 2011-01-1407). SAE Technical Paper.
- [61] Olems, L. (2000). Investigations of the temperature behaviour of the piston cylinder assembly in axial piston pumps. *International Journal of Fluid Power*, 1(1), 27-39.
- [62] Dowson, D. (1977). Isothermal Elastohydrodynamic Lubrication of Point Contacts. *Journal of Lubrication Technology*, April, 265.
- [63] Evans, H. P., & Snidle, R. W. (1981). The isothermal elastohydrodynamic lubrication of spheres. *Journal of Tribology*, 103(4), 547-557.
- [64] Venner, C. H., & Ten Napel, W. E. (1992). Multilevel solution of the elastohydrodynamically lubricated circular contact problem part 2: smooth surface results. *Wear*, 152(2), 369-381.
- [65] Nijenbanning, G. C. H. H., Venner, C. H., & Moes, H. (1994). Film thickness in elastohydrodynamically lubricated elliptic contacts. *Wear*, 176(2), 217-229.
- [66] Zou, Q., Huang, C., & Wen, S. (1999). Elastohydrodynamic film thickness in elliptical contacts with spinning and rolling. *Journal of tribology*, 121(4), 686-692.
- [67] Habchi, W., Vergne, P., Eyheramendy, D., & Morales-Espejel, G. E. (2011). Numerical investigation of the use of machinery low-viscosity working fluids as lubricants in elastohydrodynamic lubricated point contacts. *Proceedings of the Institution of Mechanical Engineers, Part J: Journal of Engineering Tribology*, 225(6), 465-477.
- [68] Dowson, D., & Higginson, G. R. (1966). *Elasto-hydrodynamic lubrication: the fundamentals of roller and gear lubrication (Vol. 23)*. Oxford: Pergamon Press.
- [69] Barus, C. (1893). Isothermals, isopiestic and isometrics relative to viscosity. *American Journal of Science*, (266), 87-96.

- [70] Wang, J., Venner, C. H., & Lubrecht, A. A. (2013). Influence of Surface Waviness on the Thermal Elastohydrodynamic Lubrication of an Eccentric-Tappet Pair. *Journal of Tribology*, 135(2), 021001.
- [71] Jacobson, B. O., & Hamrock, B. J. (1984). Non-Newtonian fluid model incorporated into elastohydrodynamic lubrication of rectangular contacts. *Journal of tribology*, 106(2), 275-282.
- [72] Venner, C. H., ten Napel, W. T., & Bosma, R. (1990). Advanced multilevel solution of the EHL line contact problem. *Journal of Tribology*, 112(3), 426-431.
- [73] Venner, C. H., & Lubrecht, A. A. (Eds.). (2000). *Multi-level methods in lubrication* (Vol. 37). Elsevier.
- [74] Gupta, P. K. (1979). Dynamics of Rolling-Element Bearings—Part III: Ball Bearing Analysis. *Journal of Tribology*, 101(3), 312-318.
- [75] Gupta, P. K. (1984). *Advanced dynamics of rolling elements* (Vol. 39). New York: Springer-Verlag.

APPENDICES

Appendix A. Derivation of the Pressure Buildup Equation

This section presents the derivation of the pressure build-up equation which was to model the pressure generation within each control volume in the lumped parameter model for pump system. The reference figure is shown in Figure 85 which represents a control volume with net flow rate occurring through it.

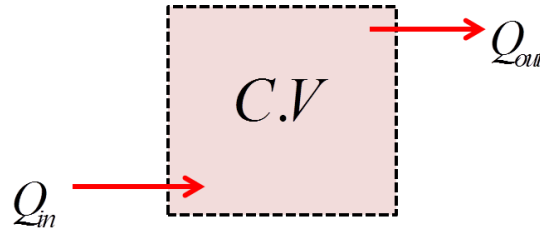


Figure 85: Arbitrary control volume in space.

The continuity equation for flow across a control volume is given by,

$$\frac{\partial}{\partial t} \int_{CV} \rho dV + \int_{CS} \rho \vec{u} \cdot d\vec{A} = 0 \quad (\text{A.1})$$

Now, using the lumped parameter model and neglecting the variation of ρ within the control volume, the above equation can be rearranged to get,

$$\frac{\partial(\rho V)}{\partial t} + \rho \int_{CS} \vec{u} \cdot d\vec{A} = 0 \quad (\text{A.2})$$

$$\rho \left[\frac{dV}{dt} + \int_{CS} \vec{u} \cdot d\vec{A} \right] = -V \frac{d\rho}{dt} \quad (\text{A.3})$$

By definition of bulk modulus, $K = \frac{dP}{d\rho/\rho}$. Differentiating with respect to time,

$$\frac{dP}{dt} = \frac{K}{\rho} \frac{d\rho}{dt} \quad (\text{A.4})$$

Substituting Equation (A.4) in (A.3),

$$-\left(\frac{dV}{dt} + \int_{CS} \vec{u} \cdot d\vec{A}\right) = \frac{V}{K} \frac{dP}{dt} \quad (\text{A.5})$$

It can be observed that $\int_{CS} \vec{u} \cdot d\vec{A}$ term represents the net flow rate occurring through the control volume with flow going outwards taken as positive. Hence, $\int_{CS} \vec{u} \cdot d\vec{A}$ can be replaced by $Q_{out} - Q_{in}$. Substituting this expression and rearranging, the final form of the pressure buildup equation can be obtained,

$$\frac{dP}{dt} = \frac{K}{V} \left[-\frac{dV}{dt} - (Q_{out} - Q_{in}) \right] \quad (\text{A.6})$$

Appendix B. Derivation of the Reynolds Equation

In the present section, a detailed derivation of the Reynolds' Equation which was used to model the lubricating gap flow in piston-cylinder interface will be presented. The derivation will be performed with reference to Figure 86. The clearance between the top and the bottom surfaces (shown in dotted lines) is representative of the lubricating gap. Since the FSI model for the piston-cylinder lubricating gap needs to account for features (deformation/tilt) for both the piston and the cylinder, the derivation will be performed using a reference plane (in blue) which is at an arbitrary orientation within the lubricating gap, and represents $z=0$. This leads to the following definition of the lubricating gap height,

$$h = h_t - h_b \quad (\text{B.1})$$

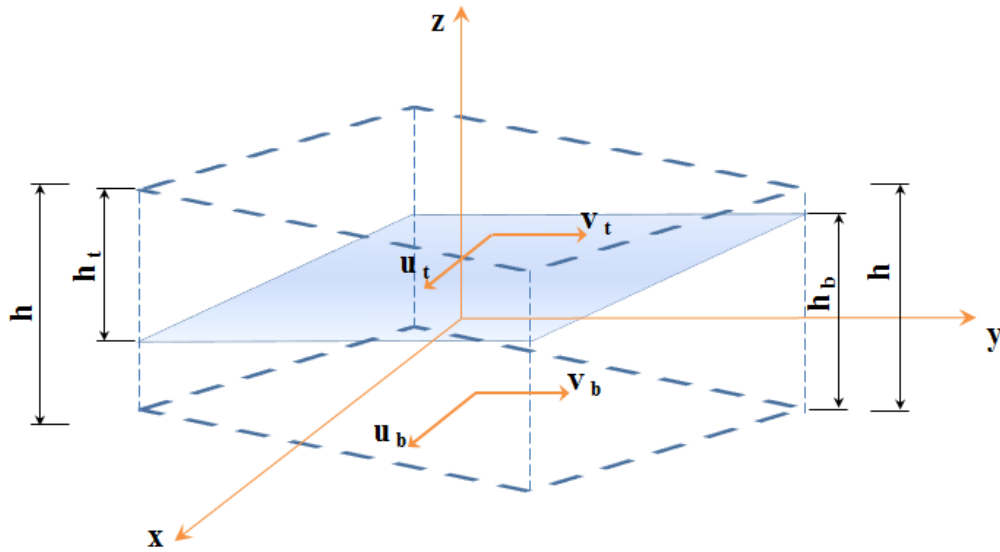


Figure 86: Definition of lubricating gap used in the derivation. The top and the bottom surfaces are represented using the dotted lines and the reference plane ($z=0$) is represented in blue.

The universal governing equation for fluid flows is the well-known Navier Stokes' equation represented in its most compact form in Equation (B.2).

This is in fact representative of 3 equations for the 3 Cartesian components of the velocity vector \mathbf{v} :

$$\rho \frac{\partial \mathbf{v}}{\partial t} + \nabla \cdot (\rho \mathbf{v} \mathbf{v}) = -\nabla p + \nabla \cdot \boldsymbol{\sigma} + \rho \mathbf{f} \quad (\text{B.2})$$

Effects of body forces acting on the lubricating film are negligible. In addition the lubricating fluids modeled in the present work are Newtonian fluids so,

$$\boldsymbol{\sigma} = \mu \nabla \mathbf{v}. \quad (\text{B.3})$$

Navier stokes equation then becomes,

$$\rho \frac{\partial \mathbf{v}}{\partial t} + \nabla \cdot (\rho \mathbf{v} \mathbf{v}) = -\nabla p + \nabla \cdot (\mu \nabla \mathbf{v}). \quad (\text{B.4})$$

In lubricating gap flows the following assumptions are made from lubrication theory [48],

- The fluid viscous forces dominate over the inertial forces, so the convective acceleration term $\nabla \cdot (\rho \mathbf{v} \mathbf{v})$ can be neglected.
- Steady state flow is assumed, so $\rho \frac{\partial \mathbf{v}}{\partial t} = 0$.
- The pressure in the lubricating film is assumed to be constant across the thickness of the film - thus $p = p(x; y)$ – only varies along the plane of the film.
- The component of the velocity in the direction normal to the gap plane can be neglected, and the velocity can be expressed as $\mathbf{v} = (u(x; y; z), v(x; y; z))$, where u and v are still functions of the three spatial directions.
- The gradient of velocity in the gap plane is negligible with respect to the component in the direction of the gap height so that $\frac{\partial u, v}{\partial z} \gg \frac{\partial u, v}{\partial x}; \frac{\partial u, v}{\partial z} \gg \frac{\partial u, v}{\partial y}$.

The assumptions are driven by the fact that lubricating gap flows occur in geometries where the dimensions in the x and y directions (as shown in Figure 86) far exceed the dimensions in the z direction (which is usually of the order of micro-meters).

Using the assumptions listed above, Equation (B.4) simplifies to two PDEs,

$$\frac{\partial p}{\partial x} = \frac{\partial}{\partial z} \left(\mu \frac{\partial u}{\partial z} \right), \quad (\text{B.5})$$

$$\frac{\partial p}{\partial y} = \frac{\partial}{\partial z} \left(\mu \frac{\partial v}{\partial z} \right). \quad (\text{B.6})$$

An integration of the following equation is performed across the lubricating film. Viscosity is assumed to be a constant across the lubricating film, but can still vary across the x and y coordinates,

$$u = \frac{z^2}{2\mu} \frac{\partial p}{\partial x} + C_1 \frac{z}{\mu} + C_2, \quad (\text{B.7})$$

$$v = \frac{z^2}{2\mu} \frac{\partial p}{\partial y} + C_3 \frac{z}{\mu} + C_4. \quad (\text{B.8})$$

Now, imposing the boundary conditions for velocities which are the velocities of the top and bottom surfaces as shown in Figure 86,

$$u = u_t \text{ and } v = v_t \text{ at } z = h_t,$$

$$u = u_b \text{ and } v = v_b \text{ at } z = h_b.$$

The solution to the Equations (B.7) and (B.8) can be found to be,

$$u = \frac{1}{2\mu} \frac{\partial p}{\partial x} (z^2 - z(h_t + h_b) + h_t h_b) - \frac{z(u_t - u_b)}{h_t - h_b} + \frac{h_t u_b - h_b u_t}{h_t - h_b}, \quad (\text{B.9})$$

$$v = \frac{1}{2\mu} \frac{\partial p}{\partial y} (z^2 - z(h_t + h_b) + h_t h_b) - \frac{z(v_t - v_b)}{h_t - h_b} + \frac{h_t v_b - h_b v_t}{h_t - h_b}. \quad (\text{B.10})$$

This is the most general solution for the velocities in the lubricating gap. For the piston-cylinder lubricating gap geometry as shown in Figure 31, assigning appropriate value of $\mathbf{v}_t = 0$ (static cylinder) and $\mathbf{v}_b = \mathbf{v}_g$ (reciprocating piston) leads to,

$$u = \frac{1}{2\mu} \frac{\partial p}{\partial x} (z^2 - z(h_t + h_b) + h_t h_b) - \frac{z u_g}{h_t - h_b} + \frac{h_t u_g}{h_t - h_b}, \quad (\text{B.11})$$

$$v = \frac{1}{2\mu} \frac{\partial p}{\partial y} (z^2 - z(h_t + h_b) + h_t h_b) - \frac{z v_g}{h_t - h_b} + \frac{h_t v_g}{h_t - h_b}. \quad (\text{B.12})$$

Now considering the continuity equation which along with the Navier Stokes' equation defines the behavior of fluid flow,

$$\frac{\partial \rho}{\partial t} + \nabla \cdot (\rho \mathbf{v}) = 0. \quad (\text{B.13})$$

Steady state assumption yields,

$$\nabla \cdot (\rho \mathbf{v}) = 0. \quad (\text{B.14})$$

Integrating the continuity equation over the lubricating gap heights,

$$\int_{h_b}^{h_t} \frac{\partial}{\partial x} \rho u \, dz + \int_{h_b}^{h_t} \frac{\partial}{\partial y} \rho v \, dz + \int_{h_b}^{h_t} \frac{\partial}{\partial z} \rho w \, dz = 0. \quad (\text{B.15})$$

First considering the integration of the first term, and splitting this into two terms, from the reference plate to the top surface and from the reference plane to the bottom surface,

$$\int_{h_b}^{h_t} \frac{\partial}{\partial x} \rho u \, dz = \int_{h_b}^0 \frac{\partial}{\partial x} \rho u \, dz + \int_0^{h_t} \frac{\partial}{\partial x} \rho u \, dz = - \int_0^{h_b} \frac{\partial}{\partial x} \rho u \, dz + \int_0^{h_t} \frac{\partial}{\partial x} \rho u \, dz. \quad (\text{B.16})$$

Since u and v are functions of all three coordinates Leibnitz's rule of integration can be used,

$$\int_0^h \frac{\partial}{\partial x} f(x, y, z) \, dz = -f(x, y, h) \frac{\partial h}{\partial x} + \frac{\partial}{\partial x} \int_0^h f(x, y, z) \, dz. \quad (\text{B.17})$$

Using this on Equation (B.14), it becomes,

$$- \left(-\rho u_b \frac{\partial h_b}{\partial x} + \frac{\partial}{\partial x} \rho \int_0^{h_b} u \, dz \right) + \left(-\rho u_t \frac{\partial h_t}{\partial x} + \frac{\partial}{\partial x} \rho \int_0^{h_t} u \, dz \right) = 0. \quad (\text{B.18})$$

At this point it can be noted that density, ρ is also assumed to be constant across the gap height (z), but can still vary in the x and y dimensions. Grouping terms, Equation (B.16) can be written as,

$$\rho u_b \frac{\partial h_b}{\partial x} - \rho u_t \frac{\partial h_t}{\partial x} + \frac{\partial}{\partial x} \rho \int_{h_b}^{h_t} u \, dz = 0. \quad (\text{B.19})$$

For $\int_{h_b}^{h_t} \frac{\partial}{\partial x} \rho v \, dz$ a similar approach is applicable leading to,

$$\rho v_b \frac{\partial h_b}{\partial y} - \rho v_t \frac{\partial h_t}{\partial y} + \frac{\partial}{\partial y} \rho \int_{h_b}^{h_t} v \, dz = 0. \quad (\text{B.20})$$

For the third term, the integration can be performed more directly. The top and the bottom surface can also exhibit normal squeeze micro-motion, which means that they can have velocities also in the z direction. So,

$$\int_{h_b}^{h_t} \frac{\partial}{\partial z} \rho w \, dz = \rho (w_t - w_b). \quad (\text{B.21})$$

Squeeze velocities are essentially the rate at which the gap height h is changing, so writing $w_t = \frac{\partial h_t}{\partial t}$ and $w_b = \frac{\partial h_b}{\partial t}$, we get,

$$\rho(w_t - w_b) = \rho\left(\frac{\partial h_t}{\partial t} - \frac{\partial h_b}{\partial t}\right). \quad (\text{B.22})$$

So Equation (B.14) finally can be written as,

$$\begin{aligned} \rho u_b \frac{\partial h_b}{\partial x} + \rho v_b \frac{\partial h_b}{\partial y} - \rho u_t \frac{\partial h_b}{\partial x} - \rho v_t \frac{\partial h_b}{\partial y} + \rho \left(\frac{\partial h_t}{\partial t} - \frac{\partial h_b}{\partial t}\right) + \frac{\partial}{\partial x} \rho \int_{h_b}^{h_t} u \, dz + \\ \frac{\partial}{\partial y} \rho \int_{h_b}^{h_t} v \, dz = 0. \end{aligned} \quad (\text{B.23})$$

To complete the derivation of the Reynolds equation, the expressions for the velocity field derived in Equations (B.9) and (B.10) are to be substituted in the integral terms.

Performing the integrations and some grouping of terms we get,

$$\begin{aligned} \frac{\partial}{\partial x} \rho \int_{h_b}^{h_t} u \, dz + \frac{\partial}{\partial y} \rho \int_{h_b}^{h_t} v \, dz = -\frac{\partial}{\partial x} \left(\frac{\rho(h_t - h_b)^3}{12\mu} \frac{dp}{dx} \right) - \frac{\partial}{\partial y} \left(\frac{\rho(h_t - h_b)^3}{12\mu} \frac{dp}{dy} \right) + \\ \rho(h_t - h_b) \frac{\partial}{\partial x} \left(\frac{u_t + u_b}{2} \right) + \rho(h_t - h_b) \frac{\partial}{\partial y} \left(\frac{v_t + v_b}{2} \right) + \rho \left(\frac{u_t + u_b}{2} \right) \frac{\partial(h_t - h_b)}{\partial x} + \rho \left(\frac{v_t + v_b}{2} \right) \frac{\partial(h_t - h_b)}{\partial y}. \end{aligned} \quad (\text{B.24})$$

Using $h = h_t - h_b$ and substituting Equation (B.22) into (B.21), we finally have the most general form of the Reynolds equation which can account for features on both top and bottom surfaces:

$$\begin{aligned} -\frac{\partial}{\partial x} \left(\frac{\rho h^3}{12\mu} \frac{dp}{dx} \right) - \frac{\partial}{\partial y} \left(\frac{\rho h^3}{12\mu} \frac{dp}{dy} \right) + \rho h \frac{\partial}{\partial x} \left(\frac{u_t + u_b}{2} \right) + \rho h \frac{\partial}{\partial y} \left(\frac{v_t + v_b}{2} \right) + \rho \left(\frac{u_t + u_b}{2} \right) \frac{\partial h}{\partial x} + \\ \rho \left(\frac{v_t + v_b}{2} \right) \frac{\partial h}{\partial y} + \rho u_b \frac{\partial h_b}{\partial x} + \rho v_b \frac{\partial h_b}{\partial y} - \rho u_t \frac{\partial h_b}{\partial x} - \rho v_t \frac{\partial h_b}{\partial y} + \rho \left(\frac{\partial h_t}{\partial t} - \frac{\partial h_b}{\partial t} \right) = 0. \end{aligned} \quad (\text{B.25})$$

This form of the Reynolds equation was then further simplified considering the geometry of the lubricating gap in piston-cylinder interface. Firstly, the top surface (cylinder) is stationary so $v_t, u_t = 0$. In addition, the spatial derivative terms of the surface velocities are also not encountered in a quasi-steady analysis of piston, which is the case of interest in the present work. With this, we get

$$\begin{aligned} -\frac{\partial}{\partial x} \left(\frac{\rho h^3}{12\mu} \frac{dp}{dx} \right) - \frac{\partial}{\partial y} \left(\frac{\rho h^3}{12\mu} \frac{dp}{dy} \right) + \rho \left(\frac{u_b}{2} \right) \frac{\partial h}{\partial x} + \rho \left(\frac{v_b}{2} \right) \frac{\partial h}{\partial y} + \rho u_b \frac{\partial h_b}{\partial x} + \rho v_b \frac{\partial h_b}{\partial y} + \rho \left(\frac{\partial h_t}{\partial t} - \right. \\ \left. \frac{\partial h_b}{\partial t} \right) = 0. \end{aligned} \quad (\text{B.26})$$

Writing this using differential operator notation, we have the form of Reynolds equation seen in Equation (4.3), which is used in the present work:

$$\nabla \cdot \left(\frac{-\rho h^3}{12\mu} \nabla p \right) + \frac{\rho \mathbf{v}_b}{2} \cdot \nabla h + \rho \mathbf{v}_b \cdot \nabla (h_b) + \rho \left(\frac{\partial h_t}{\partial t} - \frac{\partial h_b}{\partial t} \right) = 0. \quad (\text{B.27})$$